ELASTIC REVERSE-TIME MIGRATION IMAGING USING PERFORATION SHOTS AND VERTICAL RECEIVER ARRAYS

A Thesis Presented to

the Faculty of the Department of the Earth and Atmospheric Sciences

University of Houston

In Partial Fulfillment of the

Requirements for the

Degree of Master of Science

By

Nicholas Andrew Brooks

December 2016

ELASTIC REVERSE-TIME MIGRATION IMAGING USING PERFORATION SHOTS AND VERTICAL RECEIVER ARRAYS

_____

Nicholas Brooks

Approved:

_____

Dr. Robert R. Stewart, Chairman

_____

Dr. Yingcai Zheng

_____

Dr. Steven Peterson

_____

Dean, College of Natural Sciences and Mathematics

Acknowledgements

I am sincerely thankful to several individuals without whom I would not be able to complete this thesis.

Firstly, I would like to express my thanks and gratitude to Dr. Robert Stewart for his guidance, direction, education, collaboration, and his great capacity to be patient. Throughout my undergraduate and graduate programs at The University of Houston, Dr. Stewart has been one of my greatest educational influences and leaders.

I am also very thankful to my thesis committee: Dr. Yincai Zheng and Dr. Steve Peterson for their encouragement, helpful discussion, constructive criticism, intellectual stimulation, and support.

I am also very thankful to my colleagues that I have met and have embraced me throughout the years. The foundation of my professional education occurred at Pinnacle Technologies and EOG Resources, where I experienced and learned an immeasurable amount about earthquake seismology, seismic data processing, and interpretation, the importance of collaboration and social etiquette, and the value of professional and business experience. I am thankful to the various coworkers and peers I have had at Bluware Inc., Shell Oil Co., and Hess Oil Co. Specifically, I am thankful to the upper management at Bluware Inc., for allowing me to exercise my creativity and for embracing my expertise and trusting my professional judgment in business endeavors, to my esteemed colleagues Bode Omoboya and Kenneth Hester for acting as my geophysical and computational science mentors, respectively.

Lastly and most importantly, I am supremely thankful to my family, especially my wife and parents, from whom I receive unconditional support, and love, and push me

to be the best I can be. I am entirely indebted to the three of them for the wonderful life and all that they've provided for me.

My parents are entirely responsible for molding me into the man I am today, and I thank them from the bottom of my heart for putting everything they have into me. My aim is to make them proud, and I strive every day to achieve that.

For almost a decade, my wife has been more than I ever could have expected from a companion. She experiences my life, as I do hers, in almost every facet to some capacity which is why there is no person with the capacity to empathize with me and lift me like she has. I am so thankful to her for challenging me every day to be better, do better, and live better.

Nick Brooks

December 1, 2016, Houston, Texas

ELASTIC REVERSE-TIME MIGRATION IMAGING USING PERFORATION SHOTS AND VERTICAL RECEIVER ARRAYS

An Abstract of a Thesis

Presented to

the Faculty of the Department of the Earth and

Atmospheric Sciences

University of Houston

In Partial Fulfillment of the

Requirements for the

Degree of Master of Science

By

Nicholas Andrew Brooks

December 2016

Abstract

Recent innovations in hydraulic-fracture stimulation have increased the prevalence of borehole seismic monitoring of microseisms. This research investigates elastic-wave propagation as it pertains to seismic sources within the local borehole vicinity and the utility of elastic-wave finite-difference solutions as a means to model elastic-wave propagation and as a kernel component in a reverse-time migration imaging condition.

A 2-D fourth order spatially accurate finite-difference solution to the elastic-wave equation is implemented to model wave propagation in elastic media resulting from a variety of focal-mechanism types and orientations. This algorithm's simulated wavefield is compared to that of a preexisting finite-difference solution implementation in seismic Unix's suea2df and an approximate analytic solution to the elastic-wave equation.

A modified elastic reverse-time migration imaging condition is presented and tested on synthetic data propagated through a single-diffractor, two horizontal interfaces, and a subset of the Marmousi 2 model. Each test case simulates common acquisition geometries encountered in a perforation shot monitoring in an unconventional well and is demonstrated to be a potentially feasible imaging technique for near borehole subsurface structure. Imaging quality is then demonstrated to be dependent on acquisition geometry as described by the Nyquist sampling theorem. The reverse-time migration algorithm is then invoked on a dataset acquired from a vertically oriented receiver array by Hess Oil Co. from perforation shots in the En-Person 3H well.

Table of Contents

List of Figures

Dedication

This work is dedicated to my wife Kelly and my parents Nigel and Christina, who know me best, encourage and care for me most, and support and love me through everything.

Chapter 1. Review of introduction, objectives, and outline

1.1 HYDRAULIC FRACTURING AND MICROSEISMIC CONCEPTS

In recent years, innovative advances in hydraulic-fracture stimulation of tight rock formations have made unconventional reservoir production increasingly common (Ratner and Tiemann, 2015). Seismic recording of energy released during fracture stimulation has become a common and effective way of acquiring information about the state of the formation as the high-pressure fracture stimulation alters it. Specifically, kinetic energy is recorded at a distance in vertical monitoring wells or in surface monitoring arrays from stimulated fractures due to hydraulic fracturing. The acquired wavefield is inferred to depend on media material properties and focal-mechanism characteristics. Current practices in microseismic data processing typically focus on identifying hypocenter locations of microearthquakes (Li et al. 2012, 2013).

Current practices in "perf and plug" style hydraulic-fracture stimulation focus on the isolation of production zones within the lateral well via a cased borehole plug. After zone isolation is performed, well casing perforations are created with a perforation shot that consists of a focused explosion of material into the wall of the wellbore (Blanton and Mackenzie, 2006). The resulting seed fractures act as nucleation points from which new fractures can propagate when hydraulic pumping is initiated. The kinetic energy imparted into the medium surrounding the borehole during perforation provides an effective mechanism for seismologists to infer information about the seismic properties of the medium. Velocity model inferences may be made by considering direct-wave

travel times from the known perforation location to the known receiver positions. Current practice in microseismic monitoring focuses on identifying and locating positions of fractures as inferred hypocenter locations using optimization algorithms. One such algorithm is a type of "grid search" algorithm that identifies an optimal grid node as the hypocenter such that the result from predefined wavefield comparison criteria is minimized when evaluated on the real data and data simulated from the optimal grid node (Warpinski et al., 2005). Propagation of the adjoint state wavefield and identification of its local maxima amplitude as an indicator of source position identification in space and time has been a recent innovation regarding microseismic hypocenter location (Nakata and Beroza, 2016). Due to the simulated wavefield's strong dependence on medium parameters through which it travels, one such challenge associated with accurate hypocenter location is proper characterization and parameterization of the source and medium through which seismic energy propagates. Errors in velocity model construction and source parameterization are common causes of error in microseismic hypocenter location. Lateral and vertical non-homogeneities combined with the possibility of anisotropy in the physical medium expose current deficiencies in industry standard simulation algorithms that make simplistic assumptions about the medium's spatially variant properties as well as its directionally variant properties. As our understanding of the subsurface grows and the application of our seismic methods expand, requirements for more rigorous and comprehensive modeling become more important to satisfy.

The seismic energy imparted into the medium from processes involved in hydraulic fracturing are commonly used in the estimation of hypocenter locations, but, to the best of our knowledge, are not commonly used in reservoir and formation reflectivity

imaging. Typical imaging kernels use mechanisms as an approximate solution to the wave equation that best models real world data. Reverse-time migration techniques utilize finite-difference or finite element approximate solutions. I assert and demonstrate in this thesis that there is potential for perforation shot seismicity to be utilized in local reservoir imaging via reverse-time migration.

1.2 OBJECTIVES AND CONTRIBUTIONS

I aim to accomplish several tasks:

1. **Define and implement simulation algorithms:** I have developed and implemented a staggered-grid finite-difference approximate solution to the elastic-wave equation that incorporates any symmetry of stiffness tensor parameterization of elastic media. Source parameterization within the algorithm accommodates any combination of compressional or shearing stresses along any rotational axis.
2. **Validate the simulation algorithm implementation:** I validate the simulation algorithm by comparing it to a seismic Unix's implementation suea2df and an analytic solution to the elastic-wave equation.
3. **Utilize simulation algorithms to characterize model and focal-mechanism dependent radiation patterns:** I aim to analyze and characterize radiation patterns as a function of the focal-mechanism structure and the medium's property model.
4. **Develop a theoretical foundation for an elastic reverse-time migration imaging condition:** I extend previous notions of imaging conditions beyond

surface acoustic-based methods to a borehole monitored elastic context. I test this on a set of synthetic data sets with various property models. Synthetic models created are intended to range from very simple single interface scenarios to a complex normal fault scenario. I also aim to characterize survey geometry dependent imaging artifacts by comparing image results from different survey geometries. I intend to be mindful of the lateral borehole and microseismic context in which I intend to implement our algorithm in by constructing synthetic cases with typical VSP receiver geometries and lateral offset sources.

5. **Test our elastic reverse-time migration imaging condition on real world data:** I demonstrate the feasibility of our elastic reverse-time migration algorithm by executing it on the Hess Bakken dataset.

1.3 OUTLINE OF THIS THESIS

This thesis is composed of 6 chapters:

- **Chapter 1** introduces hydraulic fracturing concepts as they pertain to perforation shot-induced seismicity, gaps in common industry standard technologies as they pertain to elastic-wave propagation simulation, specifically, propagation medium and source-mechanism parameterization. Objectives and an outline of this research are presented.
- **Chapter 2** Reviews an elastic-wave equation derivation and its solution via finite-differences on a staggered-grid in stress-velocity formulation. Validation with Seismic Unix's Suea2df finite-difference solution and an analytic solution to the

elastic-wave equation in an elastic half-space is presented via comparison of wavefield samples in time.

- **Chapter 3** Analyzes and characterizes radiation patterns from several focal-mechanism types and synthetic models, both isotropic and anisotropic.
- **Chapter 4** Defines a new elastic reverse-time migration algorithm and demonstrates its execution on a subset of the Marmousi 2 computational model and other computational models developed at the University of Houston.
- **Chapter 5** Attempts to implement the reverse-time migration algorithm defined and tested in Chapter 4 of this thesis on a Bakken Microseismic data set provided by Hess Oil Co.
- **Chapter 6** Summarizes major contributions of this thesis and provides recommendations for and interests in future work about the material presented in this thesis.

Chapter 2. Finite-Difference solution to the elastic-wave equation

2.1 INTRODUCTION

There are two motivating reasons for developing a custom wave-simulation algorithm. Firstly, implementation of a custom simulation algorithm lends itself to quick and efficient modification, customization, and reimplementation. In addition to obtaining a better understanding of wave propagation and implementation of a finite-difference simulation algorithm, an implementation is now available for future work. Secondly, previous implementations in Seismic Unix (Juhlin 1995), Madagascar (Weiss and Shragge, 2013), Manning (2008), and ANIVEC contain limitations in limited symmetry configurations of the stiffness tensor, inability to accommodate lateral inhomogeneity, moment-tensor limitations, source-function limitations, 2D spatial domain constraints, stability concerns with non-stress-velocity finite-difference implementations, and a lack of robust boundary conditions for the removal of boundary reflections.

To accommodate limitations, a custom implementation of the elastic anisotropic stress-velocity finite-difference simulation algorithm was created. Source-mechanism(s) may be represented by moment-tensor and any source amplitude as a function of time. Medium parameters are represented at each grid point as a stiffness tensor and density. Boundary conditions are implemented with a damping coefficient of the padding layer and a reimplementation of a one-way wave equation absorbing boundary condition (Cerjan et al., 1985).

2.2 WAVE EQUATION DERIVATION

Elastic-wave propagation is commonly derived from a combination of Newton's second law of motion as a kinematic relationship and Hooke's law as a stress-strain relationship. Note that the component index notation in this thesis adopts the Einstein summation convention.

$$\rho \frac{\partial v_i}{\partial t} = \frac{\partial \tau_{ij}}{\partial x_j}. \tag{2.1}$$

$$\tau_{ij}(\boldsymbol{x}, t) = C_{ijkl}(\boldsymbol{x}) \varepsilon_{kl}(\boldsymbol{x}, t). \tag{2.2}$$

Where $\rho(\boldsymbol{x})$ represents the density of the model, $v_i(\boldsymbol{x}, t)$ represents the particle velocity of the model, and $\boldsymbol{x}, t$ are spatial and temporal coordinates, respectively. The internal forces are described by $\tau_{ij}(\boldsymbol{x}, t), \varepsilon_{kl}(\boldsymbol{x}, t)$ represents strain, and $C_{ijkl}(\boldsymbol{x})$ represents the linear relationship between stress and strain in the form of a rank 4 tensor. Strain may be further expressed in terms of the spatial derivatives of its components.

$$\frac{\partial \varepsilon_{kl}(\boldsymbol{x}, t)}{\partial t} = \frac{1}{2}\left(\frac{\partial v_k(\boldsymbol{x}, t)}{\partial x_l} + \frac{\partial v_l(\boldsymbol{x}, t)}{\partial x_k}\right). \tag{2.3}$$

The stress-velocity representation of Hooke's law is described as

$$\frac{\partial \tau_{ij}}{\partial t} = C_{ijkl} \frac{1}{2}\left(\frac{\partial v_k}{\partial x_l} + \frac{\partial v_l}{\partial x_k}\right). \tag{2.4}$$

Thus, Equation 2.1 may be reformulated into a homogeneous elastic-wave equation.

$$\rho(\boldsymbol{x}) \frac{\partial v_i(\boldsymbol{x}, t)}{\partial t} = \frac{\partial}{\partial x_j}\left(C_{ijkl} \frac{1}{2}\left(\frac{\partial v_k}{\partial x_l} + \frac{\partial v_l}{\partial x_k}\right)\right). \tag{2.5}$$

Sources described by dislocation within the medium may be represented as a seismic moment-tensor,

$$\mu_{ij} = \begin{bmatrix} \mu_{11} & \mu_{12} & \mu_{13} \\ \mu_{21} & \mu_{22} & \mu_{23} \\ \mu_{31} & \mu_{32} & \mu_{33} \end{bmatrix}. \tag{2.6}$$

The moment-tensor can be incorporated into a non-homogeneous representation of the elastic-wave equation. Minkoff (2002) incorporates both vector force source $f_i(\boldsymbol{x}, t)$ and moment sources $\mu_{ij}(\boldsymbol{x}, t)$ by describing the wave equation as

$$\rho(\boldsymbol{x}) \frac{\partial v_i(\boldsymbol{x}, t)}{\partial t} = \frac{\partial \tau_{ij}(\boldsymbol{x}, t)}{\partial x_j} + f_i(\boldsymbol{x}, t) + \frac{\partial \mu_{ij}(\boldsymbol{x}, t)}{\partial x_j}. \tag{2.7}$$

2.2.1 Voigt Index Reduction

The symmetric nature of the stress and strain terms ($\varepsilon_{ij} = \varepsilon_{ji}\ and\ \tau_{ij} = \tau_{ji}$) implies a reduction in rank transformation on the stiffness tensor in order to simplify calculation and has been rigorously derived in (Thomsen 1986). The number of independent coefficients for an arbitrarily symmetric stiffness tensor is determined by the following symmetry relationships:

$$C_{ijkl} = C_{jikl} = C_{ijlk} = C_{klji}. \tag{2.8}$$

$$C_{ijkl} \rightarrow C_{\alpha\beta} \qquad for \qquad \alpha, \beta = 1,2,3,4,5,6. \tag{2.9}$$

While the number of coefficients for a stiffness tensor in 3D is $3^4 = 81$, the symmetric relationship expressed in Equation 2.8 and 2.9 yields 21 independent stiffness tensor components for a stiffness tensor of arbitrary symmetry. For brevity, an abbreviated form of Hooke's law can be inferred from the symmetric nature of the stress and strain tensors in 2.7. This Voigt index reduction (Cerveny, 2001) reduces the number of components of the stress and strain values from Equation 2.4.

$$\tau_{ij} = C_{ijkl}\varepsilon_{kl} \quad Becomes \quad \tau_{\alpha} = C_{\alpha\beta}\varepsilon_{\beta}. \tag{2.10}$$

$$\begin{bmatrix}\tau_{11}\\ \tau_{22}\\ \tau_{33}\\ \tau_{23}\\ \tau_{13}\\ \tau_{12}\end{bmatrix} = \begin{bmatrix} C_{1111} & C_{1122} & C_{1133} & C_{1123} & C_{1113} & C_{1112} \\ & C_{2222} & C_{2233} & C_{2223} & C_{2213} & C_{2212} \\ & & C_{3333} & C_{3323} & C_{3313} & C_{3312} \\ & & & C_{2323} & C_{2313} & C_{2312} \\ & symmetric & & & C_{1313} & C_{1312} \\ & & & & & C_{1212} \end{bmatrix} \begin{bmatrix}\varepsilon_{11}\\ \varepsilon_{22}\\ \varepsilon_{33}\\ 2\varepsilon_{23}\\ 2\varepsilon_{13}\\ 2\varepsilon_{12}\end{bmatrix}. \tag{2.11}$$

$$\begin{bmatrix}\tau_{1}\\ \tau_{2}\\ \tau_{3}\\ \tau_{4}\\ \tau_{5}\\ \tau_{6}\end{bmatrix} = \begin{bmatrix} C_{11} & C_{12} & C_{13} & C_{14} & C_{15} & C_{16} \\ & C_{22} & C_{23} & C_{24} & C_{25} & C_{26} \\ & & C_{33} & C_{34} & C_{35} & C_{36} \\ & & & C_{44} & C_{45} & C_{46} \\ & symmetric & & & C_{55} & C_{56} \\ & & & & & C_{66} \end{bmatrix} \begin{bmatrix}\varepsilon_{1}\\ \varepsilon_{2}\\ \varepsilon_{3}\\ \varepsilon_{4}\\ \varepsilon_{5}\\ \varepsilon_{6}\end{bmatrix}. \tag{2.12}$$

2.3 STAGGERED-GRID FINITE-DIFFERENCES

Staggered-grid techniques in finite-difference approximations attempt to correct resolution errors from overlapping and regular grids and are more stable than non-staggered-grid approaches (Madariaga 1976). The staggered-grid technique was first applied to finite-difference approximations of the electric and magnetic field components of Maxwell's equations (Yee, 1966) and has since been applied to other wave equation approximate solution techniques (Madariaga, 1976). Field parameters are positioned at half index increments in the computational-grid. By using a combination of forward and backward derivatives, derivative operations on the field rotate about grid indices (Figure 2.2).

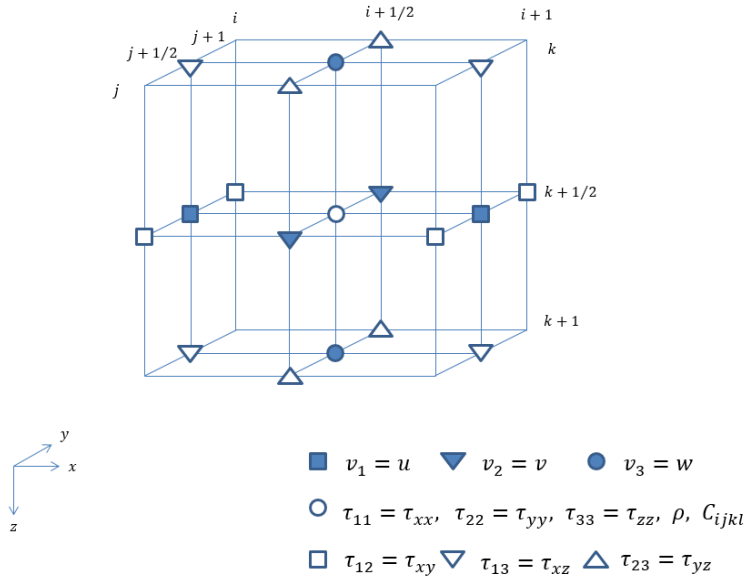

Figure 2.1: A staggered computational-grid with elastic property values at the corresponding grid node half increments. Spatial derivative operations are performed on property values at half-incremented grid nodes. The accuracy (order) of discrete differentiation relies on the number of terms incorporated from a Taylor series expansion (Grossmann et al. 2007).

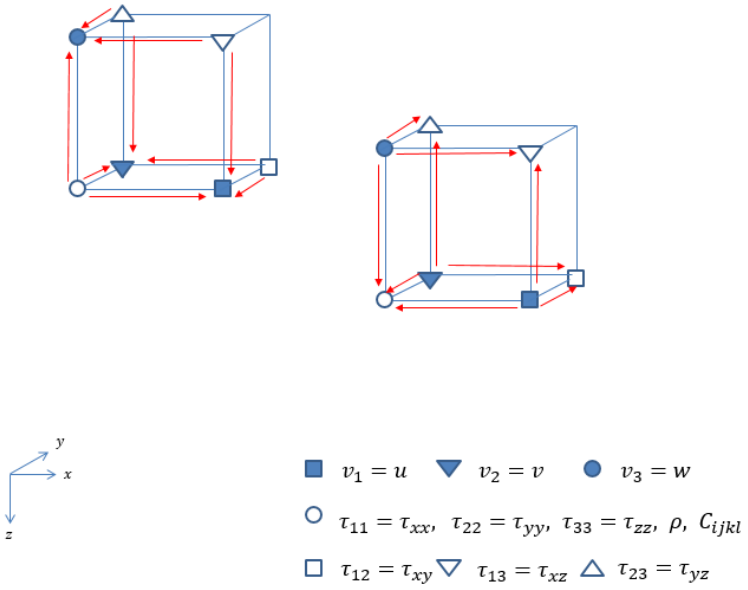

Figure 2.2: Geometry of staggered-grid central-difference operations. The **Left** most cube represents an operation on stress and property field values in half-index increments in order to propagate velocity-field values forward in time. The **Right** most cube represents an operation on velocity-field values in half-index increments to propagate stress-field values forward in time.

2.3.1 Explicit Formulation

The system of equations used in the formation of explicit finite-differences can be formed by iterating over each basis vector defining the Cartesian coordinate system used for Equation 2.1 and Equation 2.2. Such a system of equations is expressed as:

$$\rho \frac{\partial v_i}{\partial t} = \frac{\partial \tau_{ij}}{\partial x_j} \quad And \quad \frac{\partial \tau_{ij}}{\partial t} = C_{ijkl} \frac{1}{2}\left(\frac{\partial v_k}{\partial x_l} + \frac{\partial v_l}{\partial x_k}\right) \quad i,j,k,l = 1,2,3. \tag{2.13}$$

I utilize a combination of forward and backward difference operators in a circular manner as detailed by Levander (1988). Where the discrete difference operator operates forward and backward:

$$\frac{\partial f_m}{\partial \alpha} \approx D_\alpha^+ f_{m|i,j,k} = \frac{\left[\frac{9}{8}\left(f_{m|i+\frac{1}{2},j,k} - f_{m|i-\frac{1}{2},j,k}\right) - \frac{1}{24}\left(f_{m|i+\frac{3}{2},j,k} - f_{m|i-\frac{3}{2},j,k}\right)\right]}{\Delta\alpha} \quad Forward. \tag{2.14}$$

$$\frac{\partial f_m}{\partial \alpha} \approx D_\alpha^- f_{m|i,j,k} = \frac{\left[\frac{9}{8}\left(f_{m|i-\frac{1}{2},j,k} - f_{m|i+\frac{1}{2},j,k}\right) - \frac{1}{24}\left(f_{m|i-\frac{3}{2},j,k} - f_{m|i+\frac{3}{2},j,k}\right)\right]}{\Delta\alpha} \quad Backward. \tag{2.15}$$

Where f_m is a vector function with m components, α is the spatial component on which a spatial derivative will be evaluated, and i is the grid index at which the discrete derivative will be evaluated in the direction of α.

This differentiation technique operates on a staggered computational-grid with spatial node differences of $\Delta x, \Delta y, and\ \Delta z$ and a temporal difference of Δt. To form the discrete representation of the elastodynamic equations, I set $v_1 = u,\ v_2 = v,\ v_3 = w$ for conciseness, $x, y, and\ z$ are vector and tensor component basis vectors in 3 dimensions, and I redefine $i, j, and\ k$ as components of an ordered triple describing 3 dimensions of grid indices in order to reference a particular node of operation within the computational-grid at a time increment t. The discrete system of elastodynamic equations are fourth order accurate in space and second order accurate in time.

$$u_{i,j,k}^{t+\frac{1}{2}} = u_{i,j,k}^{t-\frac{1}{2}} + \frac{2\Delta t}{\rho_{i,j,k} + \rho_{i+1,j,k}}\left[D_x^+ \tau_{xx}^t + D_y^- \tau_{yx}^t + D_z^- \tau_{zx}^t\right]\Big|_{i,j,k}^{n}. \tag{2.16}$$

$$v_{i+\frac{1}{2},j+\frac{1}{2},k}^{t+\frac{1}{2}} = v_{i+\frac{1}{2},j+\frac{1}{2},k}^{t-\frac{1}{2}} + \frac{2\Delta t}{\rho_{i,j,k} + \rho_{i,j+1,k}}\left[D_x^- \tau_{yx}^t + D_y^+ \tau_{yy}^t + D_z^- \tau_{yz}^t\right]\Big|_{i+\frac{1}{2},j+\frac{1}{2},k}^{n}. \tag{2.17}$$

$$w_{i+\frac{1}{2},j,k+\frac{1}{2}}^{t+\frac{1}{2}} = w_{i+\frac{1}{2},j,k+\frac{1}{2}}^{t-\frac{1}{2}} + \frac{2\Delta t}{\rho_{i,j,k} + \rho_{i,j,k+1}}\left[D_x^- \tau_{yx}^t + D_y^- \tau_{yy}^t + D_z^+ \tau_{yz}^t\right]\Big|_{i+\frac{1}{2},j,k+\frac{1}{2}}^{n}. \tag{2.18}$$

$$\tau^{t+1}_{xx|i+\frac{1}{2},j,k} = \tau^{t}_{xx|i+\frac{1}{2},j,k}$$
$$+ \Delta t \left[C_{11} D_x^- u^{t-\frac{1}{2}} + C_{12} D_y^- v^{t-\frac{1}{2}} + C_{13} D_z^- w^{t-\frac{1}{2}} \right.$$
$$+ C_{14} \frac{1}{2}\left(D_z^+ v^{t-\frac{1}{2}} + D_y^+ w^{t-\frac{1}{2}} \right) + C_{15} \frac{1}{2}\left(D_z^+ u^{t-\frac{1}{2}} + D_x^+ w^{t-\frac{1}{2}} \right) \quad (2.19)$$
$$\left. + C_{16} \frac{1}{2}\left(D_y^+ u^{t-\frac{1}{2}} + D_x^+ v^{t-\frac{1}{2}} \right) \right] \Big|^{n+\frac{1}{2}}_{i+\frac{1}{2},j,k}.$$

$$\tau^{t+1}_{yy|i+\frac{1}{2},j,k} = \tau^{t}_{yy|i+\frac{1}{2},j,k}$$
$$+ \Delta t \left[C_{12} D_x^- u^{t-\frac{1}{2}} + C_{22} D_y^- v^{t-\frac{1}{2}} + C_{23} D_z^- w^{t-\frac{1}{2}} \right.$$
$$+ C_{24} \frac{1}{2}\left(D_z^+ v^{t-\frac{1}{2}} + D_y^+ w^{t-\frac{1}{2}} \right) + C_{25} \frac{1}{2}\left(D_z^+ u^{t-\frac{1}{2}} + D_x^+ w^{t-\frac{1}{2}} \right) \quad (2.20)$$
$$\left. + C_{26} \frac{1}{2}\left(D_y^+ u^{t-\frac{1}{2}} + D_x^+ v^{t-\frac{1}{2}} \right) \right] \Big|^{n+\frac{1}{2}}_{i+\frac{1}{2},j,k}.$$

$$\tau^{t+1}_{zz|i+\frac{1}{2},j,k} = \tau^{t}_{zz|i+\frac{1}{2},j,k}$$
$$+ \Delta t \left[C_{13} D_x^- u^{t-\frac{1}{2}} + C_{23} D_y^- v^{t-\frac{1}{2}} + C_{33} D_z^- w^{t-\frac{1}{2}} \right.$$
$$+ C_{34} \frac{1}{2}\left(D_z^+ v^{t-\frac{1}{2}} + D_y^+ w^{t-\frac{1}{2}} \right) + C_{35} \frac{1}{2}\left(D_z^+ u^{t-\frac{1}{2}} + D_x^+ w^{t-\frac{1}{2}} \right) \quad (2.21)$$
$$\left. + C_{36} \frac{1}{2}\left(D_y^+ u^{t-\frac{1}{2}} + D_x^+ v^{t-\frac{1}{2}} \right) \right] \Big|^{n+\frac{1}{2}}_{i+\frac{1}{2},j,k}.$$

$$\tau^{t+1}_{xy|i,j+\frac{1}{2},k} = \tau^{t}_{xx|i,j+\frac{1}{2},k}$$
$$+ \Delta t \left[C_{14} D_x^- u^{t-\frac{1}{2}} + C_{24} D_y^- v^{t-\frac{1}{2}} + C_{34} D_z^- w^{t-\frac{1}{2}} \right.$$
$$+ C_{44} \left(D_z^+ v^{t-\frac{1}{2}} + D_y^+ w^{t-\frac{1}{2}} \right) + C_{45} \left(D_z^+ u^{t-\frac{1}{2}} + D_x^+ w^{t-\frac{1}{2}} \right) \quad (2.22)$$
$$\left. + C_{46} \left(D_y^+ u^{t-\frac{1}{2}} + D_x^+ v^{t-\frac{1}{2}} \right) \right] \Big|^{n+\frac{1}{2}}_{i,j+\frac{1}{2},k}.$$

$$\tau^{t+1}_{xz|i,j,k+\frac{1}{2}} = \tau^{t}_{xz|i,j,k+\frac{1}{2}}$$
$$+ \Delta t \left[C_{15} D_x^- u^{t-\frac{1}{2}} + C_{25} D_y^- v^{t-\frac{1}{2}} + C_{35} D_z^- w^{t-\frac{1}{2}} \right.$$
$$+ C_{45} \left(D_z^+ v^{t-\frac{1}{2}} + D_y^+ w^{t-\frac{1}{2}} \right) + C_{55} \left(D_z^+ u^{t-\frac{1}{2}} + D_x^+ w^{t-\frac{1}{2}} \right) \tag{2.23}$$
$$\left. + C_{56} \left(D_y^+ u^{t-\frac{1}{2}} + D_x^+ v^{t-\frac{1}{2}} \right) \right] \Bigg|_{i,j,k+\frac{1}{2}}^{n+\frac{1}{2}}.$$

$$\tau^{t+1}_{xy|i+\frac{1}{2},j+\frac{1}{2},k+\frac{1}{2}} = \tau^{t}_{xx|i+\frac{1}{2},j+\frac{1}{2},k+\frac{1}{2}}$$
$$+ \Delta t \left[C_{16} D_x^- u^{t-\frac{1}{2}} + C_{26} D_y^- v^{t-\frac{1}{2}} + C_{36} D_z^- w^{t-\frac{1}{2}} \right.$$
$$+ C_{46} \left(D_z^+ v^{t-\frac{1}{2}} + D_y^+ w^{t-\frac{1}{2}} \right) + C_{56} \left(D_z^+ u^{t-\frac{1}{2}} + D_x^+ w^{t-\frac{1}{2}} \right) \tag{2.24}$$
$$\left. + C_{66} \left(D_y^+ u^{t-\frac{1}{2}} + D_x^+ v^{t-\frac{1}{2}} \right) \right] \Bigg|_{i+\frac{1}{2},j+\frac{1}{2},k+\frac{1}{2}}^{n+\frac{1}{2}}.$$

While symmetry genericity is preserved in equations 2.13 to 2.21, I assume typical experiment model parameters to stiffness coefficients of cubic, orthorhombic, and hexagonal symmetry.

2.3.2 Boundary Conditions

Reduction of grid boundary reflections were performed using an exponentially damped "spongey" bounding region that pads the computational domain. Within the absorbing region, an attenuation factor was applied (Cerjan et al., 1985). The discrete representation of this attenuation factor is as follows:

$$A(i) = e^{-\gamma\left(\frac{i}{ni}\right)^2}. \tag{2.25}$$

And a repurposed one-way wave equation absorbing boundary condition was also used as described in Clayton and Enquist (1977).

2.4 NUMERICAL VALIDATION

Simulated wavefield responses over a 1 second time interval from a vertical point force at grid coordinate x $= 0$ and z$= 0$ with a 37.67 Hz Ricker amplitude function from Seismic Unix's "suea2df" program (Juhlin, 1999) and an approximate analytic solution to the elastic-wave equation (Carcione et al., 1998) were compared to that of the finite-difference implementation developed in this thesis. Because the analytic solution to the poroelastic-wave equation is accepted to be approximately equal to the analytic solution to the elastic-wave equation when "Q" parameters, Qp and Qs, increase toward infinity (Fang, et al. 2013), I used values of 25 million for Qp and Qs. The recorded wavefields at an offset of 48 meters and depth of 120 meters are shown for the three algorithms in Figure 2.3. Simulation was performed on a spatially constant computational model with model parameters $v_p = 1732\ m/s$, $v_s = 1000\ m/s$, and a density of 2000 kg/m^3. The root-mean-square error in horizontal component trace amplitude between my implementation and the analytic solution is 0.017731307. Trace outputs of the three simulations, acquired at the receiver position shown in Figure 2.3, are shown in Figure 2.4

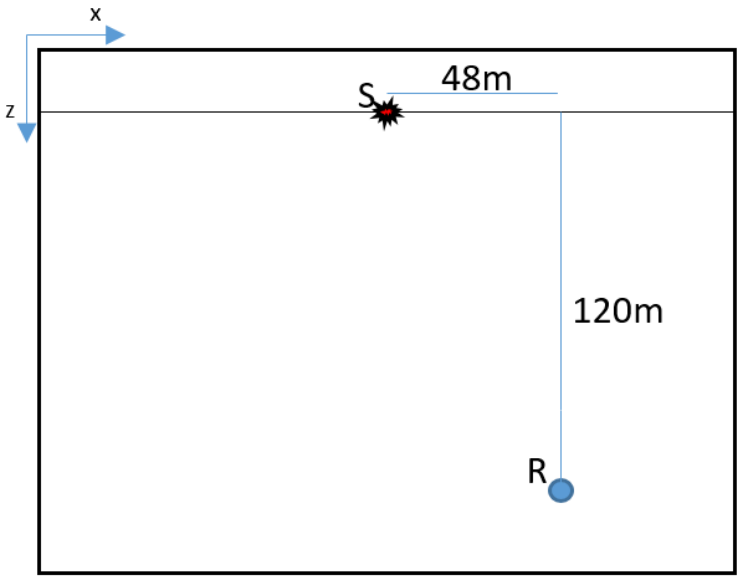

Figure 2.3: Shot and receiver geometry for validation tests. The red "S" illustrates the position of the shot. The blue circle with annotated "R" illustrates the position of the receiver.

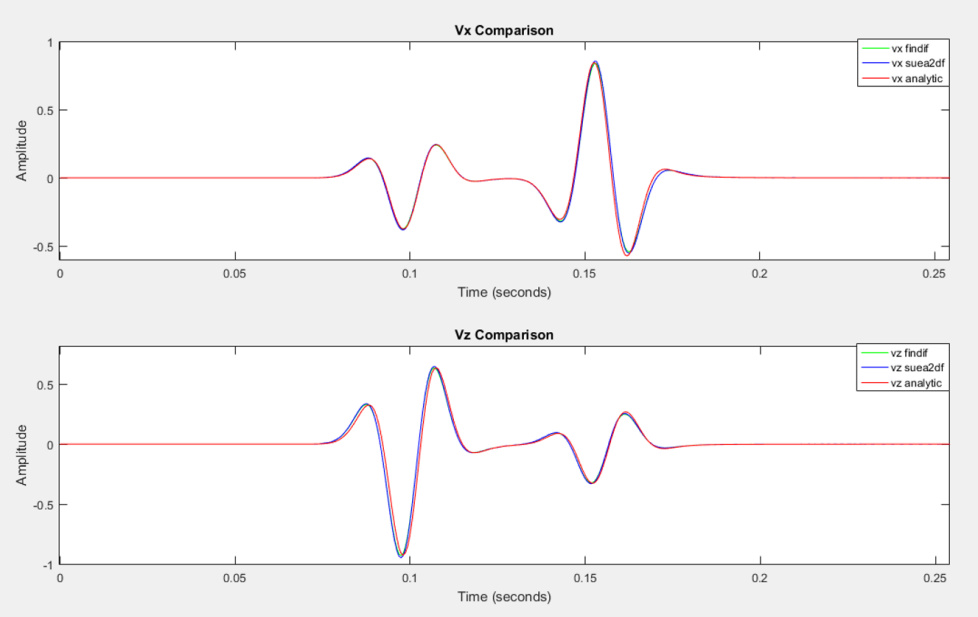

Figure 2.4: Normalized plots of wavefield amplitude at the receiver position illustrated in Figure 2.3. The top plot illustrates the horizontal component of wavefield velocity while the bottom plot illustrates the vertical component of wavefield velocity. The custom implemented algorithm discussed in this chapter is referred to as "findif" and is compared to data simulated by an analytic solution and seismic Unix's suea2df elastic-wave finite-difference solution.

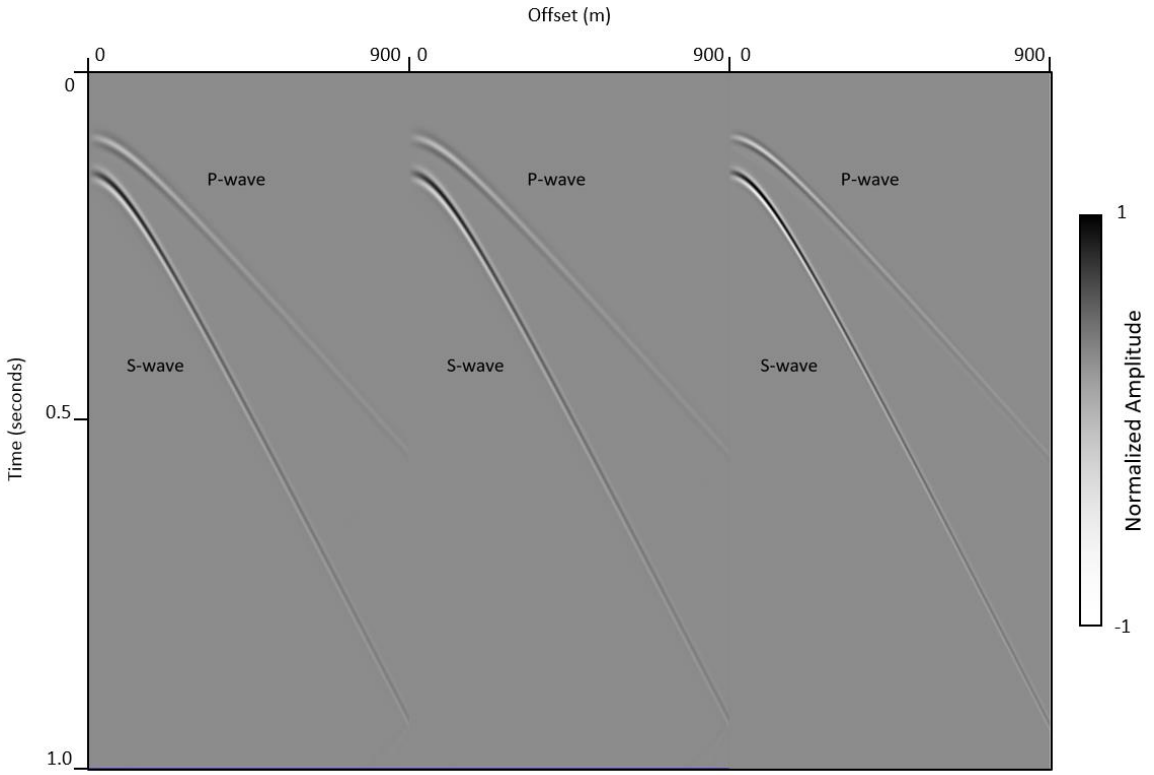

Figure 2.5: The horizontal components of wavefield output from the finite-difference implementation described in this thesis (left), suea2df (middle), and an approximate analytic solution to the elastic-wave equation (right). Receiver line depth is 120 m. Simulation time is 1 second.

My finite-difference implementation in this thesis was developed with Nvidia's CUDA technology for use on an Nvidia Gtx 780 graphics processor card, and a performance comparison of my implementation and that of suea2df's is shown in Figure 2.6.

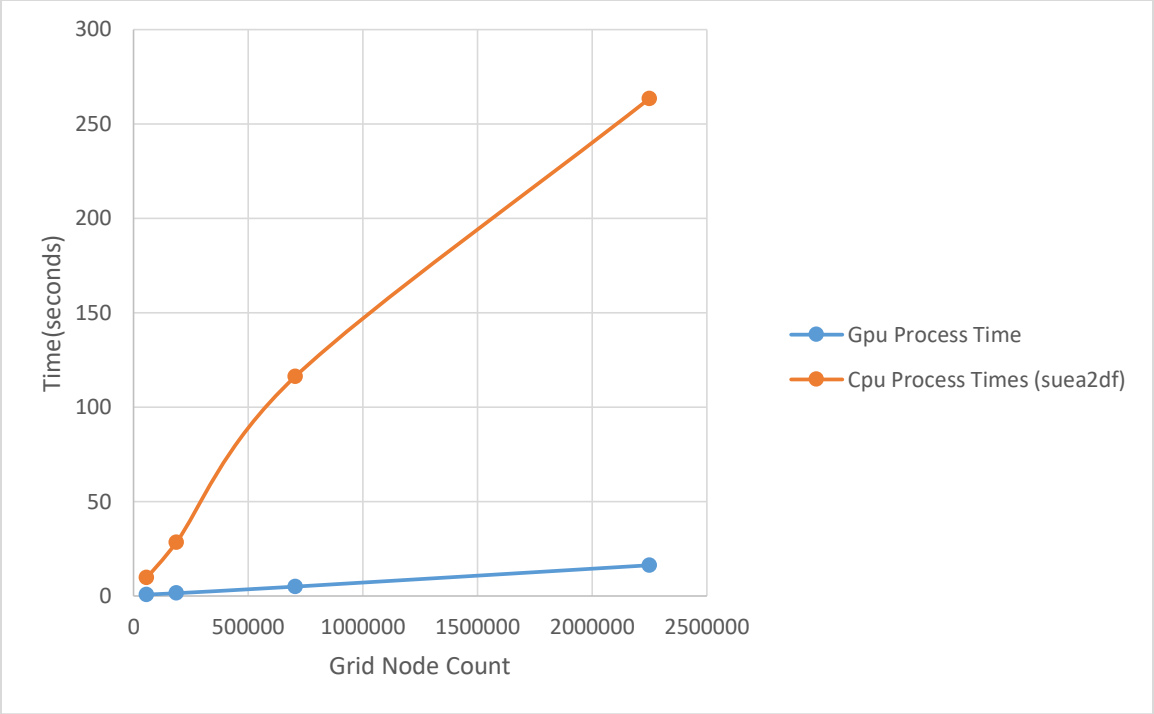

Figure 2.6: A plot of grid node count within a computational domain vs process time.

2.5 CONCLUSIONS

In this chapter, I derived the elastic-wave equation given Newton's first law and Hooke's law for continuum mechanics. I establish a finite-difference approximate solution to the elastic-wave equation in 3D for any arbitrary stiffness symmetry. The 2D implementation of this algorithm was tested for validity by comparing its output to that of Seismic Unix's program, suea2df, and an analytic solution to the elastic-wave equation. Simulation run times of suea2df and my algorithm increases from a serial cpu compared to the parallel gpu processed field differentiation.

Chapter 3. Simulation of elastic-waves through isotropic and anisotropic media.

3.1 INTRODUCTION

The simulation algorithm developed in Chapter 2 is used to create simulated wavefields through a variety of computational models of varying complexity. I focus first on synthetic data generation from various source-functions imparted into the stress and velocity-fields in time. While source wavelet function can vary depending on medium and excitation properties in fractures, Jarillo-Michel and Tsvankin (2015) demonstrated that a wavelet similar to a Gaussian derivative function can be extracted from the direct P-wave arrival of a Microseismic event. I utilize a Gaussian derivative function for the scalar source-function for synthetic examples. I then simulated wave propagation in vertically transversely isotropic media. For each synthetic example, I constructed a computational-grid with wavefield sample acquisition geometries along predefined trajectories similar to that of modern day surface-seismic and vertical-seismic profile surveys. This modeling domain is illustrated in Figure 3.1.

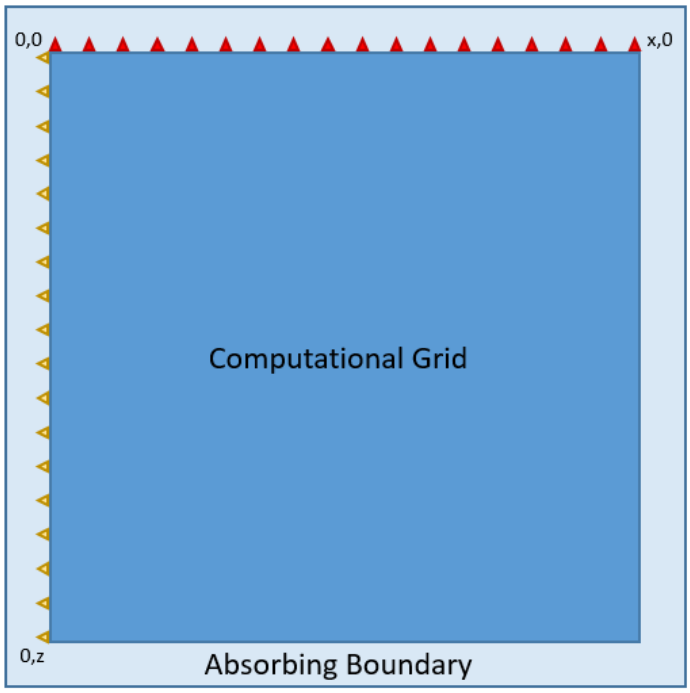

Figure 3.1: The 2D computational domain used for spatially homogeneous simulation examples in this Chapter. Surface receiver lines are illustrated as red triangles, while vertically oriented seismic profile receivers are illustrated as yellow triangles.

3.2 SOURCE-MECHANISMS IN AN ISOTROPIC MEDIUM

For each synthetic example presented in this chapter, I used the research of Aki and Richards (1980) and Eaton (2009) and implemented source injection with Equation 2.7. The stress source injection term uses Equation 3.1 to rotate the source and vary its amplitude.

$$\mu_{ij}(t) = f(t)T_{im}T_{jn}\mu_{mn}. \tag{3.1}$$

Where $\mu_{ij}(t)$ is the stress source imparted into the medium, $f(t)$ is a scalar function of time that represents the amplitude of the energy to be imparted into the medium, T_{mi} and

T_{nj} are rotation matrices where $T = \begin{bmatrix} cos\theta & -sin\theta \\ sin\theta & cos\theta \end{bmatrix}$, and μ_{ij} is the non-rotated stress tensor that describes the structure of the focal-mechanism at a point shown in Figure 3.2.

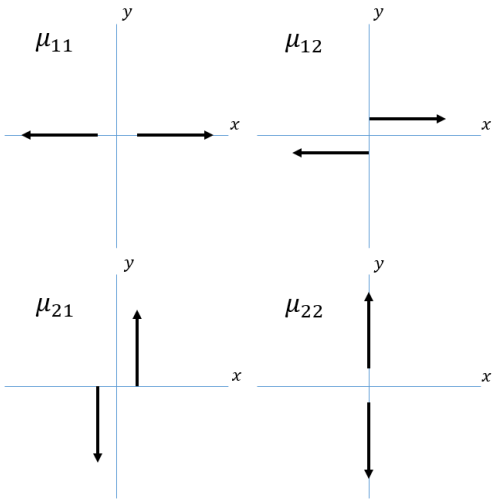

Figure 3.2: The components of a 2D moment-tensor. This is a 2D subset of moment-tensor components described by Aki and Richards, 1980.

The first simulation was executed with a compressional-source, such that $\mu_{12} = 0$, located at the center of the computational-grid at an offset of 600 m and depth of 600 m. Computational-grid-nodes were spaced uniformly at 1.2 m with $v_p = 4800 \frac{m}{s}$ and $\rho = 2650 \frac{kg}{m^3}$. The temporal domain sample rate is 0.0001 s. Figure 3.2 shows the amplitude of the vector valued wavefield resulting from a purely compressional-source-injected into the σ_{11} and σ_{22} components of the stress-field. The time variant function injected into the stress-field is a 70 Hz Gaussian derivative wavelet function. The model parameters used in this example are intended to best approximate model parameters encountered in the middle Bakken formation as illustrated by well logs in Chapter 5 of this thesis.

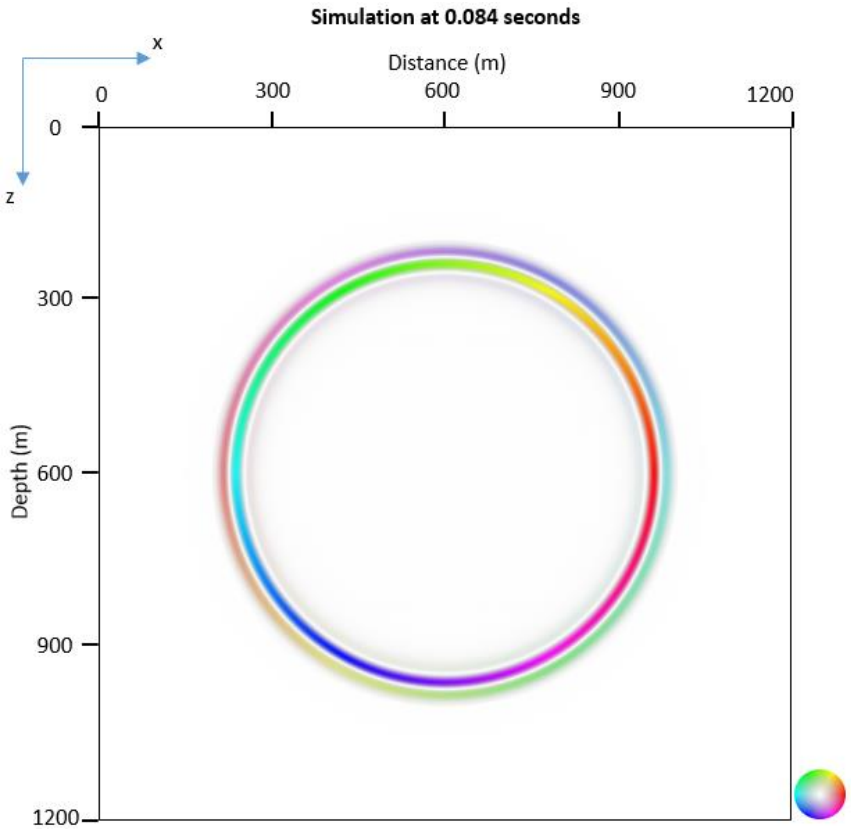

Figure 3.2: A color mapped vector field of a compressional wave 0.084 seconds after source excitation.

Color hue and relative intensity at a 2D coordinate represents vector inclination and relative magnitude, respectively, of the vector. A detailed description of the mapping between a conventional Cartesian coordinate valued vector field and a HSL valued vector field is described in Appendix A. The vector velocity-field is acquired along horizontal and vertical receiver lines positioned at the top and left sides of the computational-grid.

Synthetic seismograms recorded at receiver positions are shown Figure 3.3.

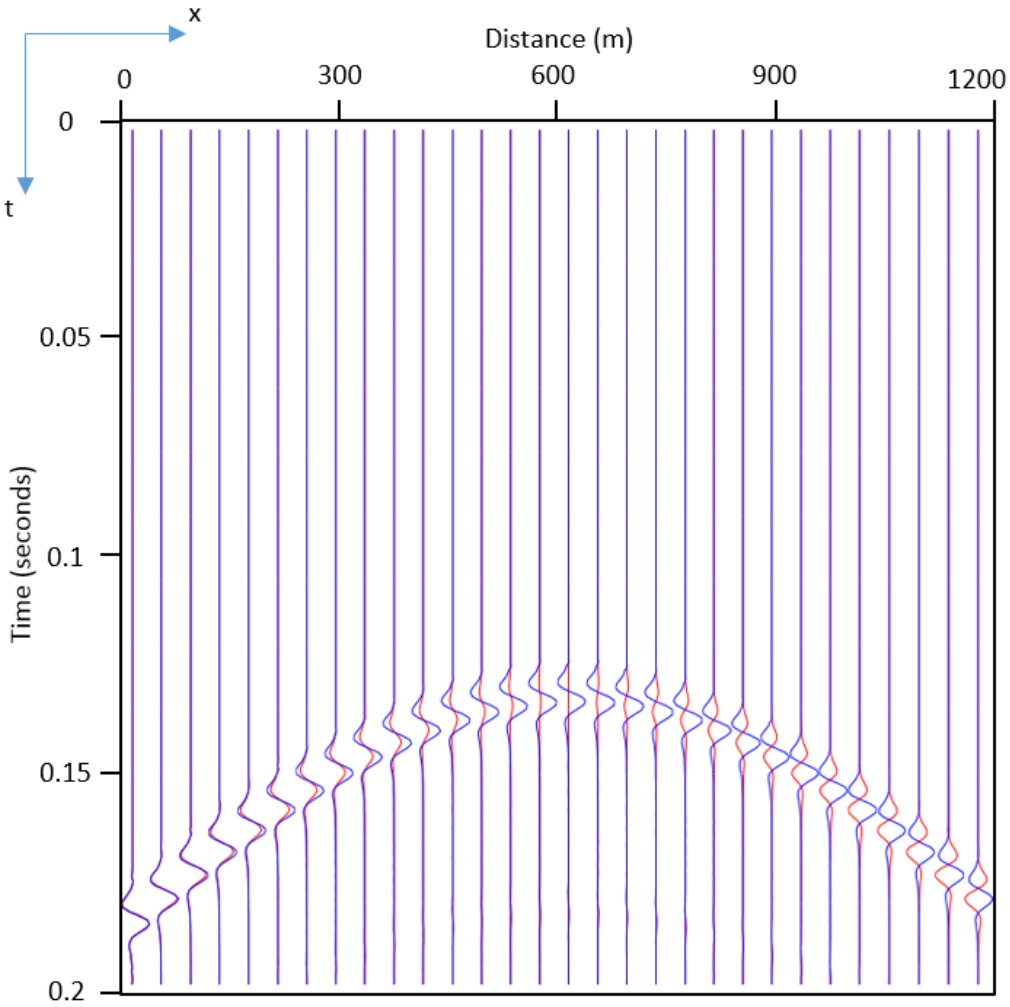

Figure 3.3: Trace records of a compressional-source simulation as recorded along the top boundary illustrated in Figure 3.1. Red trace lines represent the horizontal vector component, while blue trace lines represent the vertical vector component.

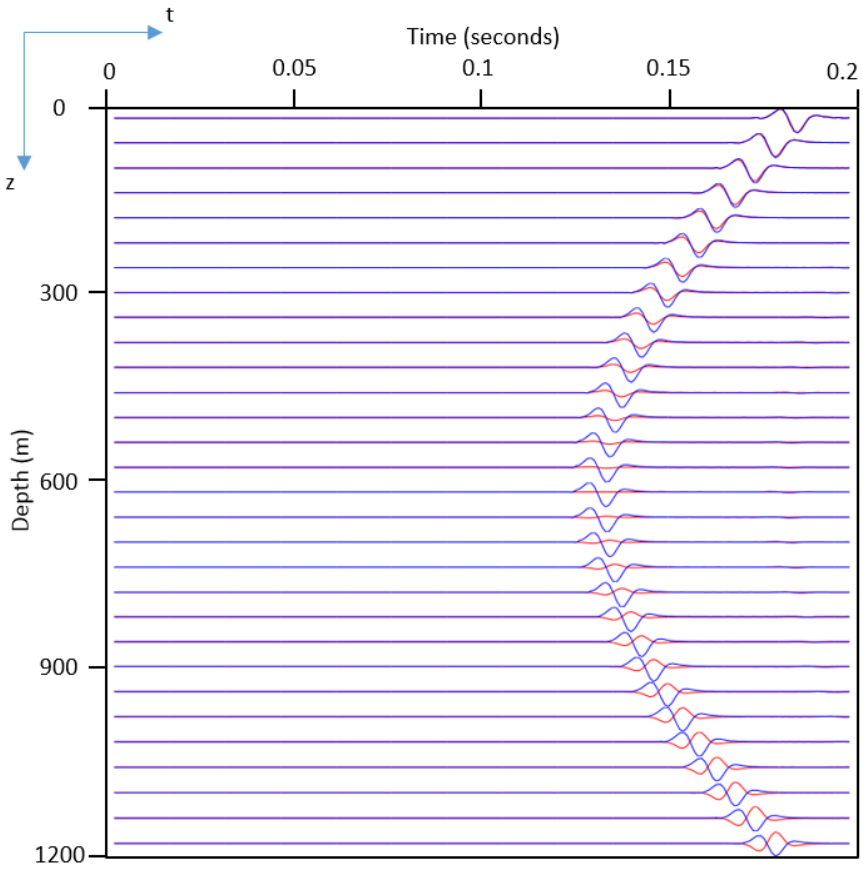

Figure 3.4: Trace records of a compressional-source simulation as recorded along the left vertical boundary illustrated in Figure 3.1 Red traces represent the horizontal vector field component, while blue trace lines represent the vertical vector component.

The double-couple focal-mechanism is a concept described in Aki and Richards (1980) used to model slip along a fracture. Wave propagation due to slip along a fracture has a characteristic radiation pattern that is well known and illustrated in Figure 3.5.

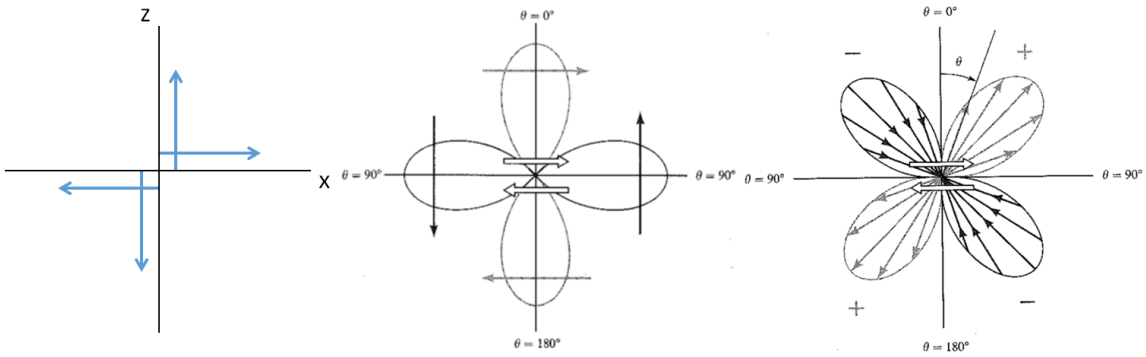

Figure 3.5: The equivalent body force diagram (left) illustrating forces imparted due to a double-couple mechanism. Seismic wave radiation patterns in an isotropic and spatially homogeneous medium that result from a double-couple focal-mechanism. The S-wave amplitude radiation pattern is illustrated in the middle and corresponding P-wave amplitude radiation pattern is illustrated on the right (Aki and Richards, 1980).

The wavefield response due to a double-couple source was simulated. I represent the double-couple focal-mechanism in 2D as a stress tensor with component values of $\mu_{12} = \mu_{21} \neq 0$ and $\mu_{11} = \mu_{22} = 0$. Figure 3.6 illustrates a wavefield excited by a double-couple focal-mechanism with an inclination of 0 degrees, Gaussian derivative source amplitude function, peak wavelet frequency of 70 Hz, and positioned at a grid origin offset of $600\,m$ and depth of $600\,m$. Computational-grid-nodes are spaced uniformly at $2\,m$ with a medium with $v_p = 4800\frac{m}{s}$, $v_s = 2900\frac{m}{s}$, and $\rho = 2650\ \frac{kg}{m^3}$. The temporal domain sample rate is $0.0001\,s$econd. The purpose of this test is to validate wave component amplitude values with respect to position by comparing relative amplitude values to that of the schematics described in Aki and Richards (1980) and illustrated in Figure 3.5.

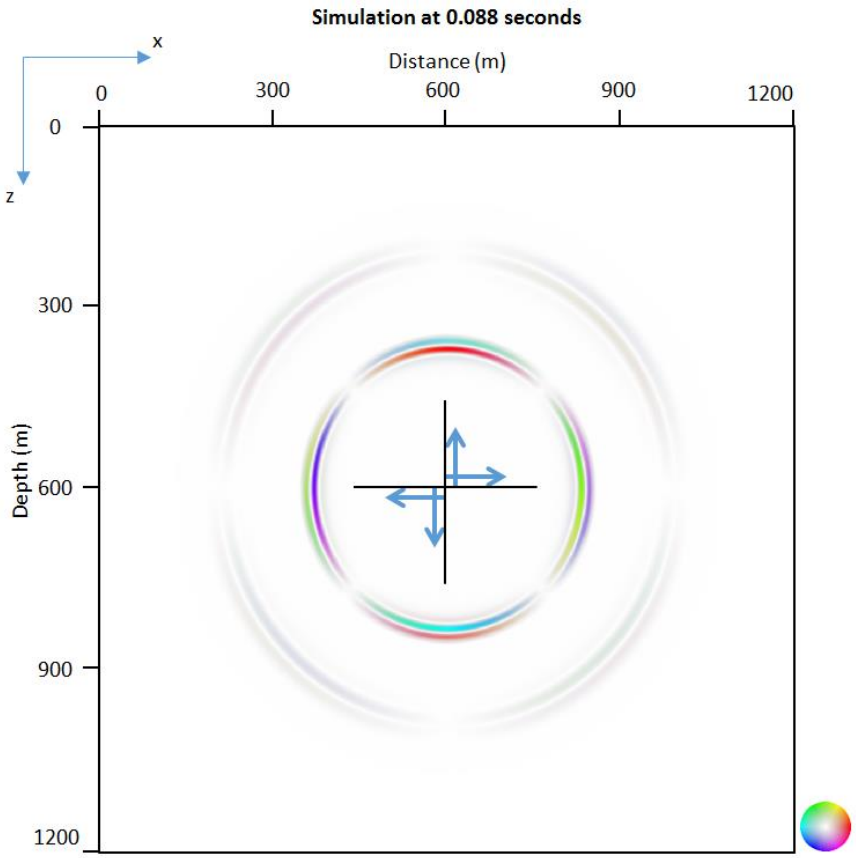

Figure 3.6: A non-rotated double-couple source-injected wavefield at time = 0.088 s. Double-couple equivalent body force diagram is illustrated at the position of source injection.

Similar to the compressional example illustrated in Figure 3.2, receiver positions for the double-couple synthetic example are illustrated in Figure 3.7 and Figure 3.8. Characteristic radiation patterns of a double-couple mechanism are clearly visible in both seismograms (Figure 3.7 and Figure 3.8) as well as the wavefield snapshot in Figure 3.6. The P-wave and S-wave radiation patterns illustrated in Figure 3.6 are identical to that of the radiation patterns illustrated in Figure 3.5. The P-wave component of the total wavefield in Figure 3.6 exhibits zero amplitude along the x axis and z axes while containing maximum amplitude values at 45 degrees with respect to the x and z axes.

Conversely, the S-wave component of the total wavefield in Figure 3.6 exhibits zero amplitude along axes oriented at 45 degrees to the x and z axes.

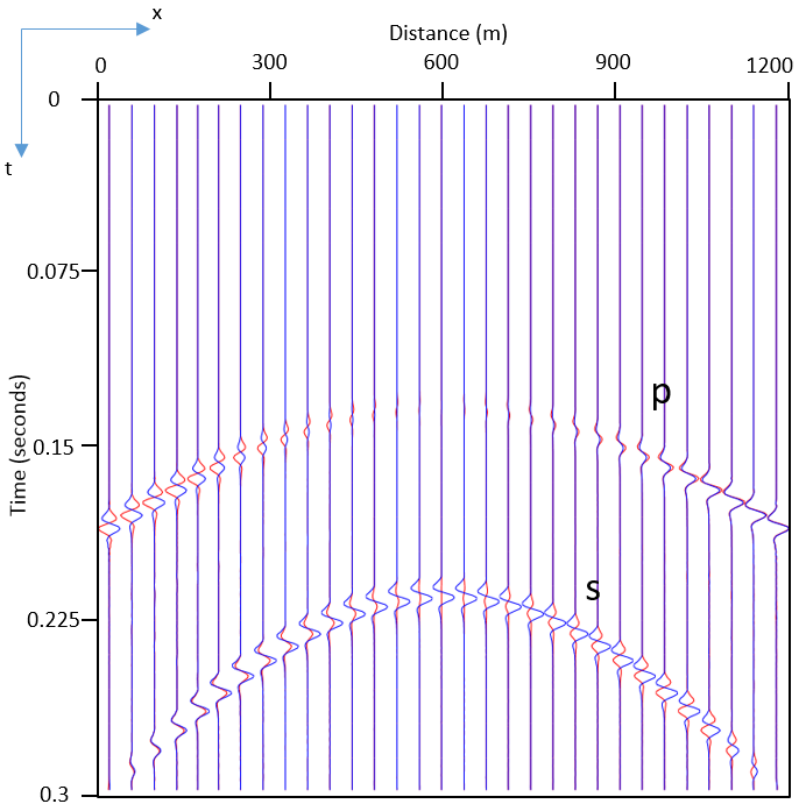

Figure 3.7: Trace records of a non-rotated double-couple source simulation as recorded along the top boundary illustrated in Figure 3.6. Red trace lines represent the horizontal vector component, while blue trace lines represent the vertical vector component.

The trace records illustrated in Figure 3.7 and 3.8 are acquired at the top and left boundary of the computational domain, respectively. Each set of traces exhibits zero amplitude P-wave amplitude regions along the focal-mechanism's simulated slip plane. The zero amplitude S-wave region is also visible in the near and far offset traces.

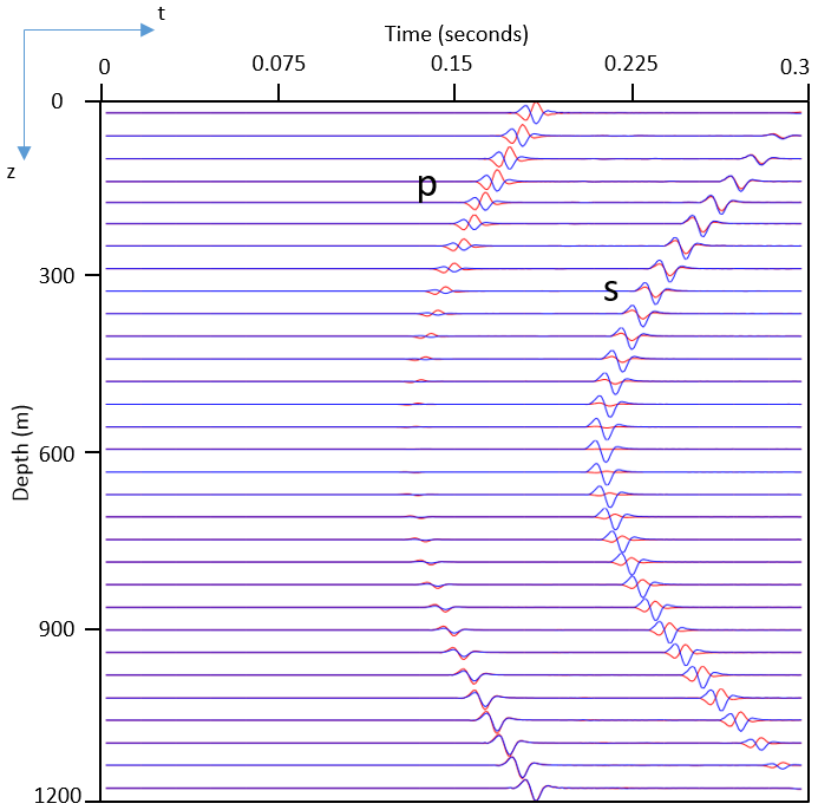

Figure 3.8: Trace records of a non-rotated double-couple source simulation as recorded along the left vertical boundary illustrated in Figure 3.6 Red traces represent the horizontal vector field component, while blue trace lines represent the vertical vector component.

I leveraged Equation 3.1 to rotate our source-mechanism 30 degrees in the counter-clockwise direction. Model, wavelet, and temporal parameters for the rotated example were the same as that of the non-rotated example. Similar radiation patterns to the non-rotated double-couple mechanism example are shown in the trace plots in Figure 3.9 but are rotated 30 degrees compared to their non-rotated counterpart in Figure 3.8. This functionality facilitates simulation of seismic events due to rotated double-couple mechanisms.

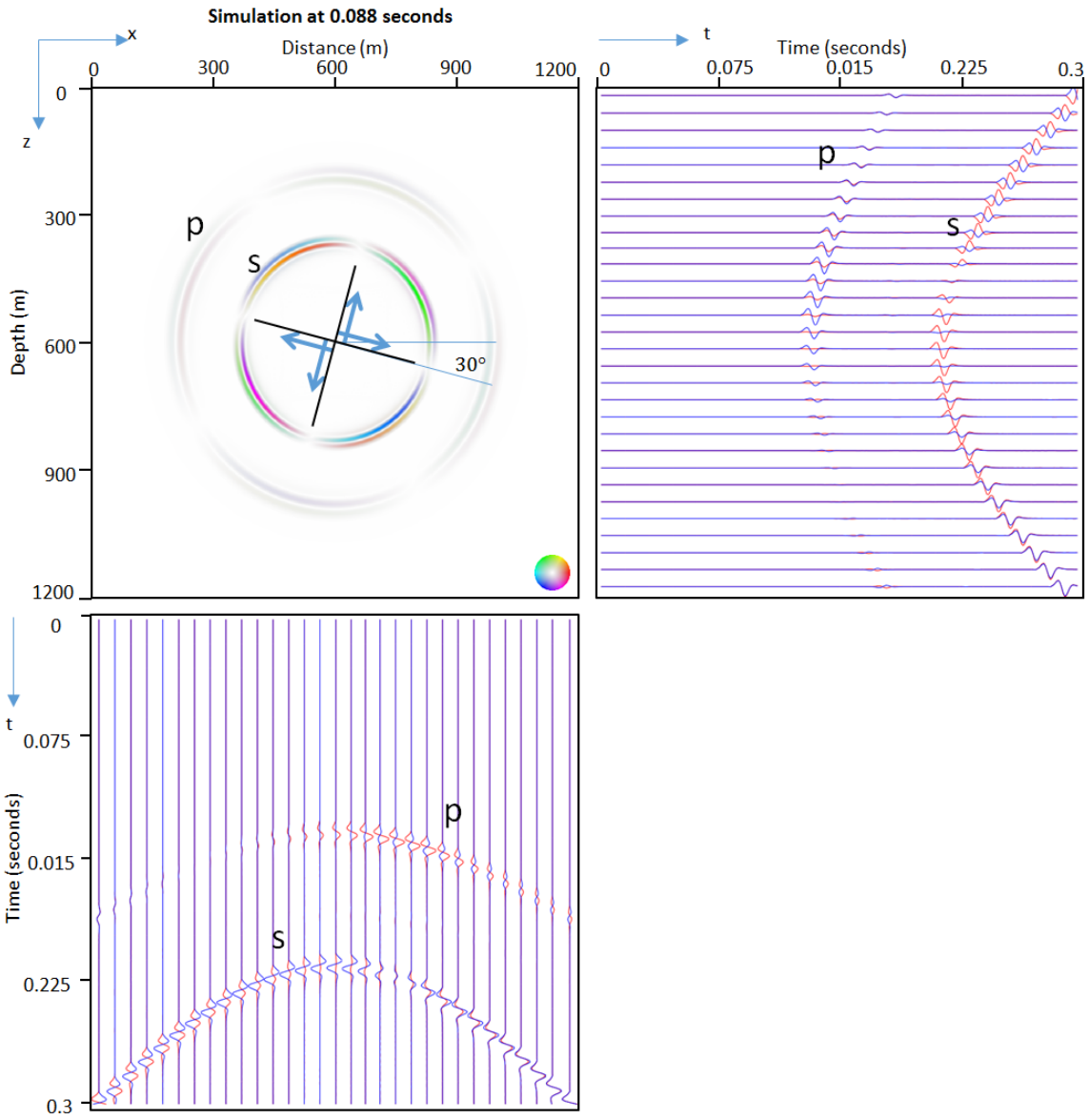

Figure 3.9: A rotated double-couple mechanism injected vector wavefield (top left). Traces from a vertically oriented receiver-set at x = 0 (top right). Traces from a horizontally oriented receiver-set at z = 0 (bottom left).

The rotated double-couple source exhibits wavefield radiation patterns similar to that of the non-rotated double-couple excited wavefield but with a slight rotation to the wavefield in accordance with the rotation of the focal-mechanism. Wavefield acquired at

left and top boundaries also show a rotated P-wave maximum and minimum and S-wave zero amplitude zone with respect to the center trace along each receiver-set.

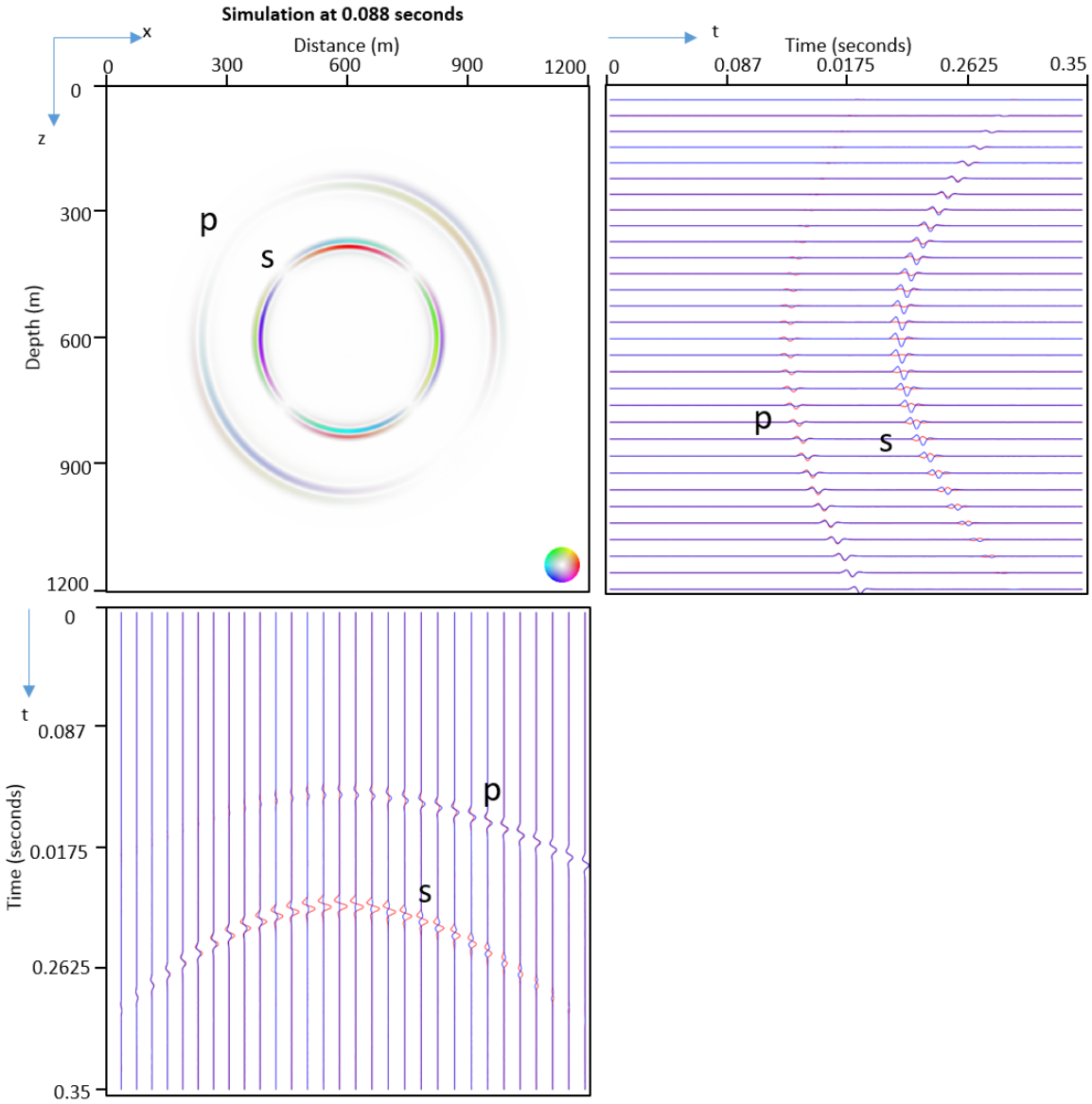

Figure 3.10: A surface recorded trace set (bottom left), vsp recorded trace set (top right), and wavefield snapshot of a combination 50% compressional and 50% double-couple excited wavefield (top left).

To simulate a wavefield generated from a combination of double-couple and compressional-source, I injected 50% of the amplitude of the wavelet function into the source-mechanism's compressional terms and 50% of the amplitude of the wavelet function into the source-mechanism's shear terms. Model and source amplitude function parameters from the non-rotated double-couple source example are reused with this example. The wavefield produced is shown in Figure 3.10 and resembles the characteristic wavefield produced from a double-couple mechanism with energy interfering constructively with the upper-left and lower-right of the P-wavefield, and de-constructively with the lower-left and upper-right portions of the P-wavefield. The shearing component is not affected by the addition of compressional energy to the source-mechanism for the medium demonstrated.

3.3 VERTICALLY TRANSVERSE WAVE PROPAGATION IN A CONSTANT MEDIUM

I continue our demonstration of elastic-wave propagation modeling by demonstrating wave propagation in anisotropic media. Thomsen (1986) has shown that for transversely isotropic (TI) media, the stiffness tensor can be parameterized with three scalar values.

$$\varepsilon = \frac{C_{11} - C_{33}}{2C_{33}}. \tag{3.2}$$

$$\gamma = \frac{C_{66} - C_{44}}{2C_{44}}. \tag{3.3}$$

$$\delta = \frac{(C_{13} - C_{44})^2 - (C_{33} - C_{44})^2}{2C_{44}}. \tag{3.4}$$

Equations 3.2 through 3.4 express the relationship between stiffness tensor and Thomson's parameters. Figure 3.11 shows wave propagation in vertically transversely isotropic media.

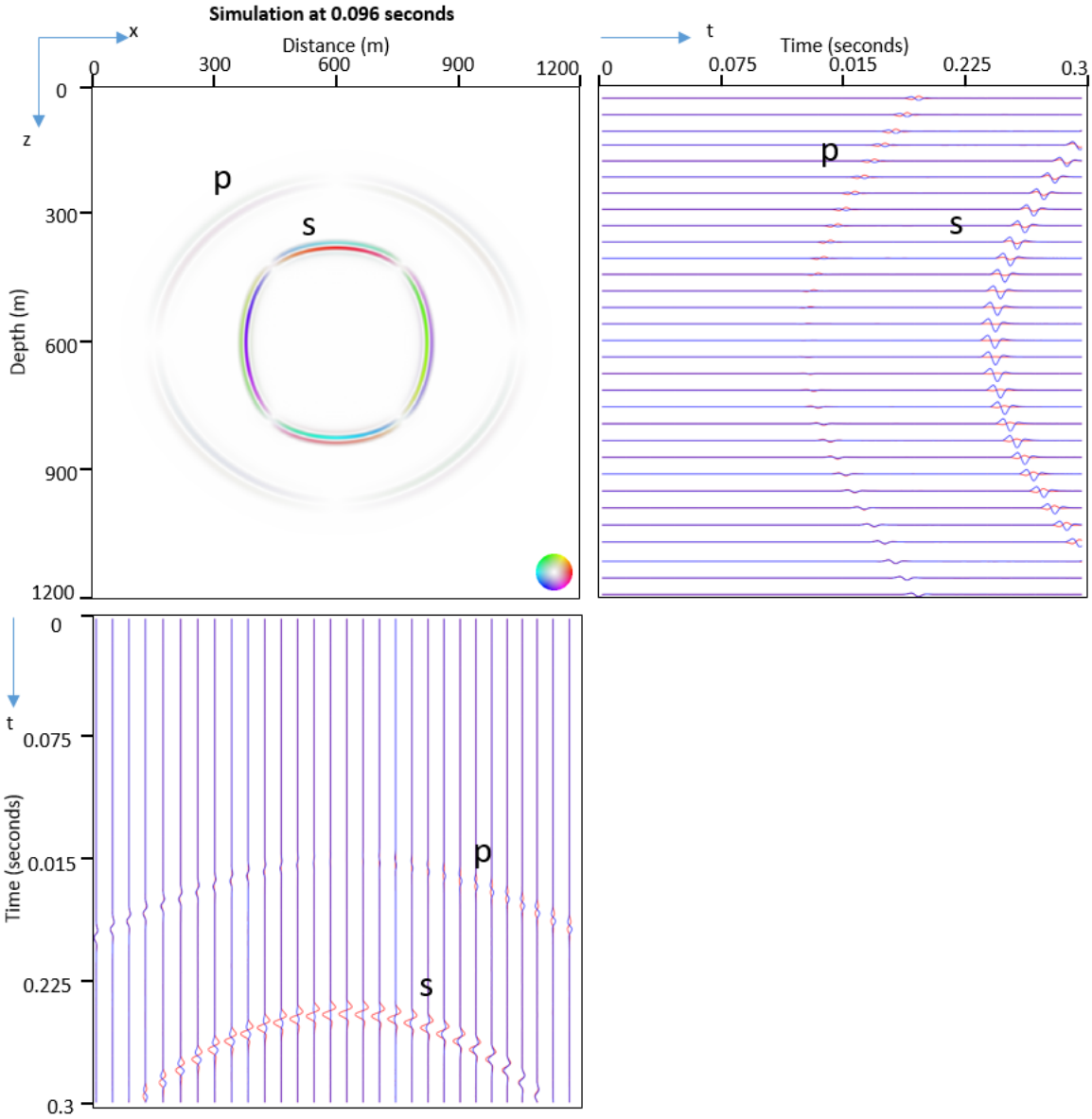

Figure 3.11: A surface receiver-set trace set (bottom left), VSP receiver-set traces (top right), and wavefield snapshot at 0.096 seconds resulting from a double-couple excited wavefield in a VTI medium (top right).

Model parameters for the example illustrated in Figure 3.11 consist of vertical $v_p = 4231\frac{m}{s}$, $v_s = 2539\frac{m}{s}$ and $\rho = 2370\ \frac{kg}{m^3}$ and anisotropic Thomsen parameter values of $\varepsilon = 0.2,\ \delta = 0.1,$ and $\gamma = 0.145.$ These model parameters are used to best simulate wave propagation in an oil shale as described in model parameter examples detailed in Thomsen (1986). The wavelet function is a 70 Hz Gaussian derivative function and injected into the shear components of stress to simulate a double-couple source. Characteristic wave front deformation is similar to wave front geometries communicated in Thomsen (1986) with elliptic shape of the P-wave.

3.4 WAVEFIELD SIMULATION IN THE MARMOUSI 2 MODEL

To simulate elastic-wave propagation in structured non-homogeneous media, a simulation was performed on a subset of the Marmousi 2 model. This subset contains a large normal fault that will be of interest as an imaging target in Chapter 4 of this thesis. I selected a 38 degree clockwise rotated double-couple source at a position within the near vicinity of the fault to best simulate slip along associated fractures that may be present parallel to the fault slip direction nearest the source position. The wavefield was acquired along a vertical set of receivers and near surface positioned receivers as illustrated in Figure 3.12.

Wavefield output illustrated in Figure 3.13, Figure 3.14, and Figure 3.15 demonstrates the complex wavefield interactions that occur during wave propagation in a complex medium. Of particular interest when analyzing wavefield characteristics are the large normal fault, and the high-density formation intersecting the fault from the left at approximately 1335 meters depth.

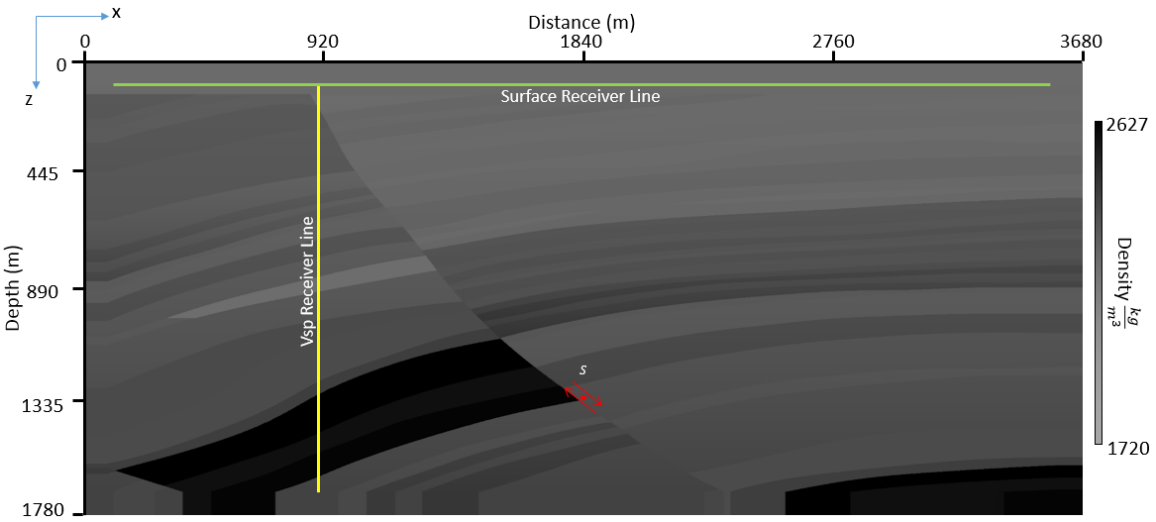

Figure 3.12 : A density model cut from the Marmousi 2 model with source and acquisition geometries illustrated in yellow (vsp receiever line), green (surface receiver line), and red (point source). The point source is positioned in close proximity to the fault and is a double-couple mechanism rotated 38 degrees clockwise such that the slip simulated will be along the direction of the fault line.

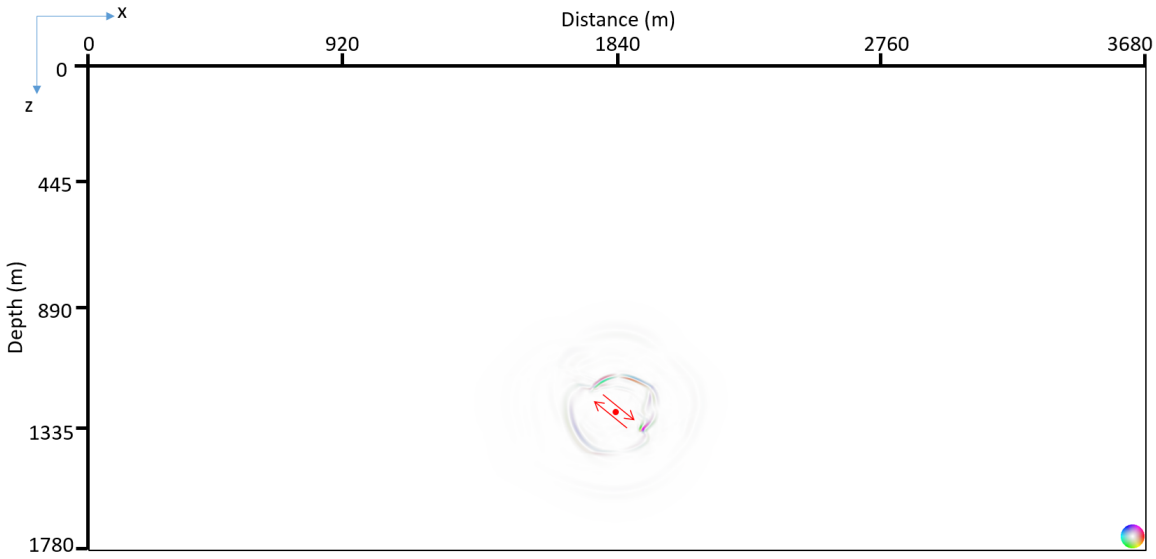

Figure 3.13: A wavefield snap shot at t=0.08 seconds elapsed simulation time. The double-couple source is illustrated with a red circle with its slip directions indicated by red arrows.

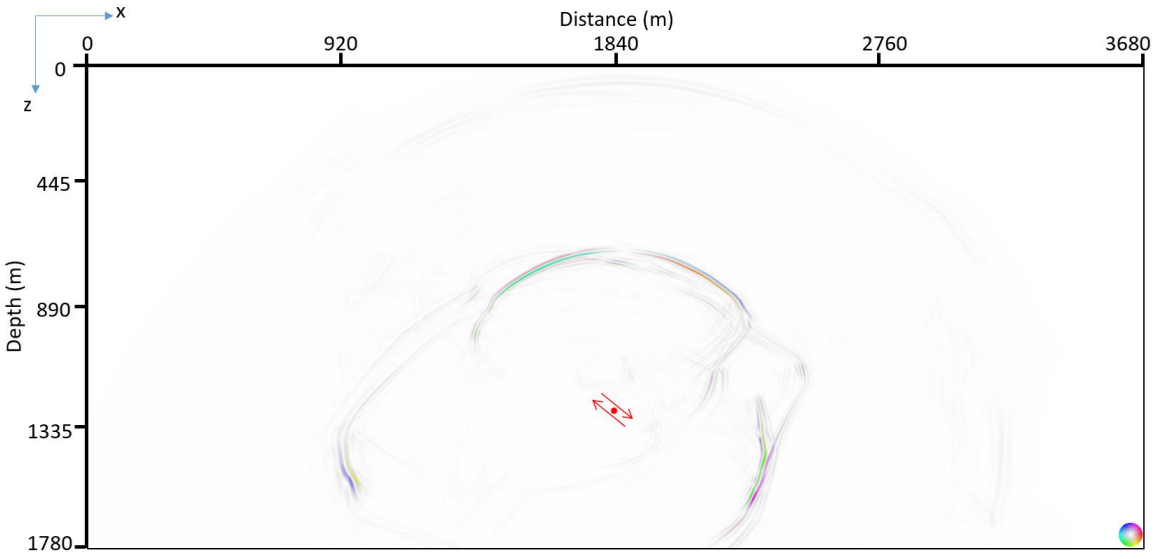

Figure 3.14: A wavefield snap shot at t=0.56 seconds elapsed simulation time. The double-couple source is illustrated with a red circle with its slip directions indicated by red arrows.

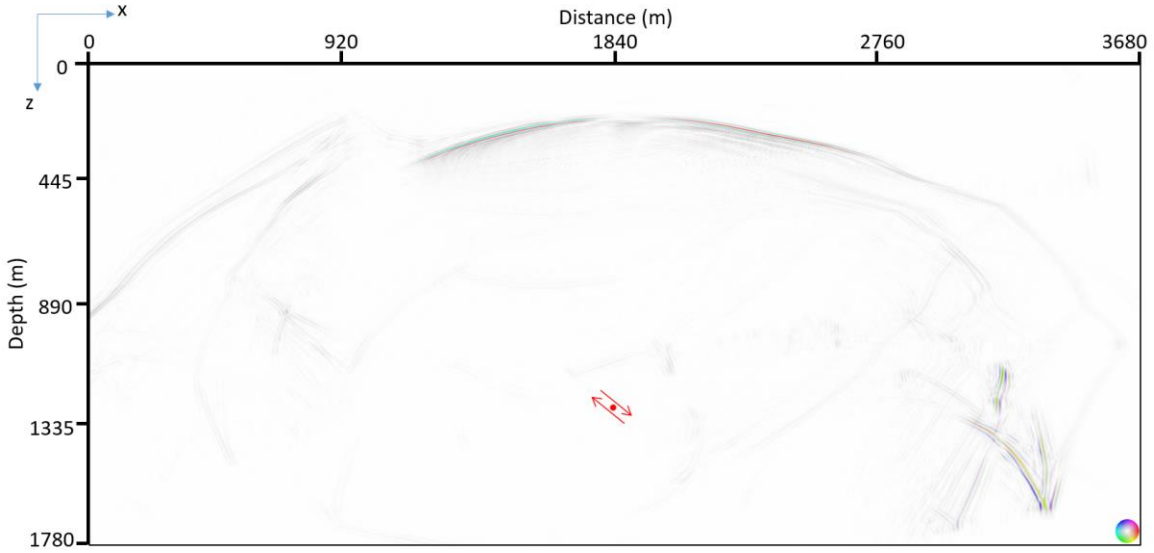

Figure 3.15: A wavefield snap shot at t=1.52 seconds elapsed simulation time. The double-couple source is illustrated with a red circle with its slip directions indicated by red arrows.

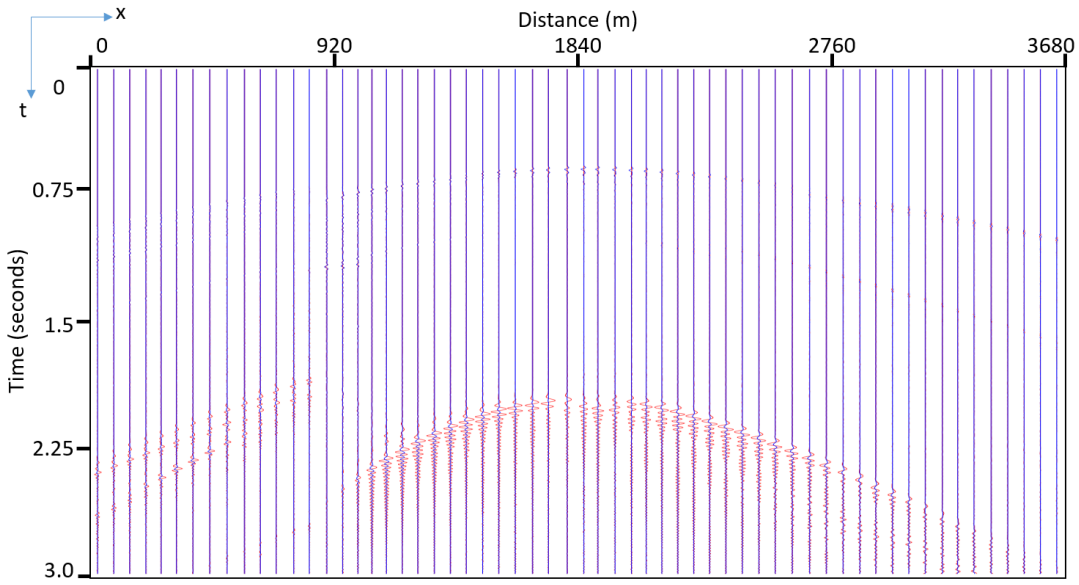

Figure 3.16: Surface acquired traces from the Marmousi 2 simulation example described in this chapter.

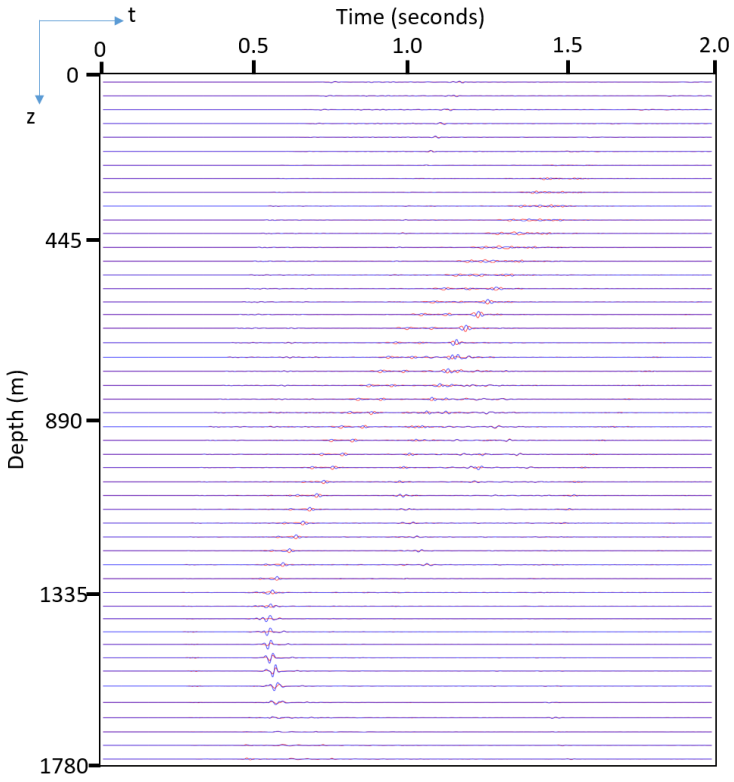

Figure 3.17: Vsp acquired traces from the Marmousi 2 simulation example described in this chapter.

Figure 3.16 and Figure 3.17 illustrate the wavefield acquired at the surface and in a vertical well, respectively. Red colored traces represent the horizontal component of the wavefield. Blue colored traces represent the vertical component of the wavefield. The geometry of the acquisition is illustrated in Figure 3.12.

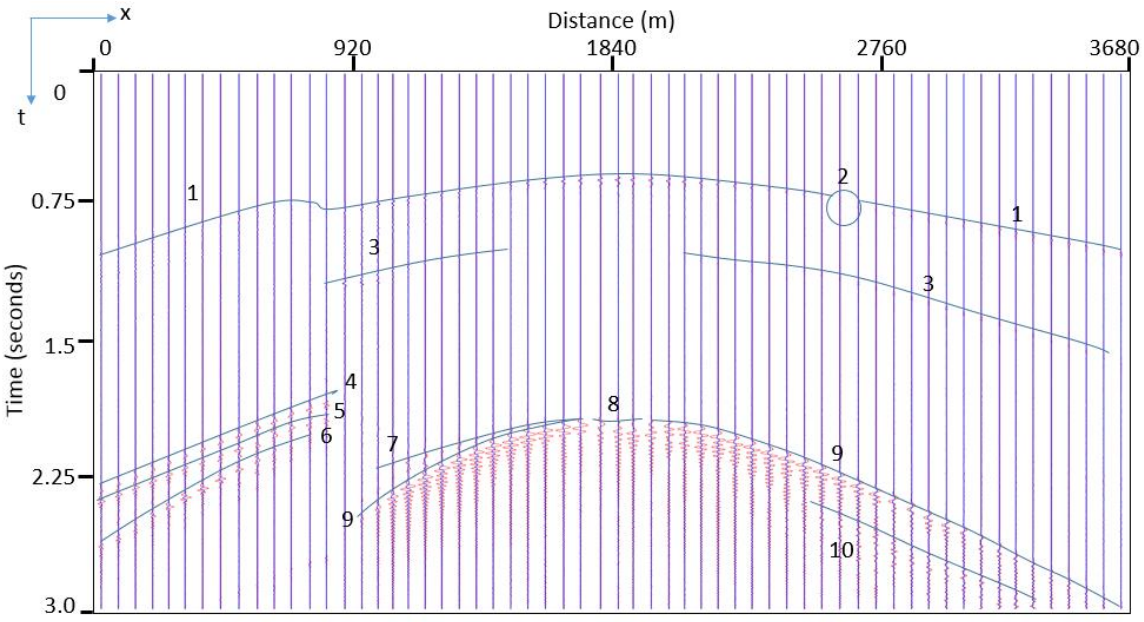

Figure 3.18: Surface-seismic acquired wavefield from the Marmousi 2 fault slip simulation in this chapter. Annotations highlight specific wavefield features of interest. 1 is a P-wave direct arrival. 2 is a zero amplitude P-wave region due to a double-couple induced radiation pattern. 3 is a direct P-wave reflection from the high velocity contact at the large fault. 4 and 9 are direct S-wave arrivals. 5 is an S-wave fault reflection. 6 is a transmitted refraction from the direct S-wave from the right of the fault to the left of the fault. 7 is a high density formation produced head wave at the fault from the S-wave. 8 is a fault reflected S-wave.

The surface acquired wavefield exhibits several notable characteristics that are illustrated and annotated in Figure 3.18. The P-wave direct-wave is annotated with the number 1 and is the first sampled response due to the double-couple source. The discontinuity in the P-wave direct-wave at x~900 exists due to the presence of the fault and direct-wave scattering along the trajectory of the fault. The discontinuity highlighted

at annotation number 2 is the zero amplitude radiation zone of the P-wave due to the characteristic radiation pattern of the double-couple mechanism. Annotation 3 P-wave reflection from the high density region to the left of the large fault illustrated in Figure 3.12. Annotations 4 and 9 are S-wave direct-waves with a discontinuity between the two features at x~900 due to the fault. The direct S-wave wave illustrated by annotation 9 is split by annotation 8 at the zero amplitude S-wave region described by the characteristic double-couple induced S-wave radiation pattern. Annotation 8 is a fault-induced reflection of the direct S-wave. Annotation 5 is an S-wave reflection from the bottom of the high-density formation to the left of the fault, and annotation 6 is a transmitted refraction of the direct S-wave from the right of the fault to the left of the fault. Annotation 7 is a head wave produced from the fault contact with the high-density formation and its interaction with the direct S-wave.

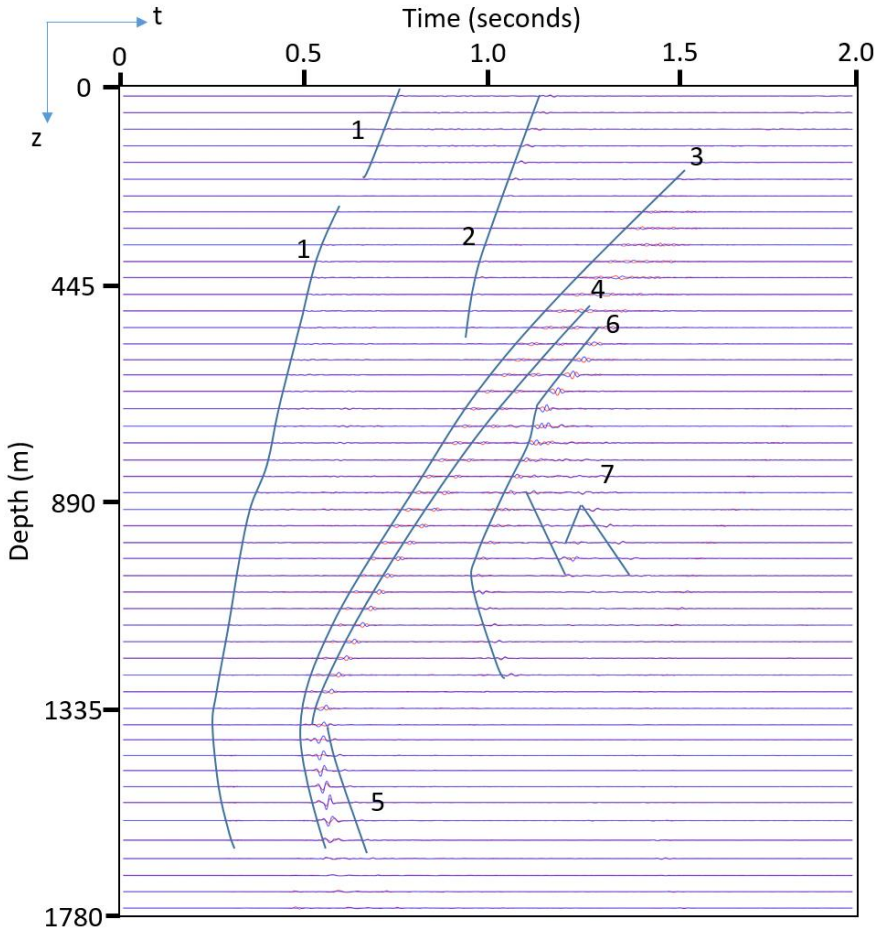

Figure 3.19: Vsp acquired wavefield from the Marmousi 2 fault slip simulation in this chapter. Annotations highlight specific wavefield features of interest.

The Vsp acquired wavefield is illustrated in Figure 3.19 with wavefield features annotated in frame. Annotation 1 is the direct P-wave arrival. Annotation 2 is a refracted P-wave from the top of the low-density zone illustrated in Figure 3.12 at a depth of z~830 meters. The direct S-wave arrival is annotated with the number 3. Annotation 4 highlights an S-wave reflection from the bottom of the high-density formation intersecting the fault from the left at z~1335. Annotation 5 is a mode converted down going P-wave produced from the direct S-wave. The upward propagating direct S-wave interacts with the fault and transmits a refracted S-wave in annotation 6. Annotation 7

highlights internal multiple reflections resulting from interfaces bounding the formation below the low density region.

3.5 CONCLUSIONS

In this chapter, I demonstrate the ability of the algorithm described in this thesis to simulate elastic-wave propagation in isotropic and anisotropic media. I also demonstrate the algorithm's ability to simulate multiple and combined source types. A simulation of a fracture via double-couple source injection near a large fault in a Marmousi 2 subset model is performed and data acquired along the surface and a vertical seismic profile. Wavefield characteristics and features were annotated and described in detail.

Chapter 4. Elastic reverse-time migration for vertical arrays

4.1 INTRODUCTION

Reverse-time migration (RTM) is a well-documented depth imaging technique that has been gaining popularity in the surface-seismic depth processing community. While initial propositions for reverse-time migration methods were made by Baysal et al. (1983), McMechan (1983) and Whitmore (1983), the technological requirements for practical applications of RTM proved too cumbersome given the computational functionality at the time. Recent technological advances in high-throughput parallel processing and IO and storage capacity have provided financial and functional feasibility for processors to popularize RTM as a common depth imaging technique (Yao, 2013).

While conventional applications of reverse-time migration have focused on depth migration of surface acquired seismic data, there have been some applications of borehole acquired seismic reverse-time migration. Lu et al. (2006) demonstrates the practicality of imaging salt dome flanks via reverse-time migration of compressional components of seismic data acquired in a vertical borehole adjacent to the imaging targets of the salt dome.

In this chapter, I present a modified elastic reverse-time migration imaging condition that removes source and receiver artifacts, demonstrates the practicality of elastic RTM in a borehole setting given source and receiver geometries similar to that of modern day perforation source borehole seismic monitoring.

4.2 REVERSE-TIME MIGRATION

RTM has been described as the time domain cross-correlation of spatially and temporally extrapolated source and receiver wavefields. Its scalar field representation has been given by Claerbout (1971).

$$i_s(x) = \int u_s(x,t)u_r(x,t)dt. \tag{4.1}$$

Where $i_s(x)$ is known as an imaging condition for a particular point source 's', u_s is the scalar wavefield extrapolated in space and time of a point source s, and u_r is the scalar wavefield extrapolated in space and time at receiver coordinates whose point source amplitude is represented by the reversed receiver functions in time. Creation of this imaging condition relies on the processor's ability to extrapolate a wavefield in time and space from a known set of sources. Specifically, reverse-time migration utilizes the simulation or modeling functionality of finite-difference approximate wave equation solutions in order to extrapolate a forward wavefield in time and space. The result of the forward wavefield extrapolation is cross-correlated in time with the extrapolation of the receiver wavefield, such that each geophone record acts as a point source where its amplitude function is the time-reversed trace in time during extrapolation. Reverse-receiver source-extrapolated wavefields are also commonly referred to as adjoint-wavefields to the source wavefield. Resultant fields from the time based cross-correlation of the forward wavefield and its adjoint-wavefield are typically summed or stacked for each source-receiver-set pair in order to obtain a final image product.

$$I(x) = \sum_s i_s(x). \tag{4.2}$$

Elastic reverse-time migration expands on the foundation established in Equation 4.1 and describes the imaging condition regarding a vector field.

$$i_{ij}(x) = \int u_i^s(x,t) u_j^r(x,t) dt. \tag{4.3}$$

The implementation expressed in Equation 4.1, 4.2, and 4.3 relies on the notion that for conventional surface-seismic acquisition source and receiver-set geometries, the cross-correlation of the source and receiver wavefields extrapolated in time and space will contain amplitude illumination at a common reflection point. Surface-seismic acquisition geometry is not the same as that of a VSP receiver-set acquiring a perforation shot excited seismic wave. For a 2D discrete implementation of the elastic imaging condition expressed in Equation 4.3, a matrix valued imaging condition is created from:

$$i_{ij}^s(\boldsymbol{x}) = \begin{bmatrix} \sum_t u_1^s(\boldsymbol{x},t) u_1^r(\boldsymbol{x},t) & \sum_t u_1^s(\boldsymbol{x},t) u_2^r(\boldsymbol{x},t) \\ \sum_t u_2^s(\boldsymbol{x},t) u_1^r(\boldsymbol{x},t) & \sum_t u_2^s(\boldsymbol{x},t) u_2^r(\boldsymbol{x},t) \end{bmatrix}. \tag{4.4}$$

Field component values u_1 and u_2 can represent Cartesian coordinate reference system components or P- and S-wave modes. Each parameterization presents benefits and issues. Cartesian coordinate component representation is efficient in computation, because wavefields are computationally represented and differentiated in this state, however, mode conversions and inconsistent wavefield features between forward and adjoint-wavefields present "crosstalk" artifacts. To mitigate "crosstalk", P- and S-wave phase parameterization can be used but requires extra computational steps and memory allocation (Yan and Sava, 2008). For this reason, I constructed the imaging condition

with P- and S-wavefield components. For isotropic stiffness models, Helmholtz decomposition method shown in Equation 4.5 may be performed.

$$u_p = \nabla \cdot u_i.$$
$$u_s = \nabla \times u_i. \tag{4.5}$$

The Helmholtz decomposition used in Equation 4.5 satisfies requirements of wave mode separation for isotropic stiffness tensor models but is not satisfactory for anisotropic stiffness tensor models due to the non-orthogonality of the wave propagation direction with respect to the wavefield vector direction. Wavefield-separation techniques for anisotropic stiffness tensor models are explored in Yan and Sava (2009), but are not explored in this thesis.

4.3 SOURCE AND RECEIVER ILLUMINATION ARTIFACTS

Differences in acquisition geometry of conventional surface-seismic surveys and vertical-seismic profiling surveys is important when considering implementation details of the reverse-time migration algorithm used. Source illumination artifacts occur from high-wavefield amplitudes at the source position near the initial simulation time multiplied with the low-amplitudes of the adjoint-wavefield. Artifacts decrease in amplitude from the source of the forward wavefield as simulation time increases and spherical spreading of the source wavefield occurs. An attempt to remove source illumination artifacts was suggested by Jiang (2009) and described in Equation 4.6. This equation suggests that source artifacts can be removed by dividing by the autocorrelation of the source wavefield.

$$I(\boldsymbol{x}) = \frac{\int u_x^s(\boldsymbol{x},t)u_x^r(\boldsymbol{x},t) + u_x^s(\boldsymbol{x},t)u_y^r(\boldsymbol{x},t) + u_y^s(\boldsymbol{x},t)u_x^r(\boldsymbol{x},t) + u_y^s(\boldsymbol{x},t)u_y^r(\boldsymbol{x},t)dt}{\int u_x^s(\boldsymbol{x},t)u_x^s(\boldsymbol{x},t) + u_y^s(\boldsymbol{x},t)u_y^s(\boldsymbol{x},t)dt}. \quad (4.6)$$

Receiver illumination artifacts in a surface-seismic reverse-time migration image tend to be small when compared to that of a vertical seismic profile. The difference in receiver illumination magnitude occurs from the difference in wave path geometry in the two different surveys. In surface-seismic surveys, a large amount of downgoing wavefield energy is not acquired by receivers at the surface due to transmitted energy away from the receiver geometry.

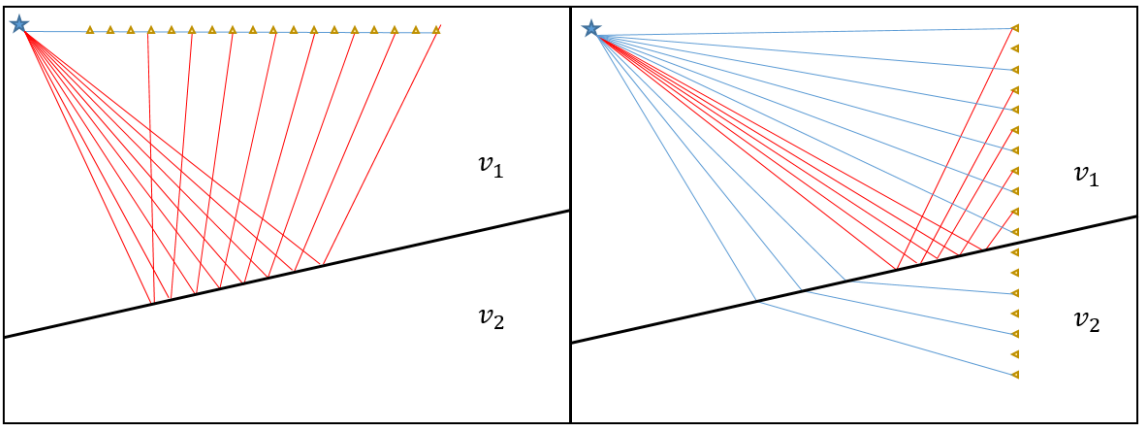

Figure 4.1: Ray paths for a surface-seismic acquisition survey (left), and a vertical seismic profile survey (right). The star represents a source position, yellow triangles represent receiver positions; red lines represent reflected energy, blue lines represent direct arrival ray paths, and the black line is a dipping interface between two velocity media.

Reflected energy is almost entirely used in isolation when constructing the adjoint state wavefield. Conversely, vertical-seismic profile surveys tend to record much more energy from the direct arrival than their surface-seismic counterpart. Because of the presence of large-amplitude direct-arrival energy in vertical seismic profiles, there exist

much larger amplitude receiver illumination artifacts when attempting to perform reverse-time migration on vertical-seismic profile acquired data.

I suggest a modified form of Equation 4.6 to accommodate receiver illumination artifact in the form of Equation 4.7.

$$I(\boldsymbol{x}) = \frac{\int u_1^s(\boldsymbol{x},t)u_1^r(\boldsymbol{x},t) + u_1^s(\boldsymbol{x},t)u_2^r(\boldsymbol{x},t) + u_2^s(\boldsymbol{x},t)u_1^r(\boldsymbol{x},t) + u_2^s(\boldsymbol{x},t)u_2^r(\boldsymbol{x},t)dt}{\int u_1^s(\boldsymbol{x},t)u_1^s(\boldsymbol{x},t) + u_2^s(\boldsymbol{x},t)u_2^s + u_1^r(\boldsymbol{x},t)u_1^r(\boldsymbol{x},t) + u_2^r(\boldsymbol{x},t)u_2^r(\boldsymbol{x},t)dt}. \quad (4.7)$$

Equation 4.7 includes a receiver auto-correlation term in the denominator to accommodate receiver artifacts. Component indices in 4.7 refer to either of the previously mentioned parameterizations of a vector. While the scalar and acoustic nature of Equation 4.1 incorporates only reflected compressional energy, Equation 4.7 elaborates on the characteristics of Equation 4.1 by incorporating reflectivity, transmission, and mode conversion into the image product from each component of the image matrix in Equation 4.2. I tested our elastic reverse-time migration imaging algorithm on a set of synthetic examples

4.4 IMAGING OF A SINGLE-DIFFRACTOR

I created a 2D synthetic model containing a single-diffraction square structure at the center of a constant velocity and density model. The diffraction structure has a width and height of 6 m. The computational model is a 200 x 200 node grid with a 1.2 m spacing between adjacent nodes in both the horizontal and vertical directions. I use a 90 Hz Gaussian derivative function and compressional-source for each of the eight extrapolated shots. Source set geometry was intended to be representative of the geometry found within a set of perforation shots in a lateral well and is shown in Figure 4.2. The

computational model has an ambient velocity of $v_p = 1400m/s$ and $v_s = 800m/s$, and an ambient density of $\rho = 800\ kg/m^3$. The diffractor is a high velocity and density structure with values of $v_p = 2500m/s$, $v_s = 1500m/s, and\ 2000\ kg/m^3$. I created a horizontal compressional-source set with each source evenly spaced at across the medium. A receiver line is also created to acquire the wavefield along a vertical seismic survey with geophone spacing along the trajectory at 2.4 m. The synthetic experiment setup is shown in Figure 4.2. My aim was to simulate synthetic data acquired at the receiver line from shots S_1 through S_8 and execute imaging condition algorithm by assuming known physical property model, source and receiver position parameters.

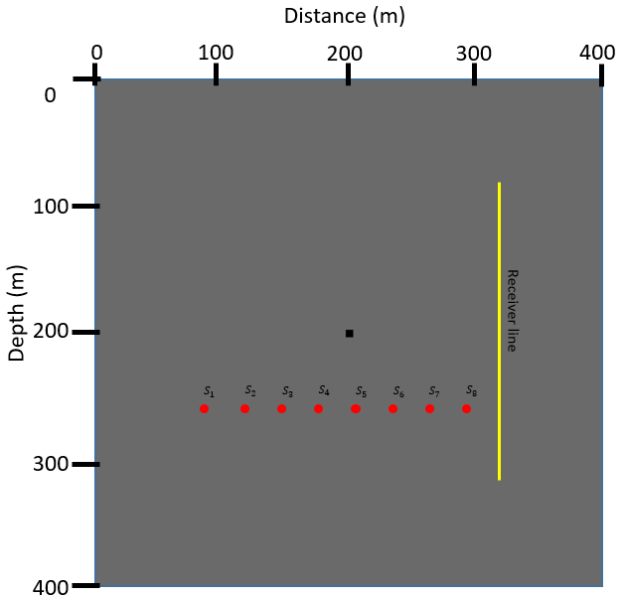

Figure 4.2: The survey geometry setup with sources illustrated in red, geophone line illustrated in yellow. The computational-density model is illustrated in the background showing the diffraction square structure in black with ambient model value in gray.

Individual shot images were created for each source using Equation 4.7. These images shown in Figure 4.4 as a set of shot images. Each shot image was indexed and is

associated with its corresponding shot index as shown in Figure 4.2. Imaging artifacts are present in each image from a lack of swath coverage in the receiver line. An ideal receiver geometry would encapsulate the imaging target and source at all (Fish 2012). Images are from each shot are summed to create the full stacked image. Image stacking effectively eliminates artifacts that do not constructively interfere with each other by illuminating common image structures. This stacked image is shown in Figure 4.5

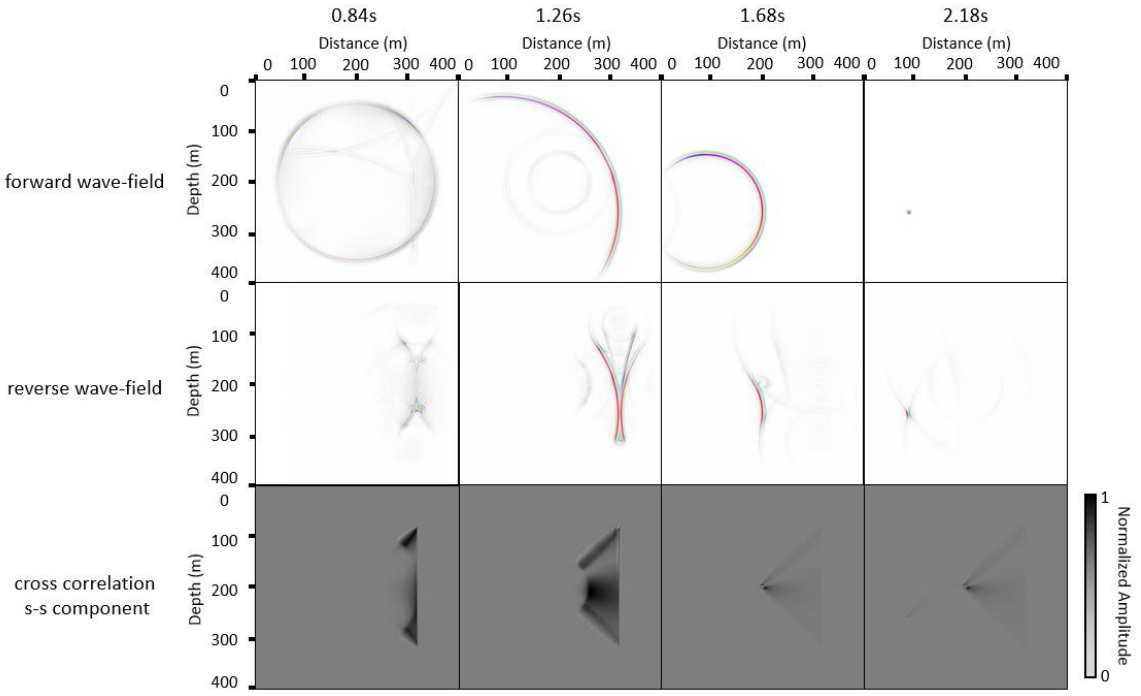

Figure 4.3: Reverse-time migration image construction. Columns illustrate forward, reverse, and cross-correlation wavefields as a progression in constructing a reverse-time migration image.

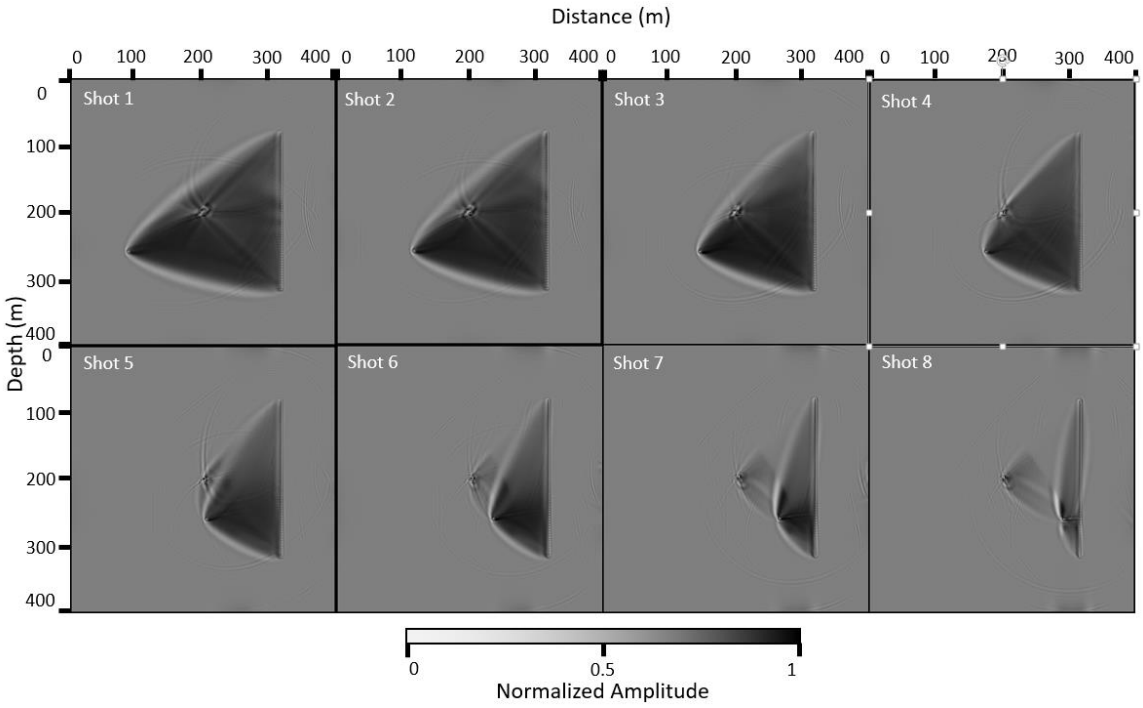

Figure 4.4: Images produced from reverse-time migration of the single-diffraction structure model shown in Figure 4.2. Shot images are organized and illustrated with their corresponding shot index either above or below it.

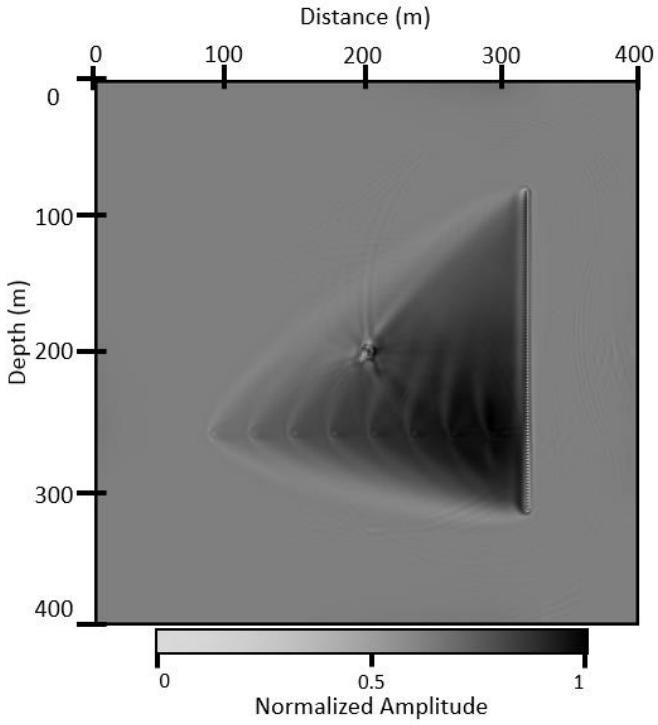

Figure 4.5: The stacked image from shots illustrated in Figure 4.4.

While the stacked image illustrated in Figure 4.5 eliminates some artifacts present in shot images 1 through 8, residual-artifacts are present in the form of low-amplitude source and receiver illumination artifacts with some crosstalk and diffraction artifacts where the source and receiver wavefields interfere constructively during cross-correlation. A derivative operator executed in the vertical domain can remove these artifacts.

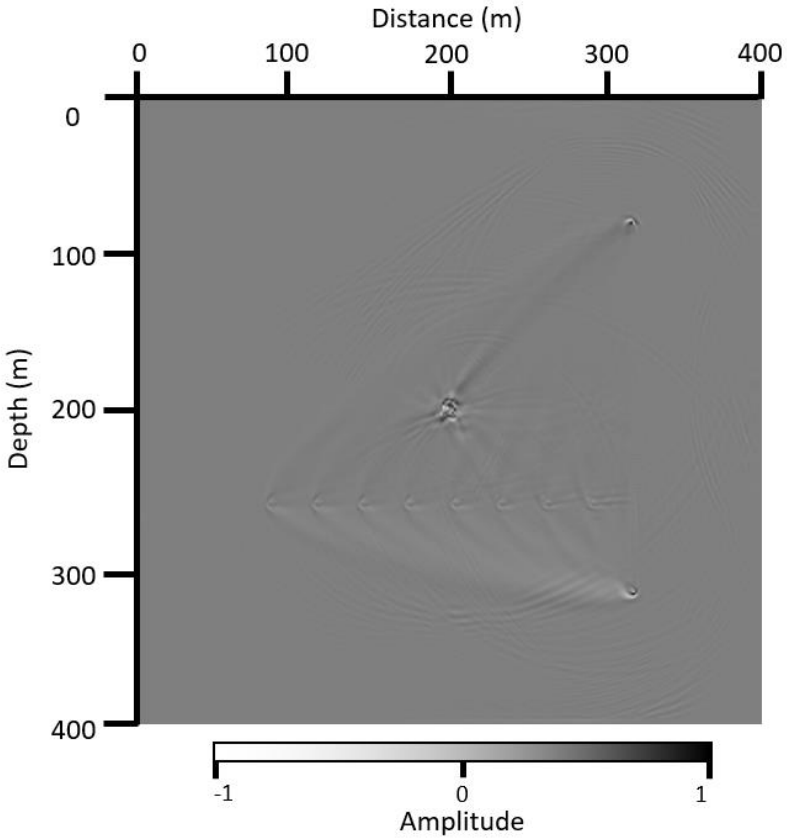

Figure 4.6: The result of a vertical derivative operator executed on Figure 4.5.

The operation of a vertical derivative on the stacked image is a technique used in artifact removal or edge detection in reverse-time migration imaging (Guitton et al., 2007). This technique exploits low wave number artifacts in the vertical domain. In an ideal scenario, source and receiver positions should be positioned from all angles surrounding the imaging target, but, is impractical within the context of subsurface-seismic imaging.

4.5 IMAGING OF HORIZONTAL INTERFACES

Source and receiver geometries were defined to simulate a lateral well in an unconventional reservoir. Sources are evenly spaced along a horizontal line to simulate the regular spatial increments that perforation shots are positioned. The receiver line is vertically oriented and positioned at the far offset of the computational domain to simulate a monitor straddling the formation in which the lateral well is positioned.

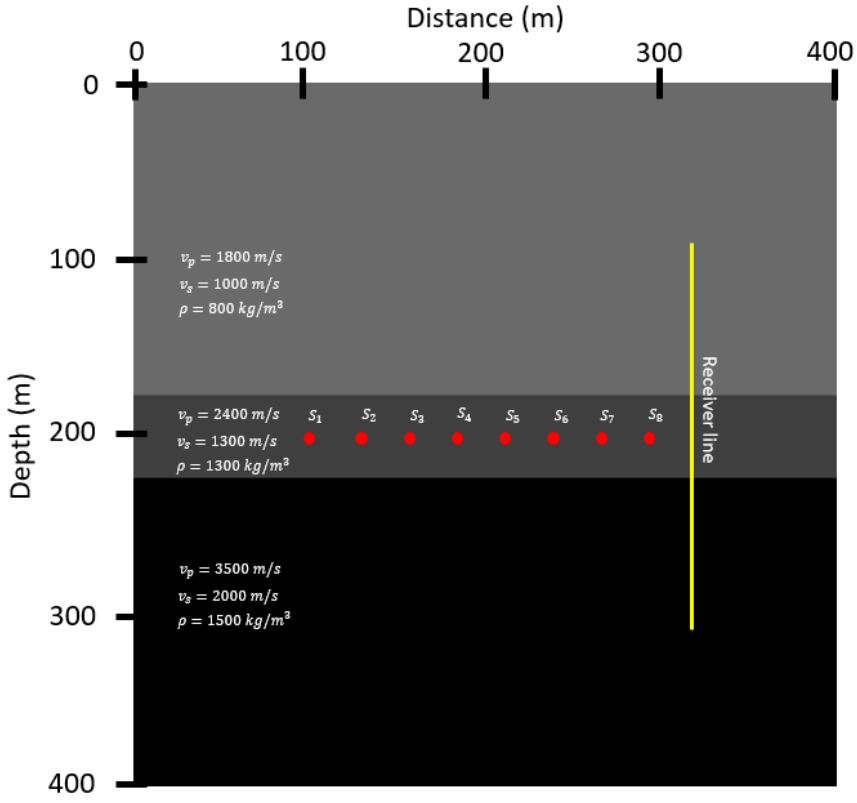

Figure 4.7: The computational domain involved in imaging from sources positioned within a laterally homogeneous formation.

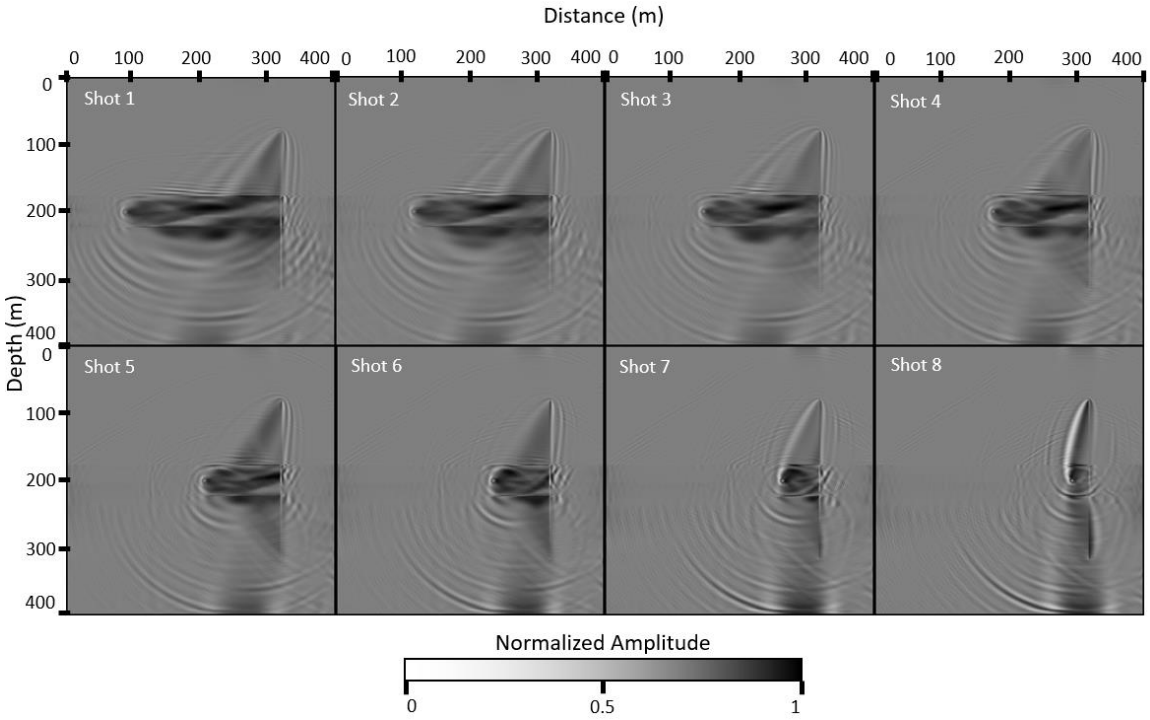

Figure 4.8: Individual shot image results from the elastic reverse-time migration of shots illustrated in Figure 4.7.

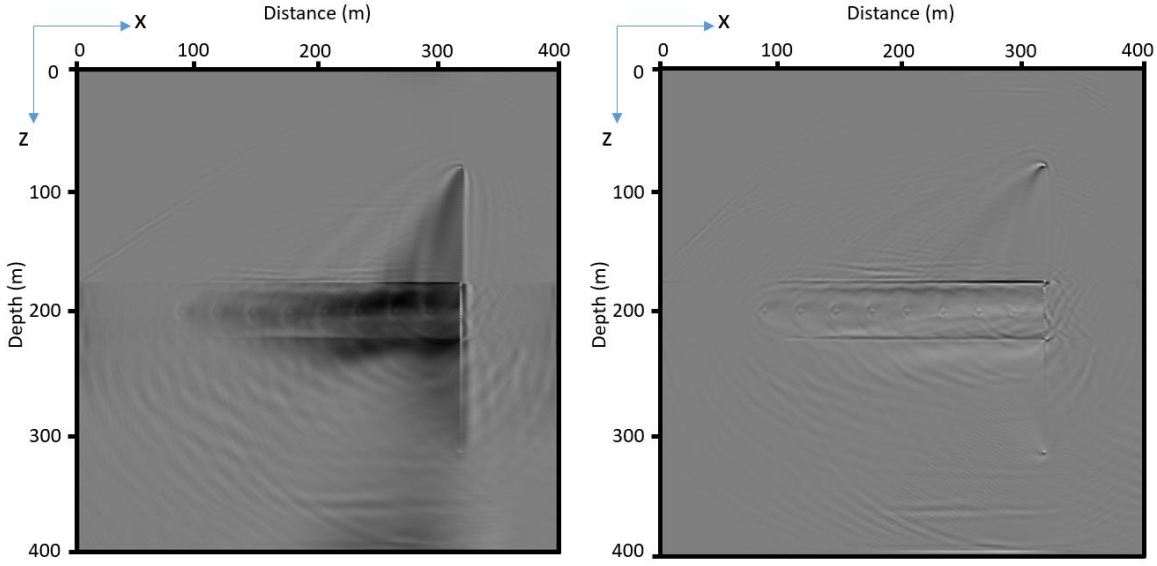

Figure 4.9: A stacked image result from the addition of images in Figure 4.9 (left) and the result from a first vertical derivative of the stacked image.

The interfaces imaged in Figure 4.8 are resolved well with low-amplitude source and receiver artifacts. It is worth noting that time interval over which construction of the forward and adjoint-wavefield are performed should be dependent on ray path distance, and thus travel time, from source to farthest receiver to minimize any noise introduced into the stacked image. I did not account for this when creating our images, and as a result, there are noise artifacts present in the image from reverberations recorded in the shot record.

4.6 IMAGING OF A COMPLEX SYNTHETIC MODEL

I cut a portion of the Marmousi 2 model that contains a large fault of imaging interest, and semi-lateral formations that allow us to realistically model the trajectory of perforation shots in a lateral well. The receiver line is positioned so the faulted region is between the source and receiver positions. The goal of this synthetic example is to simulate an environment where imaging in the near borehole vicinity may provide insight into the near borehole structure.

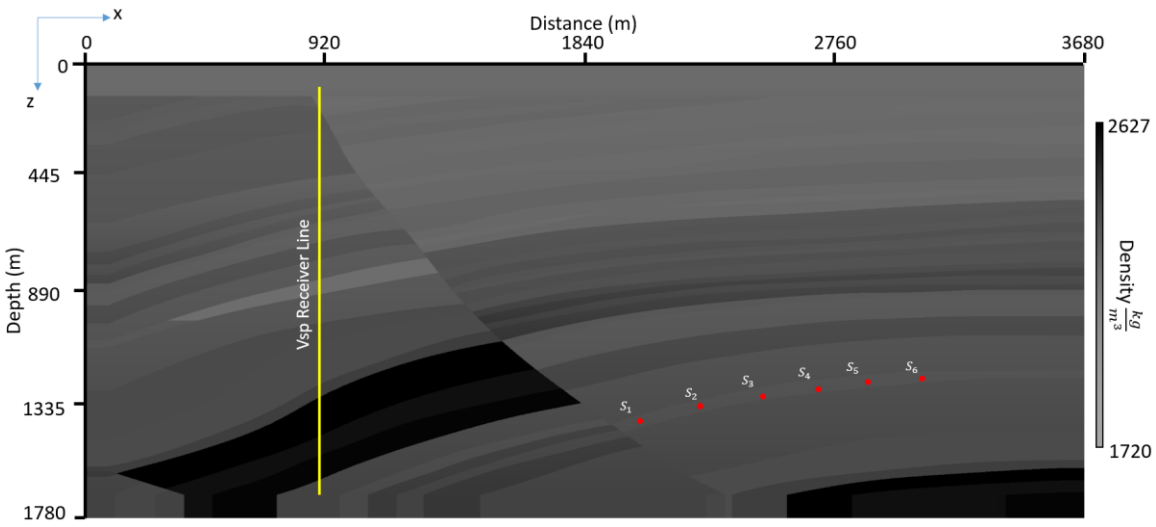

Figure 4.10: The computational model illustrating the density property, with corresponding receiver line and source positions illustrated. Source positions are intended to model perforation shots in a lateral well whose trajectory coincides with the mid-thickness of the formation of interest.

While the density in Figure 4.10 shows the contrast in property value in many interfaces, in general, reverse-time migration images interfaces of amplitude mode conversion and reflectivity, which may not correspond with interfaces in any single property model.

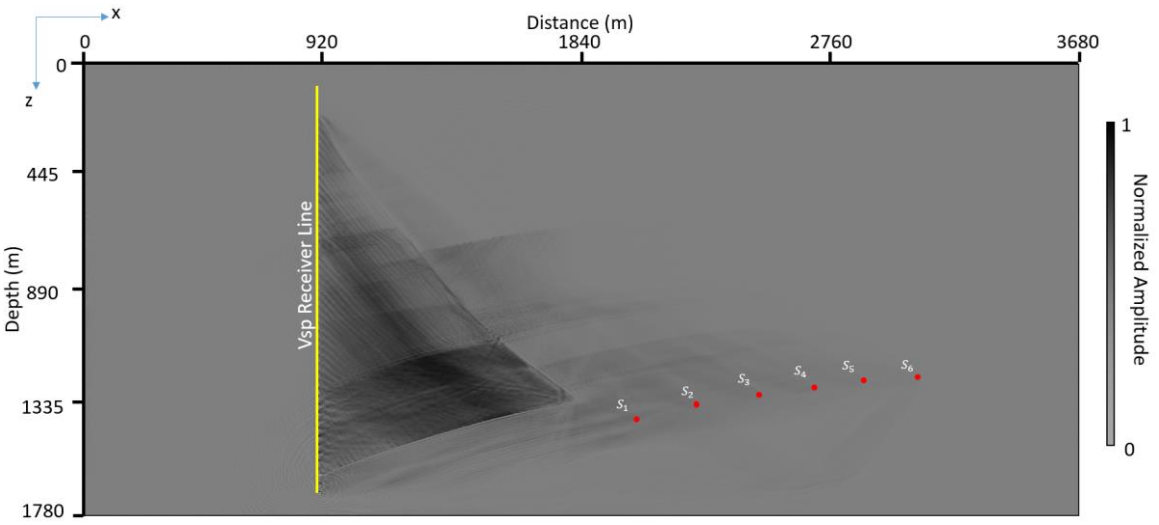

Figure 4.11: The stacked result from imaging the model illustrated in Figure 4.10 with corresponding source positions and receiver line.

The stacked image in Figure 4.11 images the large fault and adjacent interfaces within the region defined by wave paths from source to receiver-set. Artifacts close to the receiver-set are due to a large vertical receiver spacing when compared to the wavelength of the wavelet function used at the source. These sampling artifacts are even more apparent after edge detection, as shown in Figure 4.12.

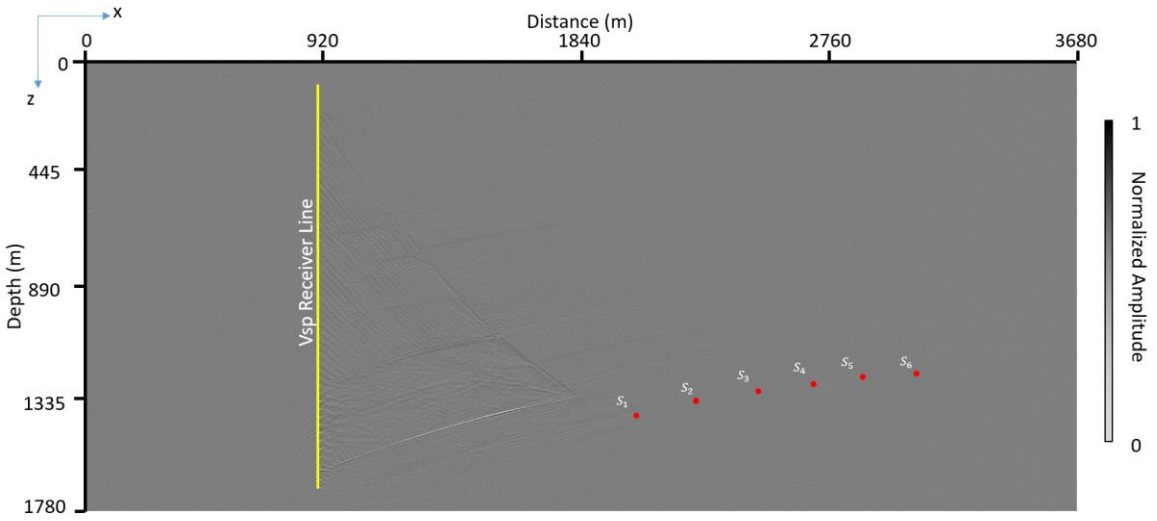

Figure 4.12: An image of a first-derivative operation performed in the vertical direction of Figure 4.11.

4.7 IMAGE DEPENDENCE ON ACQUISITION SPATIAL SAMPLE RATE

Previously, the spatial density of receivers with respect to source wavelength has accommodated any artifacts associated with acquisition spatial sample rate. Acquisition geometries in real observation wells are limited in swath and receiver spatial density.

Densley sampled receivers offer the benefits of both higher image resolution and more effective and coherent noise attenuation (Henley et al., 2012). This is demonstrated in Figure 4.13.

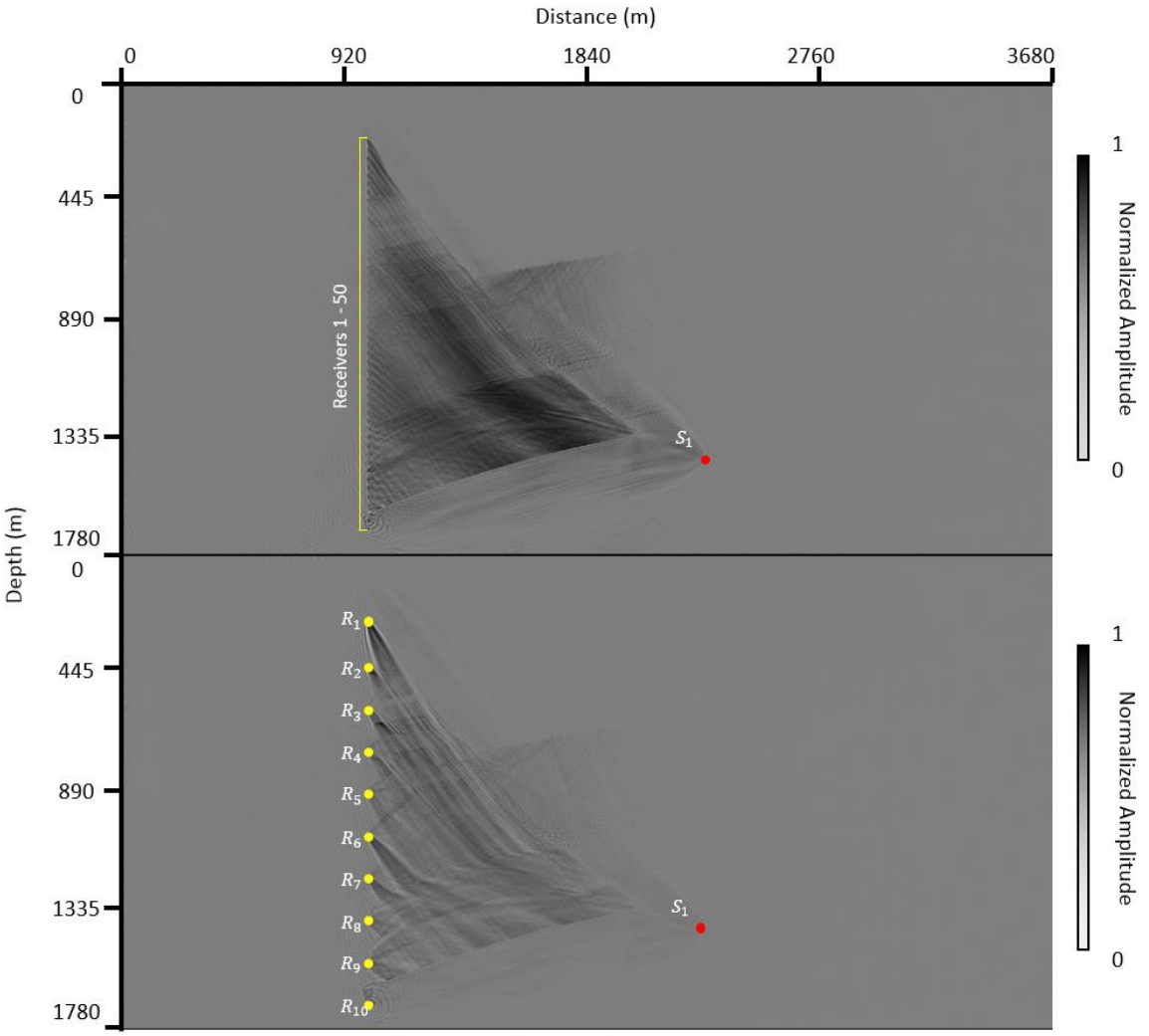

Figure 4.13: A single-shot image generated from the model illustrated in 4.9. The source wavelet amplitude function used is a 90 Hz Gaussian derivative function. Receiver spacing for the densely sampled receiver-set is 32 m (top). Receiver spacing for the sparsely sampled receiver-set is 160 m (bottom). Receiver sparsity is directly responsible for lowered imaging resolution in the bottom example.

I create two images of the Marmousi 2 model from one shot and two different receiver-sets. In the ideal scenario, I use a 50 receiver VSP with receiver spacing at 32 m. In the sparsely sampled scenario, each receiver is positioned 160 m from its neighbor. Figure 4.13 shows the differences in image quality from a single-shot with different

receiver sample rates. To evaluate an appropriate vertical sample rate for receivers, the Nyquist sampling relation is used.

$$\frac{f_{max}|\sin(\max(\theta,\varphi))|}{v_{max}(x_r, z_r \in z_{0r}: z_{nr})} \leq \frac{1}{2\Delta z}. \tag{4.8}$$

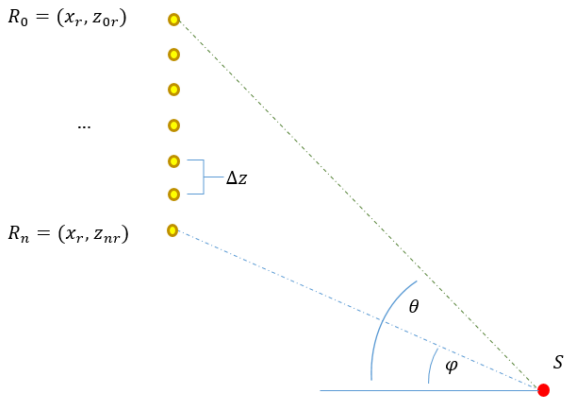

Figure 4.14: A diagram of approximate source and receiver-set geometry for a vertical seismic profile. Note that ray paths will not be straight trajectories if the model is non-homogenous. Annotations correspond to variables represented in Equation 4.3

While Figure 4.13 illustrates imaging with different receiver spatial sample rates, both images violate the Nyquist sampling relation in Equation 4.7 and contain artifacts. The maximum velocity along the receiver trajectory is 2200 m/s, and receiver spacings are both 160 m and 32 m and violate Equation 4.8 for a source wavelet frequency of 90 Hz.

4.8 CONCLUSIONS

In this chapter, I introduced the foundation of elastic reverse-time migration from reference material and implement a modified elastic reverse-time migration imaging condition based on the works of Jiang (2009) to accommodate receiver illumination

artifacts present when performing reverse-time migration on a dataset acquired from a vertical seismic profile survey.

I then tested my implementation on several different synthetic test cases consisting of a small square diffraction structure, a set of horizontal interfaces surrounding a set of point sources simulating perforation shots in a lateral well, and a complex structured subset of the Marmousi 2 model with a specific interest in imaging a target fault. I then addressed image contamination due to inadequate receiver spatial sample rate.

Chapter 5. Reverse-time migration of perforation shot data in the Bakken shale

5.1 INTRODUCTION

In 2011, Hess Corporation collected an extensive microseismic dataset to investigate the utility of microseismic data in delineating depletion geometry extents in unconventional wells. The En-Person 2H and 3H were drilled adjacent to preexisting production well, En-Person 1H, to test for optimal well spacing in an unconventional reservoir production environment (Figure 5.1). Special attention was paid to look for stimulated hydraulic-fracture network interference during and after hydraulic-fracture stimulation of the infill wells. The processing performed on this data set focuses on locating microseismic hypocenter positions (Li, et al. 2012). These processing efforts were performed under the assumption that an increase in microseismicity can provide information about the geometry of a stimulated reservoir volume (Dohmen et al.,2014).

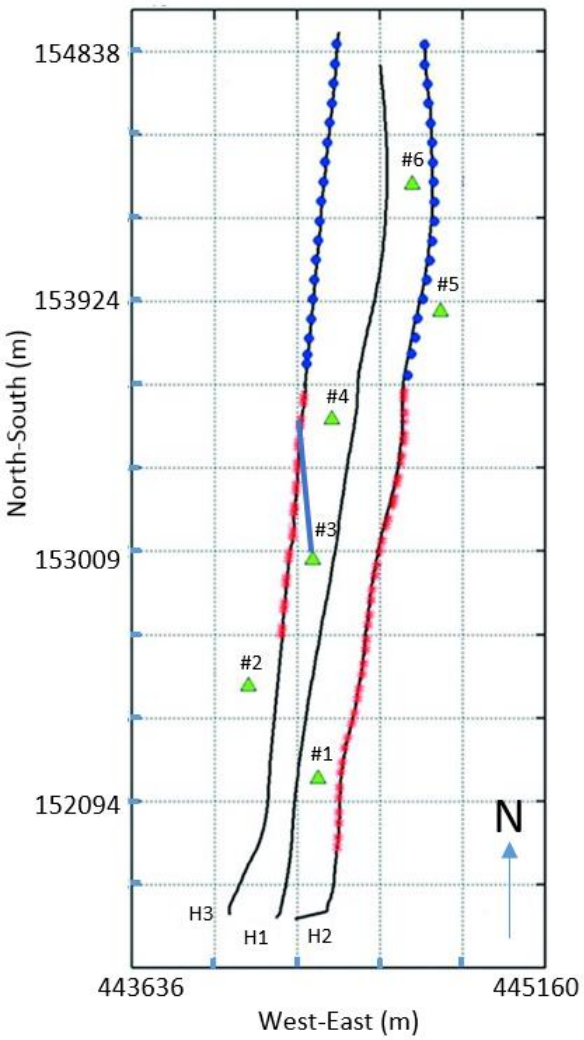

Figure 5.1: Map view of the En-Person well set and observation wells. Observation wells are indexed in an increasing fashion from south to north.

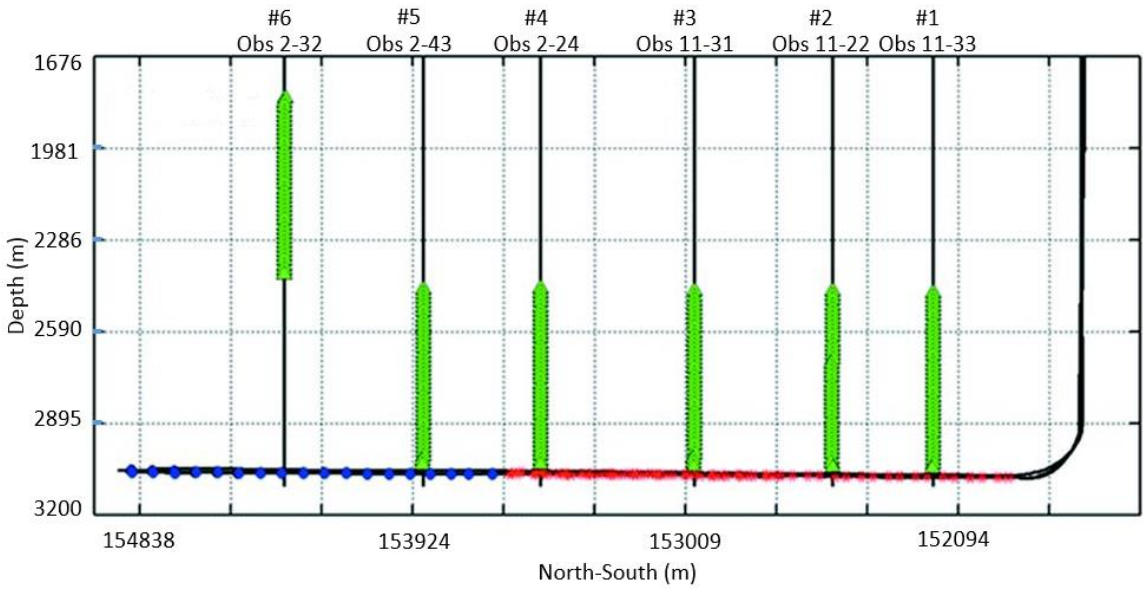

Figure 5.2: Side view of the En-Person well set and observation wells. Observation wells are indexed in an increasing fashion from south to north.

During hydraulic-fracture stimulation of stages 21 and 22 of the H2 well, increased microseismicity from the Lodgepole formation located above stage 22 of the H3 well was inferred to be the result of slip along a preexisting fault network from interaction with the increased stress from hydraulic fracturing in the En-Person wells.

The goal of this chapter is to evaluate the practicality of the elastic reverse-time migration technique established in Chapter 4 of this thesis, on real data from the EN-Person microseismic data set. By computing an image of the near borehole medium, I attempted to resolve and interpret any perturbations in the medium that may be indicative of preexisting natural fractures.

A 2D computational domain that intersects the vertical receiver-set contained in observation well 11-31 and the midpoint between perforations 2 and 3 in stage 20 of the

EN-Person-2H well is constructed. Well logs measured in microseismic observation well 11-31 were then used to construct a 2D stiffness and density model with the assumption of lateral homogeneity. A synthetic elastic reverse-time migration imaging test was performed on synthetic data to demonstrate potential ideal imaging products. Finally, an elastic reverse-time migrated image was computed from perforation shot data recorded at observation well 11-31 from perforations 2 and 3 from stage 20 of the EN-Person 2H well.

5.2 EXPERIMENTAL SETUP

The aim of this experiment was to attempt to image the near borehole vicinity between Microseismic observation well 11-31 and the midpoint between perforation shot 2 and 3 in stage 20 of En-Person H3. The 2D computational-grid used contained an origin point at the midpoint between the two perforation shots along the trajectory of the H3 well, was extended laterally to the base of observation well 11-31, and vertically to the shallowest receiver within the observation well that was used to record perforation shot data. The computational domain is shown in map view in Figure 5.3 and in side and oblique views in Figure 5.4.

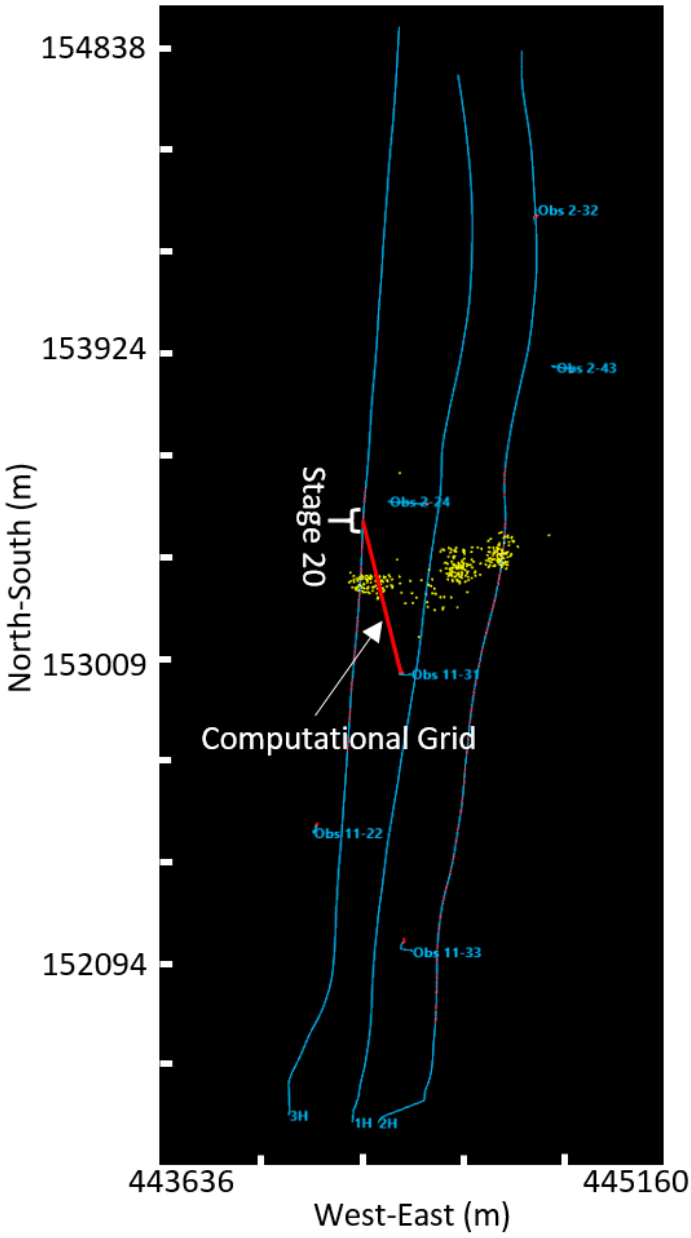

Figure 5.3: Map view of En-Person well trajectories, En-Person 2H stage 22 microseismic events, and the computational-grid used to image the medium between perforations 2 and 3 in stage 20 of En-Person 3H and observation well 11-31.

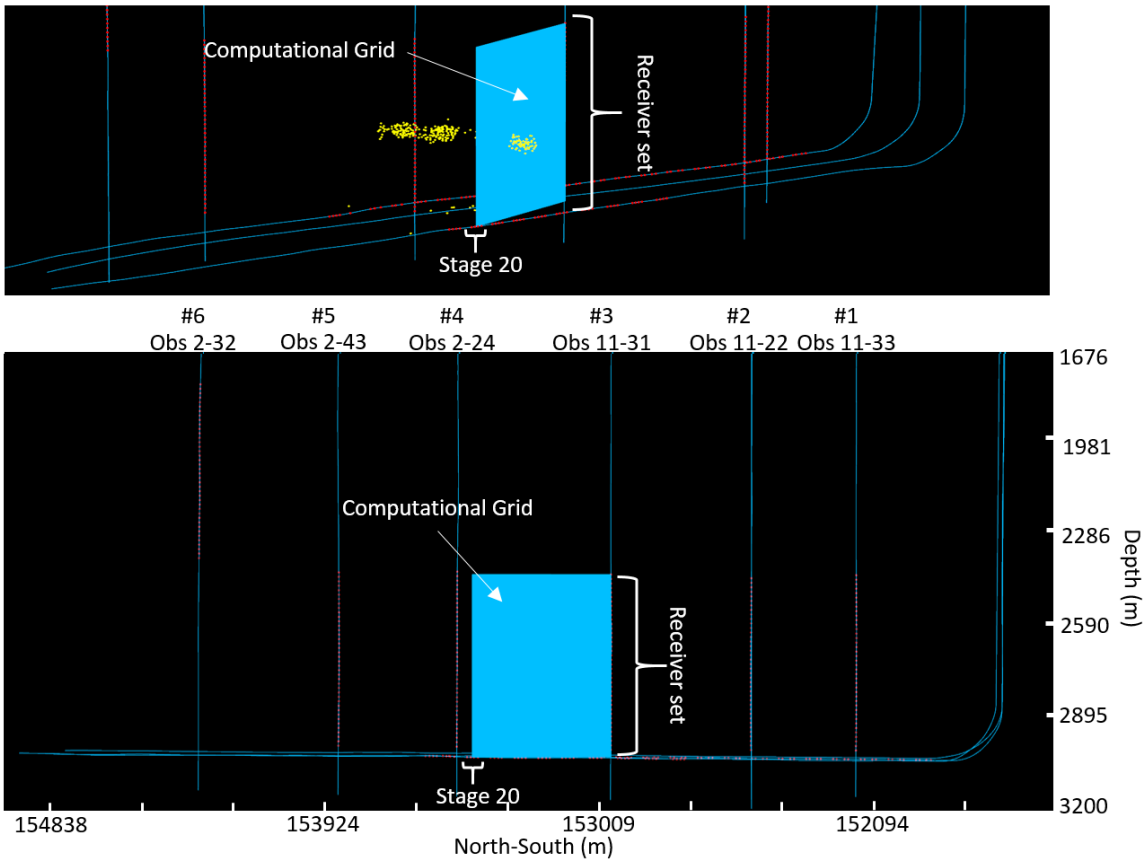

Figure 5.4: side view (bottom), and an oblique view (top) of the computational domain in the context of En-Person production wells and microseismic observation wells. The points in yellow represent hypocenter locations of micro-seismicity generated from stage 22 of the En-Person H2 well.

Compressional and shear sonic logs recorded in observation well 11-31 were used to construct stiffness and density models under the assumption of lateral homogeneity and isotropy. Yang et al., (2013) describes how the target region for the horizontal wells drilled was the middle Bakken, which is straddled by the upper and lower Bakken units of anomalously low velocity and density. The reverse-time migration source-mechanism is positioned at a depth of 3075 m. The receiver-set is positioned within the Lodgepole formation.

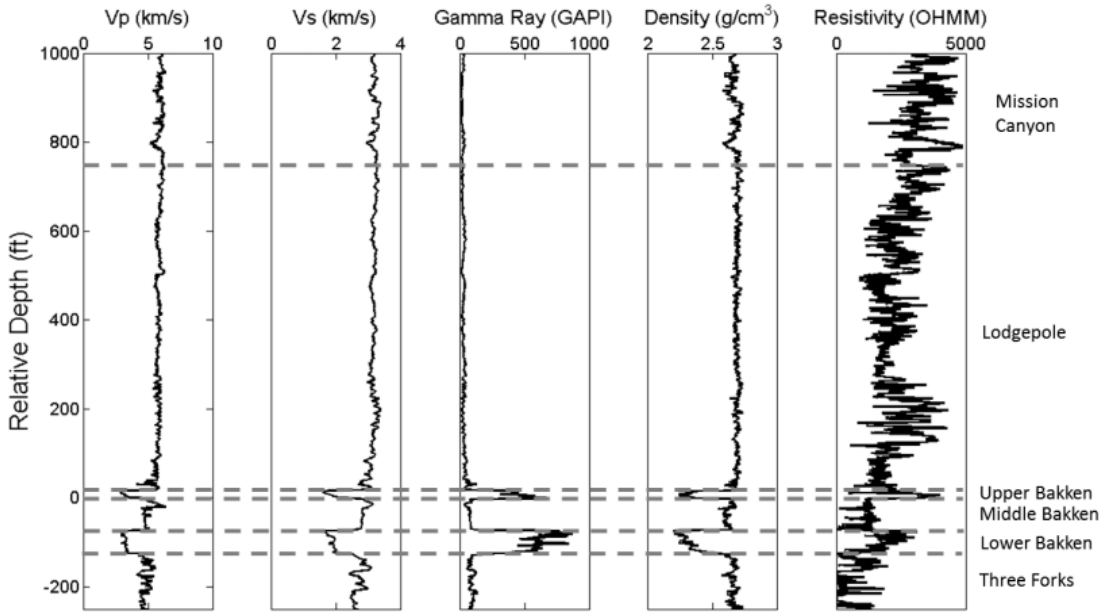

Figure 5.5: A petrophysical log collected from observation well 11-33 that shows the lithological profile across the Bakken formation (Yang et al., 2013).

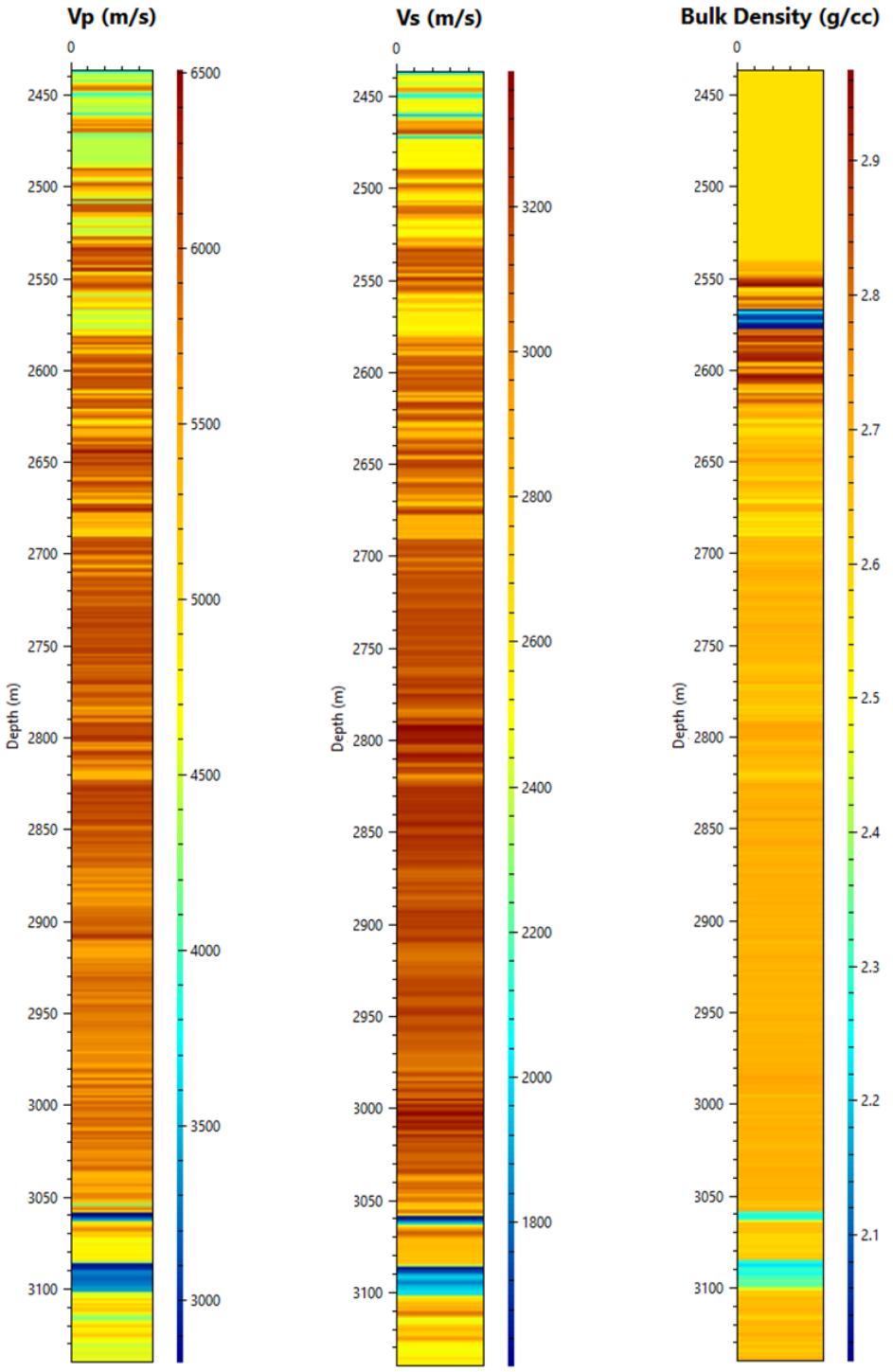

Figure 5.6: Sonic logs and bulk-density log acquired in observation well 11-31 used to construct the computational model used in this reverse-time migration experiment.

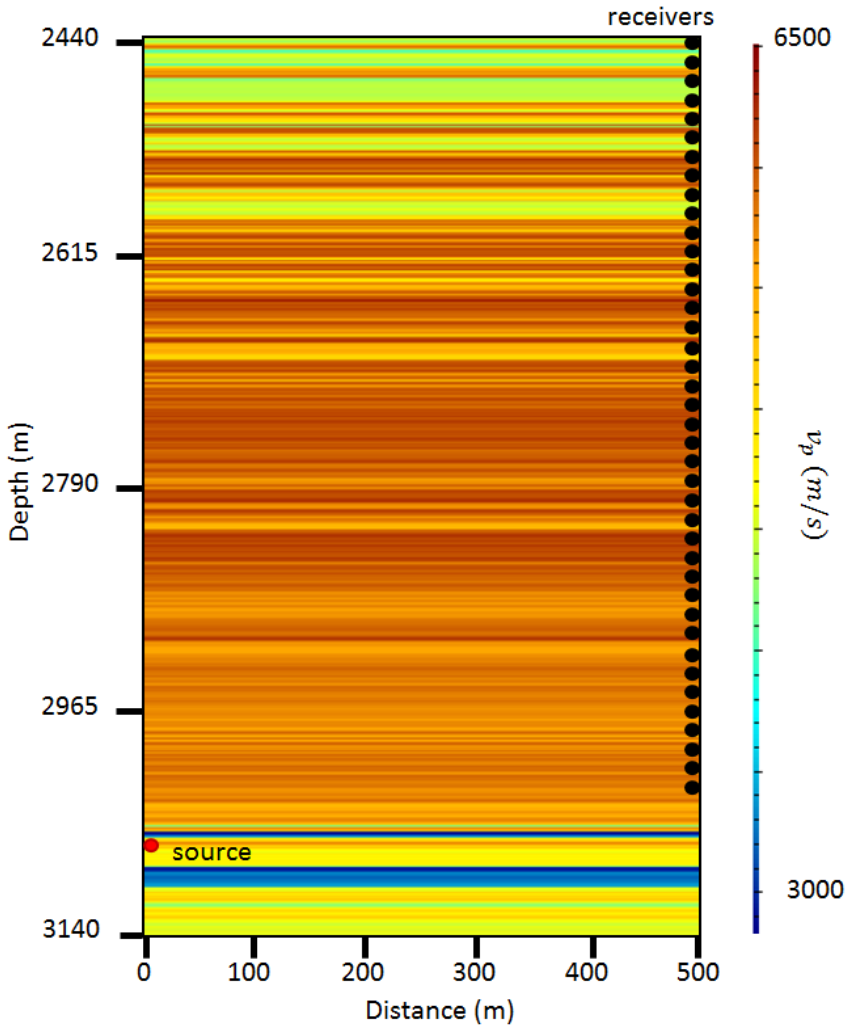

Figure 5.7: The experiment acquisition geometry overlain with the compressional velocity model. The red circle illustrates the position of the perforation shot while the black circles illustrate the positions of the receivers.

5.3 SYNTHETIC EXAMPLE

Before attempting to compute an image from perforation shot data via elastic reverse-time migration, a synthetic data set was produced that simulates, in 2D, the

response of a point force perforation gun. There are two main purposes of this synthetic migration test. Firstly, a comparison of synthetic data to the real perforation data helps to provide some information about the validity of both the source-mechanism for the forward wavefield operator and the computational domain constructed from well logs acquired in observation well 11-31. Secondly, a qualitative interpretation of how well elastic reverse-time migration can resolve interfaces may be made.

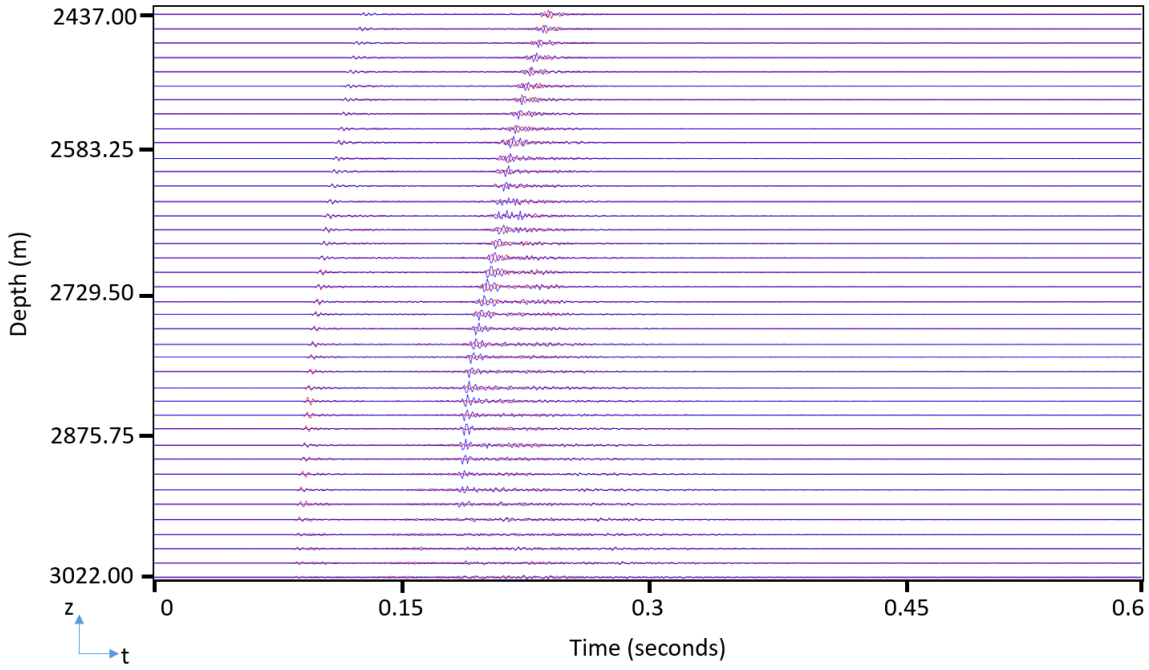

Figure 5.8: Traces recorded at receiver positions from a synthetic perforation shot.

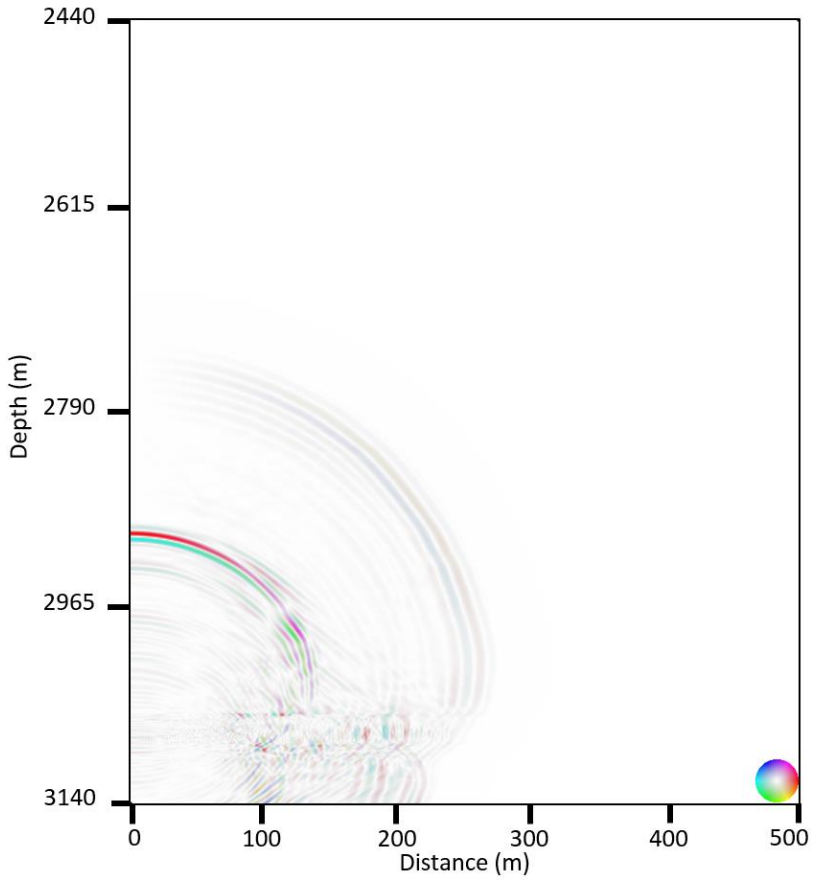

Figure 5.9: A snapshot at t=0.0604 seconds of a simulated forward wavefield propagation excited by a horizontal point force within the model illustrated by Figure 5.7.

The reverse-time migration was performed on a $(nx, \mathrm{nz}) = (586,426)$ node grid with spatial sample rate of 1.2 m in both orthogonal directions. The source wavelet was a 220 Hz wavelet injected into the velocity-field at the source location shown in Figure 5.7. Trace records are shown in Figure 5.8. The imaging output of this synthetic data represents an ideal reverse-time migration product and is shown in Figure 5.10 and 5.11. While some strong contrasts in velocity are imaged with success in the shallower regions of the computational domain as well as the middle Bakken, acquisition artifacts are

observed from an inadequate receiver spatial sample rate. These artifacts appear as interfaces between receivers. The upper Bakken-Lodgepole interface and lower Bakken-Three Forks interfaces act as a barrier of low transmission at which energy is reflected and refracted within the Bakken formation. These wave phases appear as signal distortion in the deepest 5 receivers and make imaging more difficult.

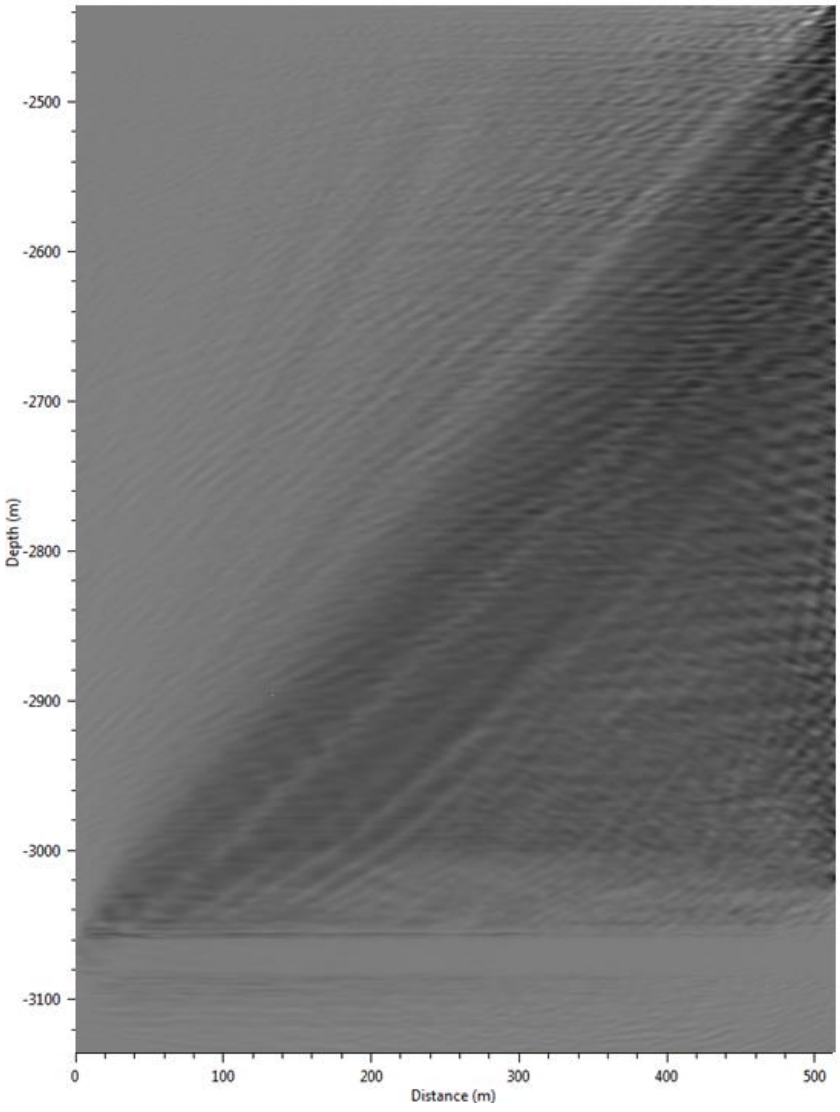

Figure 5.10: An image produced from reverse-time migration of a synthetic data set.

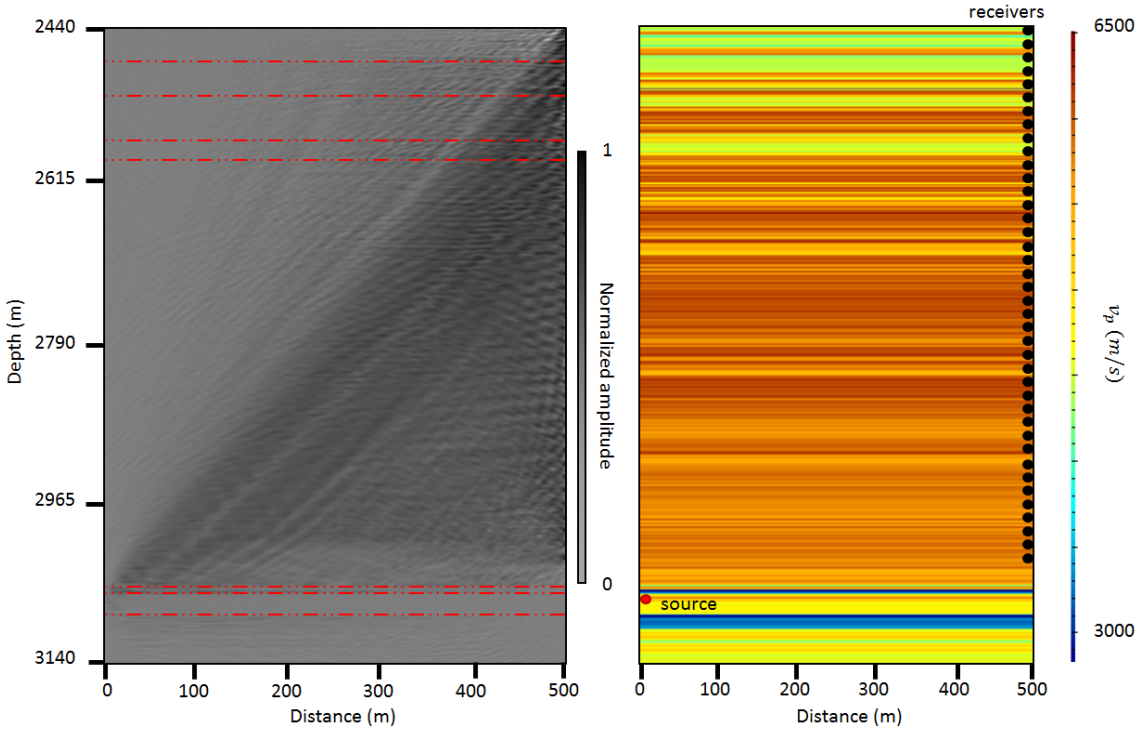

Figure 5.11: A resultant image from reverse-time migration of synthetic perforation shot data (left) and a compressional velocity model (right). Velocity-contrast interface interpretations are presented as red dashed lines.

Due to the large amplitude and quantity of imaging artifacts, I chose to execute a band pass filter on the resulting image. The frequency spectrum of the filter eliminated frequencies in the vertical direction with wavenumber lower than 90 Hz and greater than 500 Hz. This frequency range was chosen in order to highlight frequencies from the lower range of possible microseismic frequencies, near 220 Hz, of the wavelet used during forward wave propagation of this synthetic experiment. An amplitude gain of magnitude 2 was used to highlight coherent signal.

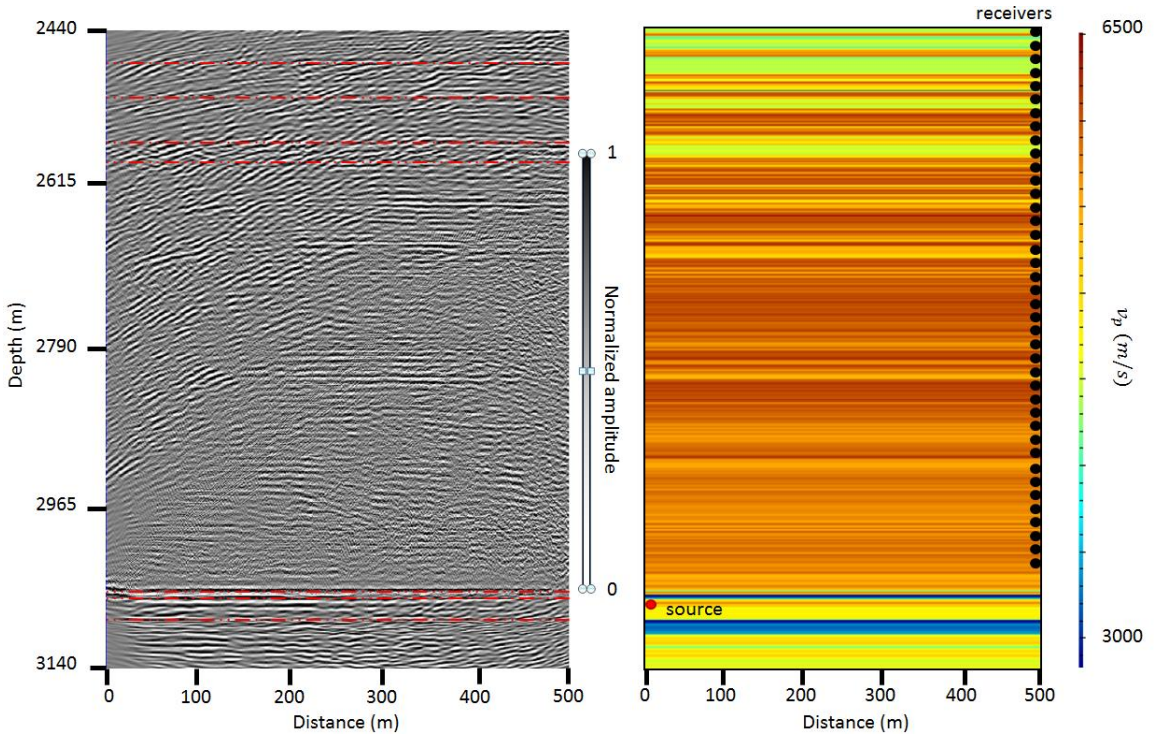

Figure 5.12: A band pass filtered and gained image from reverse-time migration of synthetic perforation shot data (left) and a compressional velocity model (right). Velocity-contrast interface interpretations are presented as thin red dashed lines.

A successful bandpass filter and gain of the migrated image highlights reflection interfaces within the computational model and is shown in Figure 5.12. While the stacking fold is minimal for this example, this image enhancement technique will play a part in imaging of the real perforation shot data.

To demonstrate the value of stacking images from multiple source-receiver geometry configurations, A 10 shot stacked synthetic image was created and band pass filtered. The filtering parameters were the same as in the single-shot synthetic image example illustrated in Figure 5.12. The 10 shots were distributed evenly in the lateral

direction at the depth of the source described in the previous single-shot synthetic example to best simulate a set of perforations in a middle Bakken targeted lateral well.

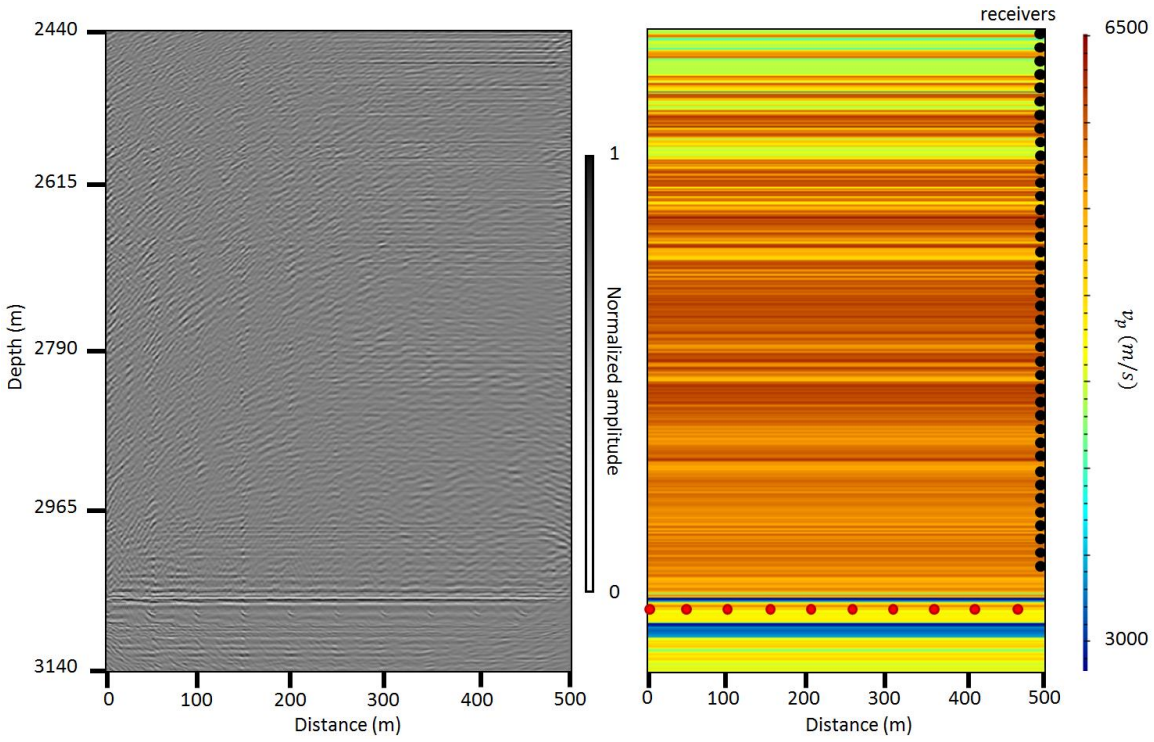

Figure 5.13: A 10 shot stacked synthetic image created from sources and receivers illustrated in the model schematic (right). The reflection and transmission interfaces contain substantially higher relative amplitude when compared with the single-shot synthetic example illustrated in Figure 5.12.

5.4 IMAGING WITH PERFORATION SHOT DATA

By consuming the same computational domain used in the synthetic example in the previous section of this chapter, an image was constructed from perforation shot data shown in Figure 5.14 with a 220 Hz Ricker wavelet used as a source to construct the forward wavefield. Trace rotation was performed on each trace to satisfy reduction in dimensionality of the 2D computational domain. Inline and vertical components were

extracted and used as data for construction of the adjoint-wavefield. Rotation angles were evaluated by aggregating compressional energy defined in a P-wave direct arrival pick window of 10 milliseconds and evaluating the aggregate azimuth of the compressional energy within the pick window.

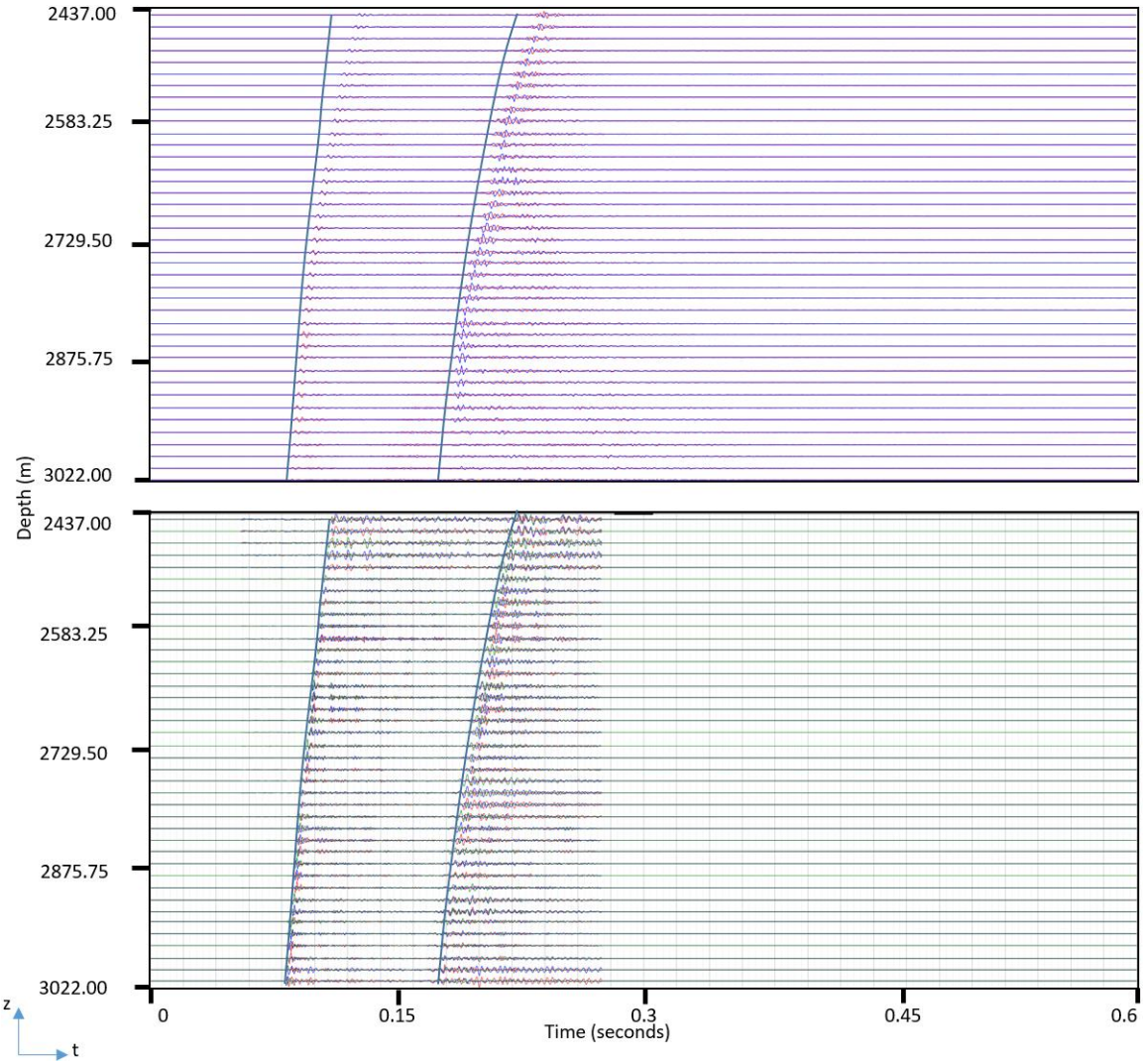

Figure 5.14: Simulated synthetic elastic-wavefield data from the En-Person stage 20 model (top) and data from En-Person stage 20 perforation shot number 2 as recorded from observation well 11-31 (bottom). Blue pick lines illustrate earliest arrival times for P- and S-waves for the real data acquired in observation well 11-31. The P-wave pick window is illustrated on the compressional wave direct arrival. The travel time residual between synthetic and real data is less than 0.001 seconds for both P-wave and S-wave direct arrival picks.

The image product from reverse-time migration of perforation shot data (Figure 5.15) is not as well resolved as its corresponding synthetic data image product. The raw stacked image illustrated in Figure 5.15 contains high-amplitude noise artifacts and is difficult to interpret.

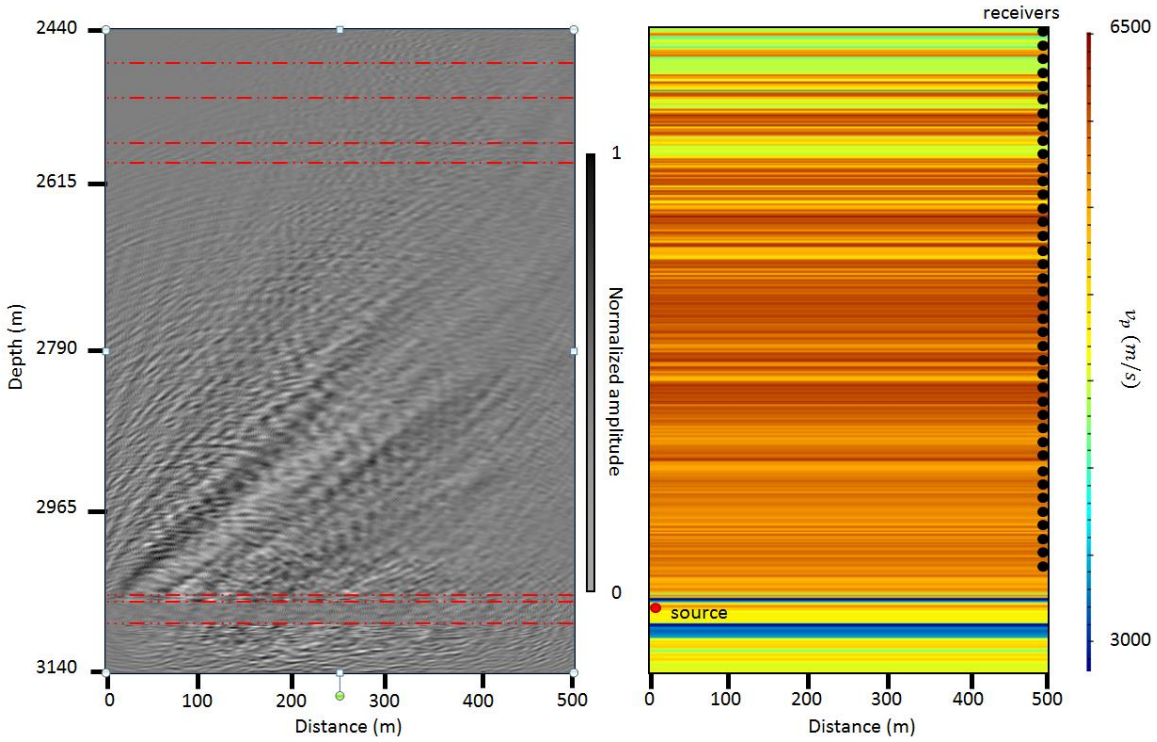

Figure 5.15: The imaging product from reverse-time migration of perforation shot data (left) along with well-resolved interface markers defined on the imaging product in illustrated in Figure 5.11, and the corresponding compressional velocity model used during reverse-time migration (right).

A 2D Fourier domain filter was executed, with Seismic Unix's suk1k2filter program, on the raw image data shown in Figure 5.15 to remove dipping artifacts. Filter arguments used for this application were defined on a frequency domain for both wavenumber axes.

The filter ranges were defined as a trapezoid for each orthogonal wavenumber domain with coordinates $p_1 = (0.0, 0.0)$, $p_2 = (0.02, 1.0)$, $p_3 = (0.45, 1.0)$, and $p_4 = (0.5, 0)$, where the first and second coordinate component values represent the frequency domain value and its corresponding filter amplitude, respectively.

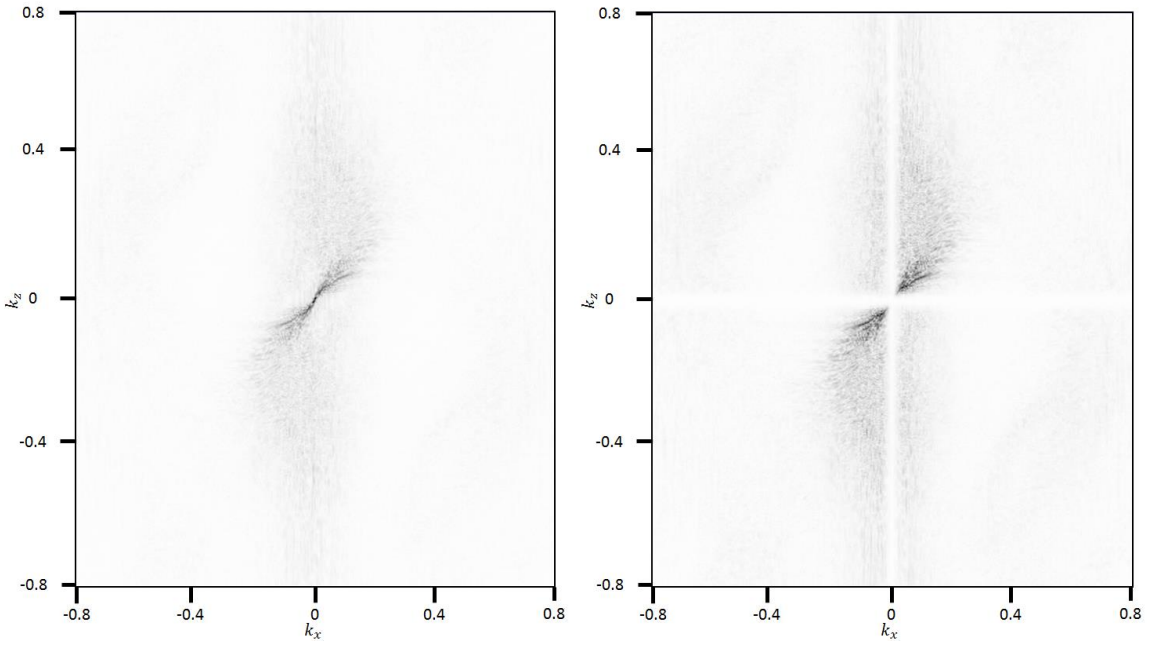

Figure 5.16: The result of a 2D Fourier transform on the perforation shot image shown in Figure 5.15 (left) and the amplitudes to be removed (right).

The Fourier domain geometry of the filter amplitude function contains a cross-like attenuated amplitude region centered at $k_x = 0$ and $k_z = 0$ and is shown in Figure 5.16. Filtering the original data is performed by subtracting the filter amplitude function (Figure 5.16 right) from the Fourier transformed original data (Figure 5.16 left). The result from the filter is an image with dipping amplitude features removed and is shown as the left image in Figure 5.17. A vertical trace low frequency filter was then executed to produce the right image in Figure 5.17.

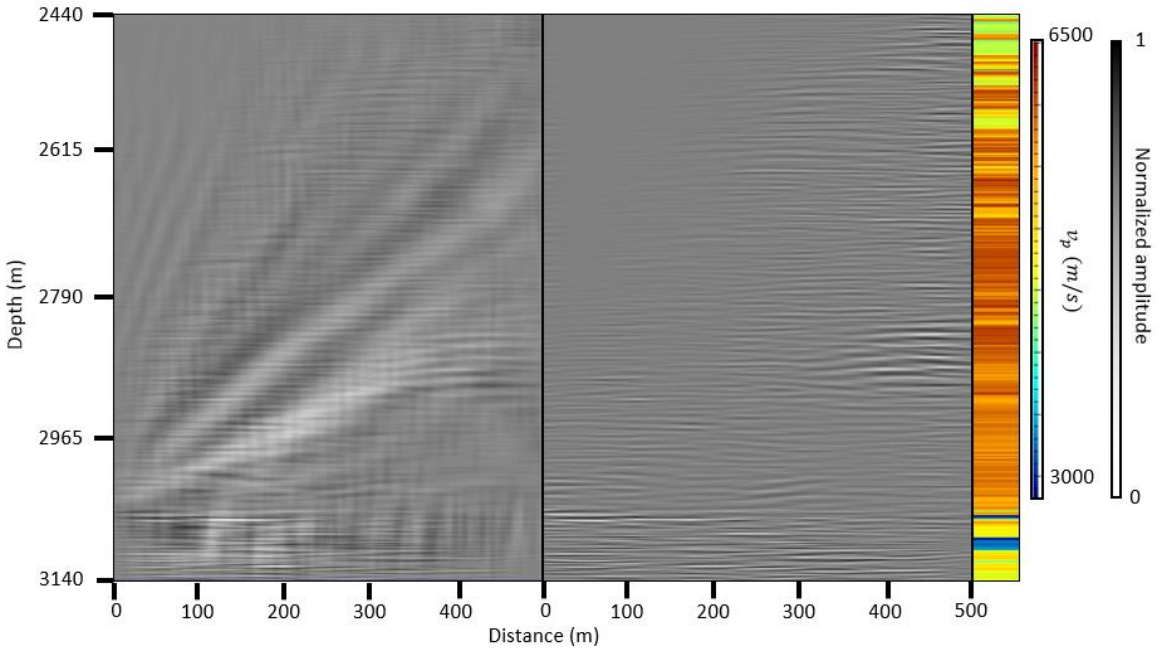

Figure 5.17: The result of a 2D Fourier domain filter on the image shown in Figure 5.15 (left) and a subsequent vertical band pass filter (middle). The vertical P-wave velocity model is shown on the right for reference to horizontally oriented velocity interfaces.

The final filtered image reveals interpretable features that correlate with velocity interfaces in the model. In an ideal scenario, more perforation shots within acceptable distance from the 2D computational-grid would be imaged and stacked to create a more complete image similar to the 10 shot synthetic example shown in Figure 5.13. Chapter 4 established reverse-time migration in a borehole setting as a practical means to image the subsurface between perforation shot in a lateral well and vertically oriented receiver-set in an adjacent monitoring well, but it did not address nuances of good practice in reverse-time migration of real world data. While a poor velocity model, spatial under-sampling of receivers with respect to the Nyquist frequency, and lack of stacking fold are culprits when considering a poor resolution of an image product from reverse-time migration,

standard artifact removal techniques, such as the Fourier domain based filters used in this chapter can help remove imaging artifacts and contribute to a more successful stacked image.

5.5 CONCLUSIONS

In this chapter, presentation of a target region of interest in the local vicinity of the En-Person lateral well set was presented. Construction of a computational model as a 2D subset region of the 3D volume surrounding stage 20 perforation sites and receivers positioned in observation well 11-31 was performed. Synthetic image generation was generated from a simulated perforation shot in the previously constructed computational domain. Imaging of 10 synthetic perforation shots was performed to present an ideal imaging scenario. An assessment of image quality in the synthetic image was used to assess image quality in the image product of the real perforation shot data. It was shown that the imaging technique implemented in Chapter 4 is highly dependent on both source-receiver-set geometries and physical model properties. The real-world perforation shot based image produced of the middle Bakken and neighboring formation units is initially poorly resolved possibly due to inaccuracies in the property models used during imaging but was successfully filtered via Fourier domain filtering methods to remove artifacts and imaging noise.

Chapter 6. Conclusions and future work

This thesis focused on the investigation and implementation of an elastic finite-difference simulation algorithm and its utility as a simulation kernel in reverse-time migration techniques for vertically oriented receivers. An implementation of a stress-velocity formulated finite-difference solution to the elastic-wave equation for arbitrary anisotropic media was defined, developed and demonstrated for isotropic and vertically transversely isotropic media. A modified reverse-time migration algorithm was suggested as a means to accurately image the medium between subsurface positioned sources and a vertically oriented receiver-set. The specific intent in suggesting the modified imaging algorithm was to accommodate both source and receiver illumination artifacts. I demonstrated the practicality of this new imaging algorithm on several computational models and qualitatively assess the image resolution dependence on acquisition geometry. In Chapter 5, an imaging example is demonstrated on both synthetic and real perforation shot data from stage 20 of the En-Person H3 as acquired by vertically oriented receivers in the adjacent observation well 11-31. Noise reduction techniques were used to enhance the quality of the perforation shot image.

While the imaging product presented in Chapter 5 is less than ideal when compared to that of its synthetic data imaged counterpart, reverse-time migration of perforation shot data was not considered when constructing acquisition geometry parameters of this microseismic monitoring survey. In future works, a spatially more dense and broad acquisition geometry may provide superior imaging quality and resolution. Also, an appropriately optimized elastic property model would be an ideal component to

incorporate into this imaging workflow to reduce image artifacts created from poor time aligned forward and adjoint-wavefields.

In future works, I hope to incorporate more robust computational technology with which a 3D implementation of the reverse-time migration algorithm presented here may be constructed and used. Also, I intend to focus on testing this algorithm on more broadly acquired data with more densely sampled data. I also intend to implement elastic property model inversion algorithms to incorporate optimized property models in the imaging examples presented in this thesis as a means to increase imaging quality and resolution.

APPENDIX A Wavefield color display

Due to the multidimensional component nature of vector fields illustrated in this thesis, I chose to transform vector values defined on a Cartesian domain into an HSL color domain similar to the method using in Manning (2008). Vectors defined in 2 and 3 dimensions can be transformed and illustrated in a single image, rather than conventional illustrations that rely on n images for n-dimensional vectors.

2D vector fields shown in this thesis are defined on a spatial Cartesian coordinate system with vector values transformed into the HSL color domain.

$$A(U_y, U_x) = \begin{cases} \tan^{-1}\left(\frac{U_y}{U_x}\right) \; if \; U_x > 0 & if \; U_x < 0, \\ \tan^{-1}\left(\frac{U_y}{U_x}\right) \; if \; U_x > 0 & if \; U_x < 0 \; and \; if \; U_y \geq 0, \\ \tan^{-1}\left(\frac{U_y}{U_x}\right) \; if \; U_x > 0 & if \; U_x < 0 \; and \; if \; U_y < 0 \\ +\frac{\pi}{2} & if \; U_x = 0 \; and \; if \; U_y > 0 \\ -\frac{\pi}{2} & if \; U_x = 0 \; and \; if \; U_y < 0 \\ undefined & if \; U_x = 0 \; and \; if \; U_y = 0 \end{cases}. \quad \text{(A.1)}$$

$$H = \frac{A(U_y, U_x) - A(0,1)}{2\pi}. \quad \text{(A.2)}$$

$$S = \sqrt{{U_x}^2 + {U_y}^2}. \quad \text{(A.3)}$$

$$L = 1 - \frac{\sqrt{{U_x}^2 + {U_y}^2}}{2}. \quad \text{(A.4)}$$

Equation A.1 transforms vector component values U_y and U_x into an angular displacement value from the x axis. Equation A.1, A.2, and A.3 define hue, saturation, and luminance values for a vector given its Cartesian coordinate system component values. Figure A.1 illustrates all possible color values for a 2D vector.

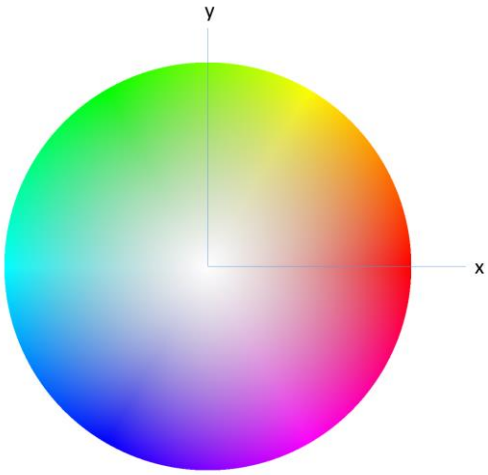

Figure A.1: The HSL domain parameterized 2D vector values. As normalized vector magnitude reaches the maximum value of the total field, color saturation increases. Color hue represents angular direction.

The transformation defined in A.1, A.2 and A.3 imply that only a subset of the HSL domain is consumed for 2D vector valued functions.

Vector fields with vector values defined on a 3D Cartesian domain extend the color transformation concepts for 2D into 3D. In 3D I use the complete HSL domain by transforming spherical coordinate system referenced vector components shown in Figure A.2 by the following transformations:

$$\varphi = \frac{z}{\sqrt{{U_x}^2 + {U_y}^2}}. \tag{A.5}$$

$$\vartheta = \frac{\varphi}{\pi} + \frac{1}{2}. \tag{A.6}$$

$$h = \frac{\theta}{2\pi}. \tag{A.7}$$

$$s = \frac{1}{2}(1 - \cos(\pi r))(1 - \cos(2\vartheta\pi)). \tag{A.8}$$

$$l = \frac{1}{2}\left(1 - \frac{2\vartheta}{\pi}\right)(1 - \cos(\pi r)) + \frac{1}{4}(1 + \cos(\pi r)). \quad \text{(A.9)}$$

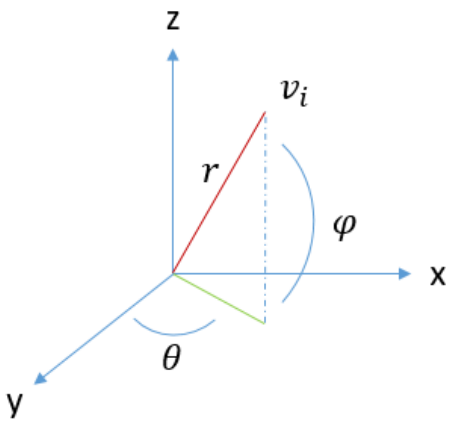

Figure A.2: a 3D vector diagram illustrating both Cartesian and spherical coordinate reference systems and their constituent components. x, y, and z represent basis vectors in a 3D Cartesian coordinate reference system. $\theta, r,$ and φ represent component coordinates in a spherical coordinate reference system. v_i represents the vector defined in an arbitrary coordinate reference system.

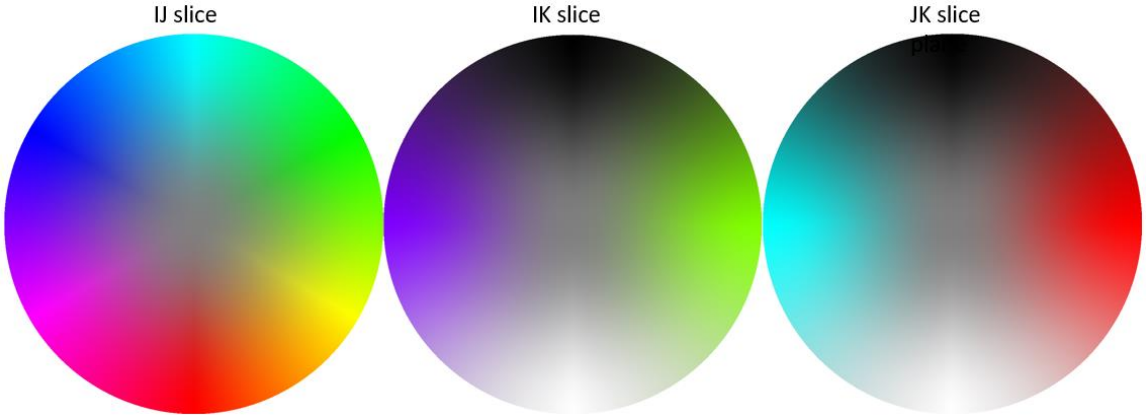

Figure A.3: Cross sections of the color sphere described in Appendix A for 3D vector spaces. Gray color represents the low magnitude and zero magnitude vectors. Black and White represent up and down, respectively, while all other color hues represent a lateral vector component.

Bibliography

Aki, K., and P. G. Richards. 1980. Quantitative Seismology: theory and methods. San Francisco: Freeman.

Blanton, Eric M., and Gordon Mackenzie. 2006. "Hydraulic Pump-Down Frac Plug and Subsequent Coiled-Tubing Removal Increases Client Efficiency in Barnett Shale Play." paper SPE 100139 presented at the SPE/ICoTA Coiled Tubing Conference & Exhibition. The Woodlands, Texas: Society of Petroleum Engineers.

Carcione, Jose M. 1998. "Visoelastic effective rheologies for modelling wave propagation in porous media." Geophysical Prospecting 46: 249-270.

Cerjan, Charles, Dan Kosloff, Ronnie Kosloff, and Moshe Reshef. 1985. "A nonreflecting boundary condition for discrete acousitc and elastic-wave equations." Geophysics 50 (4): 705-708.

Claerbout, J. 1971. "Toward a unified theory of reflector mapping." Geophysics 36 (3): 467-481.

Clayton, R., and B. Engquist. 1977. "Absorbing boundary conditions for acoustic and elastic-wave equations." Bulletin of the Seismological Society of America 67: 1529-1540.

Dohmen, Ted, Jean-Pierre Blangy, and Jon Zhang. 2014. "Microseismic depletion delineation." Interpretation 2 (3): SG1-SG13.

Duncan, Peter, and Leo Eisner. 2010. "Reservoir characterization using surface microseismic monitoring." Geophysics 75: A139–A146.

Eaton, D.W. 2009. "Resolution of microseismic moment-tensors: A synthetic modeling study." 79th Annual International Meeting, The Society of Exploration Geophysicists,Epanded Abstracts. 3569-3573.

Eaton, W. D. 2008. Microseismic focal-mechanisms: A tutorial. Calgary, Alberta: CREWES Research Report, Vol 20, 1-11.

Etgen, John, Samuel H. Gray, and Yu Zhang. 2009. "An overview of depth imaging in exploration geophysics." Geophysics 74 (6): WCA5-WCA17.

Fang, Xinding, Michael Fehler, Zhenya Zhu, Tianrun Chen, Stephen Brown, Arthur Cheng, and Nafi Toksoz. 2013. "An approach for predicting stress-induced anisotropy around a borehole." Geophysics 78 (3): D143-D150.

Fish, Ashley M. 2012. Microseismic Velocity Inversion and Event Location Using Reverse Time Imaging: [Dissertation]. Golden, Colorado: Colorado School of Mines.

Grechka, Vladimir. 2010. "Data-acquisition design for microseismic monitoring." The Leading Edge 29: 278-282.

Grossmann, Christian, Hans-G Roos, and Martin Stynes. 2007. Numerical Treatment of Partial Differential Equations. Heidelberg, Germany: Springer Science & Business Media.

Guitton, A., B. Kaelin, and B. Biondi. 2007. "Least-squares attenuation of reverse-time-migration artifacts." Geophysics 72 (1): S19-S23.

Henley, David C., Malcom B. Bertram, and Kevin W. Hall. 2012. "Spatial sampling, coherent noise, and subsurface resolution: conslusions from field experiments."

82nd Annual International Meeting, The Society of Exploration Geophysicists, Expanded Abstracts. Las Vegas, Nevada. 36-40.

Jarillo Michel, Oscar. 2015. Estimation of microseismic source parameters by anisotropic waveform inversion [Thesis]. Golden, Colorado: Colorado School of Mines.

Jarillo Michel, Oscar, and Ilya Tsvankin. 2015. Waveform inversion for microseismic source parameters: Synthetic and field-data applications. Center for Wave Phenomena, Colorado School of Mines.

Jiang, Zaiming, John C. Bancroft, and Laurence R. Lines. 2012. "Elastic Reverse-Time Migration." (CREWES) 24: 1-18.

Juhlin, Christopher. 1995. "Finite-difference elastic-wave propagation in 2-D heterogeneous transversely isotropic media." Geophysical Prospecting 45: 843-858.

Levander, A. R. 1988. "Fourth-order finite-difference P-SV seismograms." Geophysics 53: 1425-1436.

Li, C., T. Dohmen, S. Morton, K. Katahara, K. Hayles, S. Checkles, and J.P. Blangy. 2012. "Evaluating the quality of microseismic event locations." 82nd Annual International Meeting, The Society of Exploration Geophysicists, Expanded Abstracts.

Li, J., N. Toksoz, Li C., S. Morton, T. Dohmen, and K. Katahara. 2013. "Locating Bakken microseismic events with simultaneous anisotropic tomography and extended double-difference method." 83rd Annual International Meeting, The Society of Exploration Geophysicists, Expanded Abstracts. 2073-2078.

Madariaga, Raul. 1976. "Dynamics of an expanding circular fault." Bulletin of the Seismological Society of America 66: 639-666.

Manning, Peter M. 2008. "Techniques to enhance the accuracy and efficiency of finite-difference modelling for the propagation of elastic-waves." Ph.D. thesis, The University of Calgary.

Minkoff, Susan E. 2002. "Spatial parallelism of a 3D finite-difference velocity-stress elastic-wave propagation code." Journal on Scientific Computing: Society for Industrial and Applied Mathematics 24: 1-19.

Nakata, Nori, and Gregory C. Beroza. 2016. "Reverse-time migration for microseismic sources using the geometric mean as an imaging condition." Geophysics 81 (2): KS113-KS122.

Ratner, Michael, and Mary Tiemann. 2015. An Overview of Unconventional Oil and Natural Gas: Resources and Federal Actions. Congressional Research Service.

Thomsen, Leon. 1986. "Weak elastic anisotropy." Geophysics 51: 1954-1966.

Vermeer, G. 1989. Seismic wavefield sampling. Society of Exploration Geophysicists.

Warpinski, Norman R., Richard B. Sullivan, James Uhl, Charles Waltman, and Sean Machovoie. 2005. "Improved microseismic fracture mapping using perforation timing measurements for velocity calibration." The Society of Petroleum Engineers 10 (1): 14-23.

Weiss, Robin M., and Jeffrey Shragge. 2013. "Solving 3D Anisotropic Elastic-Wave Equations on Parallel GPU Devices." 78 (2): F7–F15.

Xuan, R., and Paul Sava. 2010. "Probabilistic microearthquake location for reservoir monitoring." Geophysics 75 (3): MA9-MA26.

Yan, Jia, and Paul Sava. 2009. "Elastic-wave-mode separation for VTI media." Geophysics 74 (5): WB19-WB32.

Yan, Jia, and Paul Sava. 2008. "Isotropic angle-domain elastic reverse-time migration." Geophysics 73 (6): S229-S239.

Yang, Yi, Mark Zoback, Michele Simon, and Ted Dohmen. 2013. "An integrated geomechanical and microseismic study of multi-well hydraulic-fracture stimulation in the Bakken Formation." Unconventional Resources Technology Conference. Denver, Colorado. Society of Petroleum Engineers paper 168778, 1-10.

Yee, Kane S. 1966. "Numerical solution of initial boundary value problems involving Maxwell's equations in isotropic media." IEEE Trans Antennas Propagation 14: 302-307.